REPORT DOCUMENTATION PAGE

1. AGENCY USE ONLY (Leave Blank)	2. REPORT DATE 15 Jan 98	3. REPORT TYPE AND DATES COVERED Final (15 May 94 – 14 May 94)

4. TITLE AND SUBTITLE
2D & 3D Modeling of Seismic Wave Propagation in the Heterogeneous Lithosphere in the Context of Nuclear Test Ban Monitoring

5. FUNDING NUMBERS
F49620-94-1-0278

6. AUTHORS
Dr. Eystein Husebye

AFRL-SR-BL-TR-98-

0127

7. PERFORMING ORGANIZATION NAME(S) AND ADDRESS(ES)
Bergen University
Norway

9. SPONSORING/MONITORING AGENCY NAME(S) AND ADDRESS(ES)
AFOSR/NM
110 Duncan Avenue, Room B-115
Bolling Air Force Base, DC 20332-8080

10. SPONSORING/MONITORING AGENCY REPORT NUMBER

11. SUPPLEMENTARY NOTES

12a. DISTRIBUTION AVAILABILITY STATEMENT
Approved for Public Release

12b. DISTRIBUTION CODE

13. ABSTRACT *(Maximum 200 words)*
Research efforts have been devoted to topics highly relevant to CTBT monitoring issues. Research involved the following topics: 1. NATO ASI Symposium in Alvor, Portugal 23 Jan – 1 Feb 1995 on CTBT monitoring; 2. Local event recordings; 3. Novaya Zemlya seismic events; 4. The seismology problems involving the Lg-blockage across geomorphical features like mountain ranges and grabens; 5. Simulating seismic wave propagation in the crust and upper mantle; 6. Three-dimensional finite-difference modeling of scattering from free surface topography; 7. The comparison of two and three dimensional finite-difference modeling of scattering from free surface topography; 8. Seismic source classification; 9. Signal site recognition.

19980205 048

14. SUBJECT TERMS
CTBT monitoring, seismic, two-dimensional, three-dimensional

15. NUMBER OF PAGES

16. PRICE CODE

17. SECURITY CLASSIFICATION OF REPORT	18. SECURITY CLASSIFICATION OF THIS PAGE	19. SECURITY CLASSIFICATION OF ABSTRACT	20. LIMITATION OF ABSTRACT
Unclassified	Unclassified	Unclassified	UL

2D & 3D MODELLING OF SEISMIC WAVE PROPAGATION IN THE HETEROGENEOUS LITHOPHERE IN THE CONTEXT OF NUCLEAR TEST BAN MONITORING

Eystein S. Husebye & Bent O. Ruud
Institute of Solid Earth Physics
University of Bergen
Norway

15 January 1998

Final Technical Report for Period 15 May 1994 – 14 Aug 1997

REPORT DOCUMENTATION PAGE	Form Approved OMB No. 0704-0188

1a. REPORT SECURITY CLASSIFICATION Unclassified	1b. RESTRICTIVE MARKINGS
2a. SECURITY CLASSIFICATION AUTHORITY	3. DISTRIBUTION/AVAILABILITY OF REPORT Approved for public release; Distribution unlimited
2b. DECLASSIFICATION/DOWNGRADING SCHEDULE	

4. PERFORMING ORGANIZATION REPORT NUMBER(S)	5. MONITORING ORGANIZATION REPORT NUMBER(S)

6a. NAME OF PERFORMING ORGANIZATION University of Bergen	6b. OFFICE SYMBOL (If applicable)	7a. NAME OF MONITORING ORGANIZATION Air Force Office of Scientific Research
6c. ADDRESS (City, State, and ZIP Code) Institute of Solid Earth Physics, University of Bergen, Allegt. 41, N-5007 Bergen, Norway		7b. ADDRESS (City, State, and ZIP Code) Building 410 Bolling AFB D C 20332-6448

8a. NAME OF FUNDING/SPONSORING ORGANIZATION AFOSR	8b. OFFICE SYMBOL (If applicable) NL	9. PROCUREMENT INSTRUMENT IDENTIFICATION NUMBER F49620-94-1-0278
8c. ADDRESS (City, State, and ZIP Code) Building 410 Bolling AFB D C 20332-6448		10. SOURCE OF FUNDING NUMBERS

PROGRAM ELEMENT NO.	PROJECT NO.	TASK NO.	WORK UNIT ACCESSION NO.

11. TITLE (Include Security Classification)
2D & 3D modelling of seismic wave propagation in the heterogeneous lithosphere in the context of nuclear test ban monitoring

12. PERSONAL AUTHOR(S)
Eystein S. Husebye, Bent O. Ruud

13a. TYPE OF REPORT Final Report	13b. TIME COVERED FROM 94.05.15 TO 97.08.14	14. DATE OF REPORT (Year, Month, Day) 1998 January 15	15. PAGE COUNT

16. SUPPLEMENTARY NOTATION

17. COSATI CODES			18. SUBJECT TERMS (Continue on reverse if necessary and identify by block number)
FIELD	GROUP	SUB-GROUP	2D & 3D synthetics including topography, Lg blocking, near real time event location, site recognition

19. ABSTRACT (Continue on reverse if necessary and identify by block number)
Work efforts in the reporting period have been devoted to topics being highly relevant to CTBT monitoring issues. Research accomplishments are;

(i) Our NATO ASI Symposium in Alvor, Portugal 23 Jan-1 Feb, 1995 on CTBT monitoring was rated a great success. The final outcome of this undertaking was the book: E.S. Husebye and A.M. Dainty (eds): Monitoring a Comprehensive Test Ban Treaty, Kluwer Academic Publ., Doordrecht, The Netherlands, pp 836, 1995. The book contains contributions from many scholars on most CTBT issues albeit with emphases on seismic monitoring. More than 100 key lecturers and students attended the symposiom including 10 scientists and nuclear physicists from the former Soviet Union.

(ii) Local event recordings are complex in the sense that relevant P- and S-phases vary in an unpredictable manner even between closely spaced stations; thus, manual analysis of such records is still commonplace. Our approach to solving this long standing problem of observational seismology is to bandpass filter (3-6 Hz) to ensure good SNR and then form envelopes to ensure simple signals across a seismograph network. The physical basis is that Pg and Lg are crustal

20. DISTRIBUTION/AVAILABILITY OF ABSTRACT ☐ UNCLASSIFIED/UNLIMITED ☐ SAME AS RPT. ☐ DTIC USERS	21. ABSTRACT SECURITY CLASSIFICATION Unclassified	
22a. NAME OF RESPONSIBLE INDIVIDUAL Dr. Stanley K. Dickinson	22b. TELEPHONE (Include Area Code) (202) 767-4964	22c. OFFICE SYMBOL AFOSR/NL

DD Form 1473, JUN 86   Previous editions are obsolete.

waveguide phases reflecting P- and S-energy propagation. Extensive tests on envelope analysis of local records from different areas found that arrival times of the maxima of Pg and Lg envelopes increase very consistently with distance even in different tectonic regimes. Typical velocities being 6.1 and 3.5 km/sec respectively. These arrival time parameters are easy to extract in an semi-automatic manner and are highly suitable for local epicenter determinations. Extensive tests on locating mining explosions were conducted and on average the 'envelope' location errors relative to 'true' locations were similar to those in bulletins which are based on conventional phase pickings. Occasionally the Pg/Pn envelope may be very weak but can be replaced by the easily pickable (non-envelope) Pn-phase. Additional advantages with envelope locations are transportability (not overly sensitive to details of crustal structure), and that envelope amplitudes can be directly converted to ground motion and magnitudes. For modern stations envelopes can be formed in situ with low sampling rates of 1-2 Hz thus greatly reducing transmission costs.

(iii) Novaya Zemlya (NZ) seismic events always stir interest among seismologists and politicians alike; the issue is whether a clandestine nuclear explosion has taken place at or near the former USSR nuclear test site or simply an earthquake occured. In this regard the NZ event of 13 Jan, 1996 was of particular interest because epicenter locations as provided by various seismologist groupings varied by more than 100 km and even location confidence ellipses did not overlap. We were asked by German colleagues to look into this epicenter location controversy and in particular to analyze 3-component recordings from the Norilsk station in Siberia (operated by IRIS). Other seismologists had ignored these recordings presumably due to 'spiky' records (local electric outgauges) and besides relatively high noise levels. Using our new envelope processing technique we were able to extract Pn- (somewhat doubtful) and Sn-arrival times (reliable). Using these additional phase readings in combination with Pn- and Sn-phase readings from ARCESS and Spitsbergen arrays we obtained an epicenter location at 75.38 N; 56.55 E that is on the NW Coast of Novaya Zemlya. Part of the controversy bearing on this particular event was tied to an early epicenter location westward in the Barents Sea. We demonstrated that significant seismic phase information could be extracted from 'poor' records and that the commonly used IASPEI travel time tables are inadequat for Novaya Zemlya and adjacent regions.

(iv) An intriguing problem in seismology is the Lg-blockage across geomorphical features like mountain ranges and grabens. The North Sea grabens are the classical example here with nearly total blockage for certain wave paths. Such observations are explained in terms of distortion or destruction of the crustal waveguide due to crustal thinning. This hypothesis was extensively tested by successively thinning North Sea crystalline crustal models down to 5 km – still more than 50 % of Lg-energy 'survived' in the synthetic seismograms after graben passages. Very similar results have recently been published by other scientists albeit denoted as graben Lg-blockage. Even introducing as much as 8 % RMS velocity pertubations within the graben area proper did not prevent Lg passage. Rough calculations indicated that a low Q-value of the order of 50 would suffice for near total Lg- blockage in combination with crustal thinning effects. In interesting observational feature was that in cases of Lg-blockage correspondingly the Sn and its coda were strong and vice versa. This implies that Lg energy is leaking out of the crustal waveguide into the upper mantle and outside the graben area reemerge at the free surface as Sn-waves.

(v) We are continuing our efforts on simulating seismic wave propagation in the crust and upper mantle. In this regard we have considered the problem of proper boundary conditions in 2D FD wavefield modeling. Two methods of grid boundary absorption were investigated and associated performances compared. Two methods of grid wave absorption are investigated and compared; the recent Optimal Absorbing Boundary Condition (Peng and Toksoz, J. Acoust. Soc. Am., 1994) and the Exponential Damping (a variant of Cerjan et. al., Geophysics, 1985). A staggered 8th order accurate spatial finite-difference discretization applied to the velocity-stress formulation of the elastic wave equations is used. A free, plane surface is incorporated at the top boundary, while absorbing boundary conditions are employed along the remaining grid boundaries. We find conditions for achieving stable results when applying these methods in the specific computational environment. The respective merits are also compared using both a homogeneous model and a more realistic model consisting of several tilted layers. The main result is that the ED formulation

gives better edge absorbing properties than that of the OABC method.

(vi) As mentioned in (iv) the 2D FD synthetics illustrate in an instructive manner seismic wave propagation in complex media albeit coda excitation appears somewhat weaker than seen in real records. Intuitively, we expect that 3D models would generate relative more coda waves and in this regards experiments have been carried out to model scattering from free surface topography near the NORESS array. Three-dimensional (3-D) finite-difference (F-D) modeling of scattering from free surface topography has been pursued. A velocity stress formulation of the full elastic wave equations with exact boundary conditions for a free surface topography has been numerically modelled by an 8th order finite--difference method on a staggered grid. We have simulated scattering from teleseismic P-waves using a plane, vertically incident P-wave and real topography from a 40x40 km area centered at the NORESS array in south-eastern Norway. Snapshots and synthetic seismograms of the wavefield show clear conversion from P to Rg (short period fundamental mode Rayleigh) waves in an area of rough topography approximately 10 km east of NORESS. This result is consistent with numerous observations. By the recent parallellization of the program code using MPI (Message Passing Interface), new possibilities have been opened for modeling higher frequencies and/or larger areas than so far conducted. A more complete 3-D modeling of the observational area can be realized.

(vii) We have pursued and compared two- and three-dimensional (3-D) finite-difference (F-D) modeling of scattering from free surface topography. A velocity-stress formulation of the full elastic wave equations are combined with exact boundary conditions for the surface topography and numerically discretized by an 8th order F-D method on a staggered grid. We have simulated scattering in 2-D and 3-D from teleseismic P-waves using a plane, vertically incident P-wave and real topography from a 60 by 60 km area including the NORESS array in south-eastern Norway. Many field observations that are not easily explained by simpler 2-D cases are shown to better match qualitative effects from 3-D surface topography modeling. These include strong amplifications at hills, complex wave pattern caused by scattering, and directivity of scattered waves. Snapshots and seismograms show clear conversion from P- to Rg- (short period fundamental mode Rayleigh) waves in an area of rough topography in the vicinity of the array site. All results are consistent with numerous observations. By parallellization of the original software, possibilities have been opened for modeling with higher resolution and/or larger areas than before.

(viii) An essential element in nuclear test ban monitoring is that of seismic source classification; earthquake or underground nuclear explosion ? An additional complexity of this issue is that numerous signals stemming from mining and quarry explosions (chemical) are recorded daily and hence contribute significantly to the workload on the monitoring system. An outstanding feature of this kind of industrial activities is the spatial stationarity of the explosion sites which often are less than 1 km in aperture. In other words, a scheme for automatically recognizing the seismic 'signature' of chemical explosion sites would greatly reduce the daily monitoring workload. Basic assumption here, well established observationally, is that of seismic waveform similarities for closely spaced explosions and also even aftershocks (earthquakes). In many industrialized countries of low seismicity more than 90 % of seismic event recordings stem from chemical explosions and thus contribute significantly to the daily analyst workload. In this study we explore the possibility of using waveforms from a priori known explosion sites (learning) for recognizing subsequent explosions from the same site excluding any analyst interference. To ensure high signal correlation while retaining good SNRs we used envelope transformed waveforms including both the P and Lg arrivals. To ensure good spatial resolution we used multistation (network) recordings. An interpolation and approximation neural network scheme was used for learning the computer to recognize new explosion recordings from a spesific site using detector output event files of waveforms only. The analysis output is a single number between 0-1 and on this scale an acceptance threshold of 0.4 proved appropriate. We obtained 100 % correct decisions between two sets of 'site explosions' and hundreds of 'non-site' explosions/earthquakes using data files from the Norwegian Seismograph Network.

(ix) Another possible approach to signal site recognition (see viii) is to replace multistation (z-component only) with single station 3-component recordings. Instead of using envelope transformed records we may introduce complex trace modulation so the signal covariance

matrix would have 9 different time elements. As is well known from many source studies both high and low signal frequency information contributes significantly to good classification performances so we formed covariance matrixes for 12 different frequency bands. In other words, a single 3-component event recording was in our new neural net signal recognition scheme by 9 x 12 = 108 pieces of time observation. Ground truth information was obtained for two underwater construction sites at Mongstad and Geiranger, W. Norway and 4 - 6 events were used in establishing the respective learning sets. Testing on hundreds of event recordings with epicenters adjacent to the two construction sites produced excellent results, that is all construction explosions were recognized as such while all other events were classified as non-site events. Probabilities of a 'false alarm' or a 'missed detection' (presuming score values to be Gaussian) were of the order of 1:1,000,000. We also checked the relative merits (contributions) of individual filter bands and found that the 3 - 6 Hz and the 8 - 12 Hz segments were most informative. This is somewhat surprising since these two signal segments are also most informative in the context of discrimination between explosion and earthquake sources.

Contents

1 Objectives

- Foster a better understanding of seismic wave propagation in complex lithospheric media.

- Principal modeling tool is 2-D and 3-D finite difference (FD) synthetics for models also including surface topography.

- Corroborating synthetics through analysis of array and network data.

- Use 'synthetic' knowledge in design of event classification schemes.

- Seismic network performance and real time event location.

- Automated explosion site spesific signal recognition

2 Status of effort

Much efforts have been spent on expanding to 3D models and streamlining our finite difference (FD) wavefield simulation scheme including code adaption for parallel computers. The latest extension here is to include intrisic attenuation or damping that is numeric solutions of the vico-elastic wave equations in 2D and 3D. The 3D FD modeling of topography wavefield responses in the NORESS array siting area are rated a success; we are able to reconstruct realistically the P-to-Rg scattering fields with a 'secondary' source in the Bronkeberget hills. Using the 2D FD variant we have also simulated Lg-blockage across the North Sea graben structures. Partial blockage of Lg is tied to crustal thinning with Lg leaking out of the waveguide in the form of Sn-waves. Significant Lg decay is also caused by Lg-to-Rg conversions in the overlying sediment strata and by intrinsic attenuation. In a CTBT monitoring context, near real time event classification is essential at least in the local epicenter distance range. First step of our efforts here have been to design an automatic event detection and epicenter location scheme. It is very robust and when the locations are compared with known mining sites, the results appear very accurate. More realistic real time testing is planned in cooperation with colleagues at the German National Data Center (NDC) in Hannover. Jointly with our German colleagues we analyzed a presumed 'suspecious' event taking place on the NW Coast of Novaya Zemlya 13 Jan. 1996; outcome was that there was no strong evidence that this event could be a clandestine nuclear explosion. Numerous mining and quarry sites generate seismic signals which constitute a heavy workload on any CTBT monitoring system. Since explosion sites are spatially stationary signal records from a spesific site are rather similar. We have exploited this this observational fact by designing a neural net scheme for automatically recognizing site spesific signals thereby eliminating any need for analyst interference. In fact, we have exploited two approaches here; one using signal envelopes from a set (3 - 6) of network stations (flexibel choices) and the other one tied to single station 3-component recordings. In the latter case we used the 'complex modulated' covariance matrix for a 12-suit of bandpass filters so one event record was equivalent to 9x12 = 108 pieces of time information. Use of single station recordings were in part motivated by network timing errors. Both 'site recognition' schemes had excellent performances when tested on local explosion recordings in W. Norway for which 'Ground Truth' information was available.

3 Final work effort - a personal farewell

The Principal Investigator, Eystein S. Husebye, was introduced to US Nuclear Monitoring Research (VELA Uniform Program) a long time ago, that is, in May 1966 when offered a Post. Doc. Fellowship for studies at MIT, Cambridge, MA. Afterwards employed as Director of Research (1968 - 1993) at NORSAR (The Norwegian Seismic Array), Kjeller, Norway which construction and subsequent operation for many, many years were mainly sponsored by AFTAC and ARPA. From 1991 - 1997 PI's (our) seismic monitoring research have been sponsored by the Air Force Office of Scientific Research (AFOSR) Bolling AFB and managed by Phillips Laboratory, Hanscom AFB. Pi's longstanding involvement with various US Defense and Air Force agencies have been intellectually very stimulating and personally rewarding in terms of an above average scientific and seismological career. In the latter case, to be more spesific, editor of 2 books on nuclear test bam monitoring, more than 150 technical reports and scientific journal contributions and organizer/convener for numerous international symposia, conferences and NATO ASIs. In short, Eystein S. Husebye is very grateful for the many research opportunities offered by participation in the many US sponsored scientific programs within the fields of nuclear test ban monitoring and basic seismology - these wordings are just a very modest way of expressing this gratitude.

4 Accomplishments

In the following a short summary of each subject is given. The complete papers appear in appendices. Some of the topics listed were included in our previous Interim Project Report; reason for this is that the relevant reports (4.4, 4.5, 4.6) have been significantly modified or is now appearing as journal publication. Sec. 4.1 is an exception since organizing a NATO Advanced Study Institute and subsequently editing an important book on Nuclear Monitoring is rated a major accomplishment and hence repeated here.

4.1 NATO ASI symposium & book on CTBT monitoring

Our NATO ASI Symposium in Alvor, Portugal 23 Jan–1 Feb, 1995 on CTBT monitoring was rated a great success. The final outcome of this undertaking was the book: E.S. Husebye and A.M. Dainty (eds): Monitoring a Comprehensive Test Ban Treaty, Kluwer Academic Publ., Doordrecht, The Netherlands, pp 836, 1995. The book contains contributions from many scholars on most CTBT issues albeit with emphases on seismic monitoring. More than 100 key lecturers and students attended the symposiom including 10 scientists and nuclear physicists from the former Soviet Union.

4.2 Local event location in an automatic manner

Local event recordings are complex in the sense that relevant P- and S-phases vary in an unpredictable manner even between closely spaced stations; thus, manual analysis of such records is still commonplace. Our approach to solving this long standing problem of observational seismology is to bandpass filter (3–6 Hz) to ensure good SNR and then form envelopes to ensure simple signals across a seismograph network. The physical basis is that Pg and Lg are crustal waveguide phases reflecting P- and S-energy propagation. Extensive tests on envelope analysis of local records from different areas found that arrival times of the maxima of Pg and Lg envelopes increase very consistently with distance even in different tectonic regimes. Typical velocities being 6.1 and 3.5 km/sec respectively. These arrival time parameters are easy to extract in an semi-automatic manner and are highly suitable for local epicenter determinations. Extensive tests on locating mining explosions were conducted and on average the 'envelope' location errors relative to 'true' locations were similar to those in bulletins which are based on conventional phase pickings. Occasionally the Pg/Pn envelope may be very weak but can be replaced by the easily pickable (non-envelope) Pn-phase. Additional advantages with envelope locations are transportability (not overly sensitive to details of crustal structure), and that envelope amplitudes can be directly converted to ground motion and magnitudes. For modern stations envelopes can be formed in situ with low sampling rates of 1-2 Hz thus greatly reducing transmission costs.

4.3 Relocating the 13 January 1996 Novaya Zemlya seismic event

Novaya Zemlya (NZ) seismic events always stir interest among seismologists and politicians alike; the issue is whether a clandestine nuclear explosion has taken place at or near the former USSR nuclear test site or simply an earthquake occured. In this regard the NZ event of 13 Jan, 1996 was of particular interest because epicenter locations as provided by various seismologist groupings varied by more than 100 km and even location confidence ellipses did not overlap. We were asked by German colleagues to look into this epicenter location controversy and in particular to analyze 3-component recordings from the Norilsk station in Siberia (operated by IRIS). Other seismologists had ignored these recordings presumably due to 'spiky' records (local electric outgauges) and besides relatively high noise levels. Using our new envelope processing technique we were able to extract Pn- (somewhat doubtful) and Sn-arrival times (reliable). Using these additional phase

readings in combination with Pn- and Sn-phase readings from ARCESS and Spitsbergen arrays we obtained an epicenter location at 75.38 N; 56.55 E that is on the NW Coast of Novaya Zemlya. Part of the controversy bearing on this particular event was tied to an early epicenter location westward in the Barents Sea. We demonstrated that significant seismic phase information could be extracted from 'poor' records and that the commonly used IASPEI travel time tables are inadequat for Novaya Zemlya and adjacent regions.

4.4   *Lg*-blockage across North Sea grabens

The North Sea *Lg*-blockage for wave paths across the crustal graben structures is a well-established observational fact. Analysis of such observations implies that *Lg*-blockage takes place in graben areas associated with sedimentary basin formation and crustal thinning. These intriguing observations have triggered many theoretical studies aimed at highlighting specific *Lg* loss mechanisms albeit so far with only moderate success. Our approach to this problem is to simulate seismic wavefield propagation through the crustal waveguide using 2D finite difference techniques. ¿From oil exploration works in the North Sea the graben structures are known in detail which enabled us to use realistic crustal models in our *Lg* synthetics. In the most extreme model tested, the crystalline crust thickness beneath the graben amounted to only 5 km while the overlying sedimentary pile is nearly 10 km thick. At the base of the crust the Moho is elevated nearly 10 km below the graben. This model has similarities to the oceanic crustal waveguide where total *Lg*-blockage is claimed for path lengths exceeding 100 km. The synthetic wavefields are displayed in terms of snapshots, semblance velocity analysis and time-space RMS amplitudes. The dominant structural *Lg* loss mechanisms are *Lg*-to-*Rg* conversions (scattering) in the sediments and *S*-wave leakage out of the crustal waveguide and into the upper mantle. Part of these upper mantle *S*-waves return to the crust and appears as *Sn* coda. Observationally, strong *Sn*-phases of long duration are often associated with weak *Lg*-phases and vice versa. Our synthetics produced *Lg* amplitude decay amounting at most to 6-10 dB while observational data imply blockage amounting to 15-20 dB. The latter is equivalent to *Pn-Lg* magnitude difference of nearly one magnitude unit. The main outcome of this study is therefore that *Lg*-wave propagation is very robust and that a dominant blockage effect associated with intrinsic attenuation, that is Q values of the order of 100 at 2 Hz for a path length of minimum 100 km, is necessary to conform to observations.

4.5   Boundary conditions in 2D FD modelling

Two methods of grid wave absorption are investigated and compared; the recent Optimal Absorbing Boundary Condition (Peng and Toksøz, J. Acous. Soc. Am., 1994) and the Exponential Damping, a variant of Cerjan et. al. (Geophysics, 1985). A staggered 8th order accurate spatial finite-difference discretization applied to the velocity-stress formulation of the elastic wave equations is used. A free, plane surface is incorporated at the top boundary, while absorbing boundary conditions are employed along the remaining grid boundaries. We find conditions for achieving stable results when applying these methods in the specific computational environment. The respective merits are also compared using both a homogeneous model and a more realistic model consisting of several tilted layers.

4.6   3D FD modeling of scattering from topography

Three-dimensional (3–D) finite–difference (F–D) modeling of scattering from free surface topography has been pursued. A velocity stress formulation of the full elastic wave equations with exact boundary conditions for a free surface topography has been numerically modelled by an 8th order finite–difference method on a staggered grid. We have simulated scattering from teleseismic *P*-waves using a plane, vertically incident *P*-wave and real topography from a 40 × 40 km area

5

centered at the NORESS array in south-eastern Norway. Snapshots and synthetic seismograms of the wavefield show clear conversion from P to Rg (short period fundamental mode Rayleigh) waves in an area of rough topography approximately 10 km east of NORESS. This result is consistent with numerous observations. By the recent parallellization of the program code using MPI (Message Passing Interface), new possibilities have been opened for modeling higher frequencies and/or larger areas than so far conducted. A more complete 3-D modeling of the observational area can be realized.

4.7   3-D versus 2-D finite difference seismic synthetics

We have pursued and compared two- and three-dimensional (3-D) finite-difference (F-D) modeling of scattering from free surface topography. A velocity-stress formulation of the full elastic wave equations are combined with exact boundary conditions for the surface topography and numerically discretized by an 8th order F-D method on a staggered grid. We have simulated scattering in 2-D and 3-D from teleseismic P-waves using a plane, vertically incident P-wave and real topography from a 60 by 60 km area including the NORESS array in south-eastern Norway. Many field observations that are not easily explained by simpler 2-D cases are shown to better match qualitative effects from 3-D surface topography modeling. These include strong amplifications at hills, complex wave pattern caused by scattering, and directivity of scattered waves. Snapshots and seismograms show clear conversion from P- to Rg- (short period fundamental mode Rayleigh) waves in an area of rough topography in the vicinity of the array site. All results are consistent with numerous observations. By parallellization of the original software, possibilities have been opened for modeling with higher resolution and/or larger areas than before.

4.8   Recognizing explosion sites without seismogram readings

An essential element in nuclear test ban monitoring is that of seismic source classification; earthquake or underground nuclear explosion ? An additional complexity of this issue is that numerous signals stemming from mining and quarry explosions (chemical) are recorded daily and hence contribute significantly to the workload on the monitoring system. An outstanding feature of this kind of industrial activities is the spatial stationarity of the explosion sites which often are less than 1 km in aperture. In other words, a scheme for automatically recognizing the seismic 'signature' of chemical explosion sites would greatly reduce the daily monitoring workload. Basic assumption here, well established observationally, is that of seismic waveform similarities for closely spaced explosions and also even aftershocks (earthquakes). In many industrialized countries of low seismicity more than 90 % of seismic event recordings stem from chemical explosions and thus contribute significantly to the daily analyst workload. In this study we explore the possibility of using waveforms from a priori known explosion sites (learning) for recognizing subsequent explosions from the same site excluding any analyst interference. To ensure high signal correlation while retaining good SNRs we used envelope transformed waveforms including both the P and Lg arrivals. To ensure good spatial resolution we used multistation (network) recordings. An interpolation and approximation neural network scheme was used for learning the computer to recognize new explosion recordings from a spesific site using detector output event files of waveforms only. The analysis output is a single number between 0-1 and on this scale an acceptance threshold of 0.4 proved appropriate. We obtained 100 % correct decisions between two sets of 'site explosions' and hundreds of 'non-site' explosions/earthquakes using data files from the Norwegian Seismograph Network.

4.9   Signal site recognition using single station 3-component records

As mentioned, seismic waveform similarities for closely spaced explosions are well established ob-
servationally. Also, encouraged by our previous site recognition results we considered additional
flexibility in our approach to this problem essentially how to incorporate additional seismic record
information in the neural network analysis. Another motivation here was to safeguard against
technical defects like timing errors which otherwise would ruin multistation analysis. The alter-
native strategy choosen for extracting relative comprehensive signal attributes was that of using
single station 3-component (3C) records. By introducing complex demodulated record operations
(including both the P- and S-wave arrivals and part of the coda) the 3C covariance matrix would
contain 3x3 elements of different time information. From other source classification studies we
know that both explosion and earthquake spesific information are contained in several frequency
bands so we formed covariance matrixes for a suit of 12 different frequency bands. In other words,
a single 3C station event record produced 9x12 = 108 pieces of time information. Having access
to 'ground truth' information from 2 underwater construction sites (Mongstad and Geiranger)
we had 4 - 6 events (enough) for site recognition learning sets. Obtained results were excellent;
all events from the construction sites (not in learning sets) were classified as such while all other
events (more than 200) were classified as non-site events whether source was an explosion or an
earthquake. Presuming log-normal distribution of the neural network output score factor we esti-
mated that the probabilities of false alarm or missed 'detection' were less than 1:1,000,000. Also,
spatial resolution was good (less than 10 km) even perpendicularly to the station-site azimuth
direction. During this 3C site recognition exercise we found in the epicenter map used, 2 cluster of
events with which origin times were mainly between 10. - 14. hours that is prime working hours.
Selecting events directly from bulletin for learning sets but without ground truth information at
hand did produce results somewhat less convincing in comparision to those obtained for Mongstad
and Geiranger. This kind of problems, lack of ground truth information for appearant event clus-
ters, would in future be addressed through an initial multivariate analysis scheme in order to sort
out 'most similar' event recordings and hence the likely event candidates for learning sets.

5 Personnel Supported

Principal Investigator: Prof. Eystein S. Husebye

AFOSR project full-time researcher: Dr. Bent O. Ruud

Ph.D student: C. Deniz Mendi (thesis defence March, 1996; now in Istanbul)
Ph.D student: Stig Hestholm (now at Rice University, Houston, TX)
Master student: Tor Vegar Maardalen (completed May 1996)
Master student: Bjorn Heincke (Albrecht University, Kiel, FRG)

Other persons associated with project:
Dr. Yu. V. Fedorenko (Kola Sci. Center, RAS, Apatity,Russia)
Dr. Matti Tarvainen (Institute of Seismology, UoHelsinki, Finland)
Dr. Gennady A. Ryzhikov (gone)
Dr. Marina S. Biryulina (gone)
Dr. Andrej N. Gashin (SYNAPSE, Moscow, Russia)
Dr. Yann Grundt (University of Bergen)

6 Publications

Husebye, E.S. and Dainty, A.M. (eds.), 1996. Monitoring a Comprehensive Test Ban Treaty, NATO ASI Series E, Kluwer Academic Publishers, Dordrecht, The Netherlands, pp. 836.

Mendi, C.D., 1996. Prospects for On-line Analysis of Seismic Records and Their 2-D Finite Difference Synthesis, dr. scient. dissertation, February 1996, University of Bergen, Norway.

Mendi, C.D. and Husebye, E.S., 1995. Near Real Time Estimation of Seismic Event Magnitude and Moment via P and Lg Phases. In: Console, R. and Nikolaev, A. (eds.), Earthquakes Induced by Underground Nuclear Explosions, NATO ASI Series 2, Springer Verlag, Berlin, Germany.

Ryzhikov, G.A., Biryulina, M.S. and Husebye, E.S., 1996. A novel Approach to Automatic Monitoring of Regional Seismic Events, IRIS Newsletters, Vol. XV, 12–14.

Mendi, C.D., Ruud, B.O. and Husebye, E.S., 1997. The North Sea Lg-blockage Puzzle, Geophys. J. Int., 130, 669-680.

Hestholm, S., Ruud, B.O. and Husebye, E.S., 1997. Finite Difference Modeling of Elastic Waves in 3-D Including Free Surface Topography. In: F. J. Seron and F. J. Sabadell (eds.), High Performance Computing in Seismic Modelling, Zaragoza, Spain, in press.

Henger, M., Koch, K., Ruud, B.O., and Husebye, E.S., 1997. Comments on "The Political Sensitivity of Earthquake Locations" by van der Vink and Wallace, IRIS Newsletter, XVI, 20 - 22.

Hestholm, S. and Ruud, B., 1998. 3-D Finite Difference Elastic Wave Modeling including Surface Topography, Geophysics, in press.

Simone, A. and Hestholm, S., 1998. Instabilities in applying Absorbing Boundary Conditions to High Order Seismic Modeling Algoritms, Geophysics, in press.

Husebye, E.S. and Ruud. B.O. Seismic Wave Propagation in the Crust - Event Location in a semiautomatic Manner. In M.J. Shore, R.S. Jih, A.M. Dainty and J. Erwin (eds), Proceedings of The 19th Annual Seismic Research Symposium on Monitoring a Comprehensive Test Ban Treaty, Orlando, FL, 23-25 Sept. 1997, Technical Report, DSWA/Special Programs, Alexandria, VA.

Husebye, E.S., Ruud, B.O. and Dainty, A.M., 1998. Robust and Reliable Epicenter Determinations: Envelope Processing of Local Network Data, Bull. Seism. Soc. Am., 88, in press.

Federenko, Yu.V., Husebye, E.S., Heincke, B. and Ruud, B.O., 1998. Recognizing Explosion Sites

without Seismogram Readings: Neural Network Analysis of Envelope transformed Multistation SP Recordings 3-6 Hz, Geophys. J. Int., in press.

Tarvainen, M., Tiira, T. and Husebye, E.S., 1998. Locating near field Seismic Events with Global Optimization based on Interval Arithmetic, Geophys. J. Int., in press.

Hestholm, S., Ruud, B.O. and Husebye, E.S., 1998. 3-D versus 2-D Finite difference seismic synthetics including Real Surface Topography. IASPEI Conference Proceeding, PEPI, m/s in preparation.

Fedorenko, Yu. V., Husebye, E.S. and Ruud, B.O., 1998. Explosion Site Recognition using single station 3-component Event Records: IASPEI Conference Proceeding, PEPI, m/s in preparartion

Husebye, E.S. and Dowla, F.U. (eds): Seismological Data and Practise - Beyond Year 2000. Proceedings of IASPEI S20 Symposium at the 29 th General Assembly, Thessaloniki, Greece, Aug., 1997, volume in preparation.

7 Interactions

7.1 Presentations at conferences

Husebye, E.S. and Mendi, C.D.: Near Real Time Magnitude and Moment Estimation, NATO ASI on Monitoring a Comprehensive Test Ban Treaty, Jan. 23–Feb. 2, 1995, Alvor, Portugal.

Ruud, B.O., Grundt, Y., and Husebye, E.S.: A Comparison of tau-sum velocity-depth inversion for a perturbed and unperturbed crustal model, NATO ASI on Monitoring a Comprehensive Test Ban Treaty, Jan. 23–Feb. 2, 1995, Alvor, Portugal.

Ruud, B.O., Hestholm, S. and Husebye, E.S.: Finite Difference Modelling of Seismic Waves in a Heterogeneous Lithosphere, NATO ASI on Monitoring a Comprehensive Test Ban Treaty, Jan. 23–Feb. 2, 1995, Alvor, Portugal.

Hestholm, S. and Ruud, B.O.: 3D Finite Difference Elastic Wave Modeling Including Surface Topography, XXI General Assembly of IUGG, July 2–14, 1995, Boulder, CO, USA.

Husebye, E.S., Ryzhikov, G. and Birioulina, M.: Near real time event location from seismogram envelopes of local networks, XXI General Assembly of IUGG, July 2–14, 1995, Boulder, CO, USA.

Mendi, C.D. and Husebye, E.S.: Real Time Magnitude and Moment Estimation for Local Events, XXI General Assembly of IUGG, July 2–14, 1995, Boulder, CO, USA.

Ruud, B.O. and Hestholm, S.: Modeling Scattering from Surface Topography by 3D Finite Differences, XXI General Assembly of IUGG, July 2–14, 1995, Boulder, CO, USA.

Husebye, E.S. and Ruud, B.O.: Wavefield synthetics in 3D and fully automatic event locations, 17th Annual Seismic Research Symposium, Sept. 11–15, 1995, Scottsdale, AZ, USA.

Husebye, E.S., Ryzhikov, G. and Birioulina, M.: Fully automatic epicenter determinations of local events, 10th Anniversary of the FINESS array workshop on GSETT-3 and IMS, Oct. 12–14, 1995, Lahti, Finland.

Husebye, E.S., Ruud, B.O. and Hestholm, S.: Finite difference simulations of topography on seismic wavefields, 10th Anniversary of the FINESS array workshop on GSETT-3 and IMS, Oct. 12–14, 1995, Lahti, Finland.

Husebye, E.S., Mendi, C.D. and Ruud, B.O.: Lg blockage – finite difference synthetic simulation for graben structures, 10th Anniversary of the FINESS array workshop on GSETT-3 and IMS, Oct. 12–14, 1995, Lahti, Finland.

Mendi, C.D., Ruud, B.O. and Husebye, E.S.: Synthesizing Lg blockage across North sea graben

structures, European Geophysical Society XXI General Assembly, 6–10 May 1996, The Hague, The Netherlands.

Ryzhikov, G., Biryulina, M. and Husebye, E.S.: Epicenter location as a 3D tomography problem, European Geophysical Society XXI General Assembly, 6–10 May 1996, The Hague, The Netherlands.

Ruud, B.O. and Hestholm, S.: 3D finite difference elastic wave modeling including surface topography, European Geophysical Society XXI General Assembly, 6–10 May 1996, The Hague, The Netherlands.

Husebye, E.S. and Ruud. B.O. Seismic wave propagation in the crust - event location in a semi-automatic manner. Presented at The 19th Annual Seismic Research Symposium on Monitoring a Comprehensive Test Ban Treaty, Orlando, FL, 23-25 Sept. 1997.

Ruud, B.O. and Hestholm, S. Modeling of teleseismic P scattering from surface topography in SE Norway by 3-D finite differences, Presented at The 29th General Assembly of the IASPEI, Thessaloniki, Hellas, 18-28 Aug. 1997.

Hestholm, S., Husebye, E.S. and Ruud, B.O. Comparison between 3-D and 2-D Synthetic Seismic Scattering from Surface Topography in south-eastern Norway, Presented at The 29th General Assembly of the IASPEI, Thessaloniki, Hellas, 18-28 Aug. 1997.

Mendi, C.D., Ruud, B.O. and Husebye, E.S. The North Sea Lg-blockage puzzle, Presented at The 29th General Assembly of the IASPEI, Thessaloniki, Hellas, 18-28 Aug. 1997.

Husebye, E.S. and Ruud. B.O. Fast, Robust and Reliable Epicenter Determinations - Envelope Processing of Local Network Data. Presented at The 29th General Assembly of the IASPEI, Thessaloniki, Hellas, 18-28 Aug. 1997.

Fedorenko, Y., Husebye, E.S. and Ruud. B.O. Epicenter locations tied to ANN multidimentional envelope waveform recognition. Presented at The 29th General Assembly of the IASPEI, Thessaloniki, Hellas, 18-28 Aug. 1997.

7.2   Cooperative organizations

Inst. North Industrial Ecology Problems, RAS, Apatity, Kola, Russia
Seismology Division, Inst. Petro. Research and Geophysics, Holon, Israel
SYNAPSE Science Center/Moscow IRIS Data Analysis Center, Moscow, Russia
National Data Center, Rome, italy
National Data Center, Hannover, Germany
Institute of Seismology, Helsinki, Finland

8   Inventions and patent disclosures

None.

9   Honors

E.S. Husebye: Fellow Royal Astronomical Society, UK
E.S. Husebye: Member of European Geophysical Society's Beno Gutenberg Medal Committee.
E.S. Husebye: Convenorships: EGS 1996, IASPEI 1997, EGS 1997.

B.O. Ruud: Opponent at doctoral thesis defence at Helsinki University, Finland, Nov. 1995.

Appendix 1

Monitoring a
Comprehensive Test Ban Treaty

edited by

Eystein S. Husebye

Institute of Solid Earth Physics,
University of Bergen,
Bergen, Norway

and

Anton M. Dainty

Earth Sciences Division,
Phillips Laboratory/GPE,
Hanscom AFB, Massachusetts, U.S.A.

NATO ADVANCED STUDY INSTITUTE
Alvor, Portugal 23 January - 1 February 1995

MONITORING A COMPREHENSIVE
TEST BAN TREATY

Sponsored by and organized on behalf of the

SCIENTIFIC AND ENVIRONMENTAL AFFAIRS DIVISION
NORTH ATLANTIC TREATY ORGANIZATION

Co-sponsored by:

Air Force Office of Scientific Research, Directorate of Mathematics and Geoscience,
Bolling AFB, Washington DC, USA

Phillips Laboratory, Earth Science Division, US Air Force,
Hanscom AFB, MA, USA

US Air Force European Office of Aerospace Research and Development,
London, UK

Advisory Council for Arms Control and Disarmament,
Ministry of Foreign Affairs, Oslo, Norway

Junta Nacional de Investigacao Cientifca e Technologica, Lisbon, Portugal

Centro de Geofisica da Universidade de Lisboa, Lisbon, Portugal

Faculty of Science, University of Bergen, Norway

Scientific Directors:

Eystein S. Husebye	Anton M. Dainty	Alexander F. Kushnir	Luiz Mendes-Victor
University of Bergen,	Phillips Laboratory,	MDC IRIS/SYNAPSE,	University of Lisbon,
Bergen, Norway	Hanscom AFB, USA	Moscow, Russia	Lisbon, Portugal

Local Organizing Committee:

Luiz Mendes-Victor (Chairman), Paula Teves Costa, Carlos Sousa Oliveria,
Luisa Conde Senos, Luis M. Matias, Maria Fernanda Dias (secretary)

PREFACE

This NATO Advanced Study Institute addressed the problem of verifying compliance by signatories of a Comprehensive Test Ban Treaty (CTBT), including setting up a monitoring system that will detect treaty violations. The verification problem comprises a blend of political, scientific and technical issues, which have often been treated separately. The requirements of the system are set by political considerations; it must be based on scientifically sound principles; and it must be implemented technically in the real world.

The issue of a Comprehensive Test Ban Treaty (CTBT) has been on the U.N. political agenda for almost 40 years. As this is being written, it is an active topic: the Conference on Disarmament (CD) is working to draft such a treaty which will then be made available for any nation that wishes to sign. Another aspect of a CTBT is its place in the larger issue of non-proliferation of nuclear weapons. Again, this is an active topic as this is being written: negotiation of a CTBT was explicitly stated as a goal when the Non-Proliferation Treaty was recently renewed indefinitely. In the technical field, the Group of Scientific Experts (GSE), convened by the CD, is conducting its third Technical Test, known as GSETT-3. The intention of GSETT-3 is to produce a prototype system for seismological monitoring that, among other goals, can serve as a practical example for the negotiating community of what is technically feasible. Also, the CD has established special working groups on the non-seismic techniques of hydroacoustic, radionuclide, and infrasound monitoring, and on on-site inspection methods, as part of the process of drafting a CTBT.

In these Proceedings, the main focus will be on the scientific and technical aspects of seismic monitoring of underground nuclear tests. This particular topic was chosen because it is one of the main technical challenges of monitoring. However, we have also included the political issues and non-seismic techniques. Accordingly, the Proceedings of the ASI have been arranged so that a general overview of the problem of monitoring is given in the first section, with a more detailed exposition of the technical practice and problems of seismic monitoring following, and papers on future directions in the last section. The overview section includes contributions about political background and developments, and technical reviews of the latest practice in testing and the non-seismic monitoring methods, including on-site inspection. Some, but not all, of the non-seismic methods are used for explosions which are not contained. These must be monitored, but it must be born in mind that current testing practice is to contain tests underground, and any compliance system must contain provisions for monitoring such events; hence, the focus on seismic monitoring in this ASI.

The specific nature of a CTBT, as compared to other treaties such as the Limited Test Ban Treaty banning all tests except underground or the Threshold Test Ban Treaty

- banning underground tests above a certain rather large threshold, imparts its own unique characteristics to a seismic monitoring system. First, a CTBT is intended to be multilateral and worldwide rather than bilateral or trilateral, thus any monitoring system must cover the globe and all environments: underground, underwater, atmosphere and space. Second, and technically much more important, all tests of any size would be banned under a CTBT, including small events. To monitor small underground events, it is necessary to record seismograms at relatively short ranges of 100-2000 km from the event, known in seismology as the regional distance range. This is a major change from current operational procedure in monitoring which is based at monitoring at distances beyond 2000 km, the teleseismic distance range: it has been known since the earliest days of seismology that seismograms at regional distances have quite different characteristics and frequency content than seismograms at teleseismic distances, due to the different parts of the earth that are sampled during propagation of the signal between source and receiver.

The new technological developments required by this shift to regional monitoring form an important part of the papers presented here. The operational process of seismic monitoring can be divided into detection of all seismic signals, location of all events, identification of the seismic events which are underground nuclear tests (known as "discrimination" in seismic monitoring), and estimation of the size (yield) of the nuclear explosions. In assessing the new problems of regional monitoring, it must of course be remembered that expertise from other fields in seismology, especially earthquake recording, is available, and indeed many of the resources of knowledge and equipment already in place will surely be used in monitoring a CTBT. However, such knowledge and equipment has been acquired to meet the needs of these fields, and will not always fit the requirements of seismic monitoring. The most pressing case is discrimination, since this is a subject that is unique to seismic monitoring. Furthermore, because of the higher frequency of regional signals compared to teleseismic, the most effective means of discrimination discovered for teleseismic signals (MS:mb) cannot be used for small events and new methods must be found. Accordingly, particular attention has been paid to discrimination.

The structure of the Proceedings is designed to cover the problems listed above. After opening with an overview section on Principal Political and Technical Test Ban Issues, a section on Monitoring Technologies gives a summary of all the methods being considered for monitoring a CTBT. Following this, the section Explosion and Earthquake Source Modelling examines underground nuclear tests and other disturbances as seismic sources. This examination includes the problem of decoupling (i.e., decoupling the explosion from the solid earth by detonating it in a cavity), which is probably the most credible way in which monitoring might be defeated. Following this the problem of monitoring such seismic sources is discussed in some detail, with sections on Seismic Networks, including detection and location of seismic events; Signal Processing and Seismic Wave Propagation, covering analysis methods specific to the seismic arrays used in regional monitoring and propagation of seismic waves at regional distances; and Seismic Source Discrimination Technologies, especially at regional distances. These topics cover three of the four classical steps of monitoring,

namely, detection, location, and discrimination; the signal analysis and wave propagation are included as the scientific basis for accomplishing this. A review paper on existing methods of yield estimation is included in the section on source modelling, but this topic has not been treated at greater length because in a CTBT, all tests of any size will be proscribed.

The subject of monitoring underground nuclear explosions has its points of controversy, technical and otherwise. In the NATO ASI, and in these Proceedings, our position has been to present as many points of view as possible and to encourage the contributors to put down there own points of view. We have made no effort to reconcile differing points of view, but simply present them for the reader to make his or her own judgments. Within these constraints, we hope these Proceedings give an accurate and succinct review of the state-of-the-art (or state-of-the-argument) of Monitoring a Comprehensive Test Ban Treaty. It can be said that the practically unanimous opinion of the ASI participants, as expressed in the scheduled discussion sessions, is that a Comprehensive Test Ban Treaty can be monitored in the technical sense, at least down to some yield; the arguments are over what that yield is.

A great deal of effort goes into organizing and running an ASI. We would like to express our sincere thanks to all who worked, often late into the night for many nights, to make this Conference possible. Particular thanks go to Prof. F. Tomas, the State Secretary of Science and Technology of Portugal, and Prof. R. Ribiero, President of Junta Nacional de Investigacao Cientifica e Tecnologica, Lisboa, Portugal, who found time in their busy schedules to attend and speak at the Opening Ceremonies. We are also indebted to our fellow Organizing Committee members Prof. Alexander Kushnir of the International Institute of Earthquake Prediction Theory and Mathematical Geophysics, Moscow, Russia, and Prof. Luis Mendes-Victor of the University of Lisboa, Portugal. Nothing would have been possible without the work of the Local Organizing Committee consisting of Prof. Mendes-Victor, Prof. Paula Costa, Prof. Carlos Oliveira, Dr. Luisa Senos, Dr. Luis Matia, and Fernanda Dias, all of the University of Lisboa; they have our gratitude for a smoothly run and enjoyable meeting.

<center>August 1995</center>

<center>

Eystein Husebye   Anton Dainty
Bergen, Norway   Boston, U.S.A.

</center>

Appendix 2

Robust and Reliable Epicenter Determinations:
Envelope Processing of Local Network Data

by Eystein S. Husebye, Bent O. Ruud, and Anton M. Dainty*

Abstract Local event recordings are complex in the sense that relevant P and S phases vary in an unpredictable manner even between closely spaced stations; thus, manual analysis of such records is still commonplace. Our approach to solving this long-standing problem of observational seismology is to bandpass filter (3 to 6 Hz) to ensure good signal-to-noise ratio SNR and then form envelopes to ensure simple signals across a seismograph network. The physical basis is that Pg and Lg are crustal wave-guide phases reflecting P- and S-energy propagation. Extensive tests on envelope analysis of local records from different areas found that arrival times of the maxima of Pg and Lg envelopes increase very consistently with distance even in different tectonic regimes, typical velocities being 6.1 and 3.5 km/sec, respectively. These arrival-time parameters are easy to extract in a semi-automatic manner and are highly suitable for local epicenter determinations. Extensive tests on locating mining explosions were conducted, and on average, the "envelope" location errors relative to "true" locations were similar to those in bulletins that are based on conventional phase pickings. Occasionally, the Pg/Pn envelope may be very weak but can be replaced by the easily pickable (nonenvelope) Pn phase. Additional advantages with envelope locations are transportability (not overly sensitive to details of crustal structure), and that envelope amplitudes can be directly converted to ground motion and magnitudes. For modern stations, envelopes can be formed *in situ* with low sampling rates of 1 to 2 Hz, thus greatly reducing transmission costs.

Introduction

A common assumption in local seismogram analysis is that the records are dominated by the four phases Pn, Pg, Sn, and Lg (replaced by Sg at short distances). These phases are associated with specific travel-time curves and propagation paths that in turn are used in epicenter determinations. This simple approach is now being questioned. For example, Pg and Lg are not adequately described as simple rays; they are essentially wave-guide phases including scattering contributions from crustal heterogeneity (Hestholm *et al.*, 1994.) At distances beyond about 100 km, the direct Sg signal is rather weak, hence the change of notation to Lg—the dominant crustal wave observable occasionally out to 3000 km (Nuttli, 1973; Hansen *et al.*, 1990). Since normally Pg and Lg are dominant over Pn and Sn, the signal envelopes of P- and S-wave arrivals are indicative of P- and S-energy transport in the crustal wave guide. An indication for this is that the Lg-wave group velocity is reported in the interval 3.4 to 3.6 km/sec for large parts of the continents (Mykkeltveit and Husebye, 1981).

For local epicenter determinations, preferences are to work with high signal frequencies ($f > 2$ Hz) where signal-to-noise ratio (SNR) is relatively high, thereby accepting the penalty of complex signal records. Low-frequency filtering typically results in simple records but poor SNR, thus this option is not of much interest. The greatest problem is that the shear wave rain (Sn and/or Lg) that typically is the most prominent feature in the seismogram often has an emergent onset. Hence, reliable phase picks are difficult to accomplish automatically, so these efforts remain essentially manual. When we contemplated this problem, the envelope processing introduced in NORSAR array surveillance appeared attractive (Ringdal *et al.*, 1975; Nuttli, 1973): Could this be a successful approach for automated analysis of complex local records as well? By envelope transforming such records, we obtain traces with excellent SNR (filter band 3 to 6 Hz used), but signals are not identical since local network apertures are often large. However, both PG and LG (envelope notations for Pg and Lg) peaks are sufficiently similarly shaped to warrant combined analysis operations based on 1D signal attributes; that is, envelope parameter variations depend on epicenter distance alone; the original signal waveforms do

*Present address: Defense Special Weapons Agency, Special Programs Division, 6801 Telegraph Road, Alexandria, Virginia 22310-3398.

not. By plotting envelope traces (Fig. 2), it is easy to verify the validity of this assumption (Fig. 3), and besides, *PG* and *LG* (their envelope peaks) propagate with velocities of approximately 6.1 and 3.5 km/sec, respectively, as expected for crustal wave-guide propagation. Ryzhikov *et al.* (1996) designed an ingenious scheme for joint *PG* and *LG* power location in time and geographical space, equivalent to epicenter determination. Conceptually, this has some similarities to global beamforming and threshold monitoring (Sereno and Bratt, 1989; Kværna and Ringdal, 1995). In essence, envelope location may be considered a variant of *f-k* analysis, tomography backprojection, or a "brute force" search for maximum power in geographical space as a function of time.

There are drawbacks with "envelope power" location schemes, namely, the common necessity of weighting the dominant *LG* signal, lack of resolution due to a broad *LG* peak, and loss of the relatively weak *PG* beyond about a 400-km distance. There is also the well-known problem that for *P*-only observations for events outside a network, gross errors may occur because origin time and distance are not well resolved, which is an incentive to use both *P* and *S* arrivals in spite of the difficulties. To avoid weighting and related problems, we decided to use the easily pickable *PG* and *LG* peak arrival times in a conventional epicenter location scheme as demonstrated below.

Time-Domain Envelope Location

Most local networks operate in a trigger mode; that is, only segmented data containing real signals are transmitted to the local hub for further analysis. Such data are used here, and after prefiltering in the 2 to 4 or 3 to 6 Hz passband, envelopes are formed: *LG* peaks are picked easily by computer as the maximum in the segment. A preliminary location is then made from these *LG* readings that in turn is used to predict the *PG* arrival windows, with subsequent *PG* arrival-time picking. In cases where *PG* readings are problematic, we may instead aim at reading the first phase arrival, *Pg* or *Pn* (Ruud and Husebye, 1992). Then with *PG* and *LG* (or *Pn* and *LG*, *Pg* and *LG*) paired arrival times, reliable epicenter determinations are feasible using any of several location algorithms. Our preference is the Ruud *et al.* (1993) grid-search routine, but we also used the fast Interval Arithmetics scheme of Tarvainen *et al.* (1997). Envelope traces for an event detected by the local Norwegian Seismic Network (NSN, Fig. 1) are shown in Figure 2, illustrating the ease by which *PG* and *LG* can be picked.

In order to find appropriate travel-time curves for the *PG* and *LG* peaks, we proceeded in the following manner. First *Pg* arrival times (first onsets) for nearby stations (distance less than 100 km) were read. Since station and epicenter coordinates are known, accurate origin times were easy to obtain assuming a *Pg* velocity of 6.1 km/sec. Then by plotting travel times for *PG* and *LG* peaks, it was simple to calculate linear travel-time curves in a least-squares sence
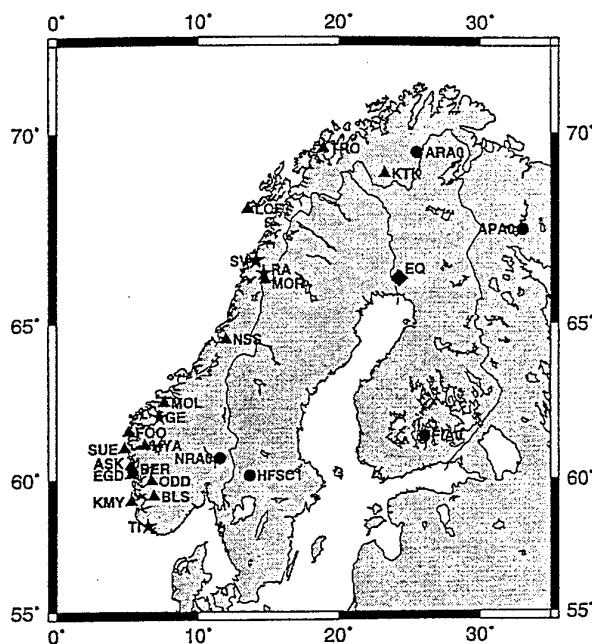

Figure 1.   The Norwegian Seismograph Network and Scandinavian array stations used in analysis. Explosion sites for which envelope location accuracy were tested (TI = Titania, GE = Geiranger, RA = Rana, SV = Svartisen) and an earthquake (EQ) location examined using the arrays are also shown. The Titania and Geiranger explosions are only recorded by S. Norway stations while the Rana and Svartisen explosions are only recorded by stations north of 65° N.

(Fig. 3) for Titania and Geiranger explosion recordings. The scattering in *PG* arrival times is larger than that of *LG*—not unexpected since the crustal wave guide is more pronounced for shear waves. Further refinements of these 1D time curves do not seem practical in view of lateral velocity and thickness variations of the crust (e.g., see Kinck *et al.,* 1993). A preferable alternative is to introduce spatial time corrections here (Shearer, 1997).

Network Analysis and Location Results

Mining Explosions in Norway

We used local explosion records from NSN stations (Fig. 1) to test the robustness and accuracy of our novel envelope epicenter determination scheme. Location performances are shown in Figure 4 for the four known explosion sites Titania, Geiranger, Rana, and Svartisen (Fig. 1). For Geiranger locations, station MOL is rather critical at an epicenter distance of only 55 km. However, at such close ranges, *PG* and *LG* are not well separated, so for MOL, *PG* time picks are available for only about 30% of the events. Geiranger locations by which all *PG* time picks (including the missing ones for MOL) are replaced by those of the an-
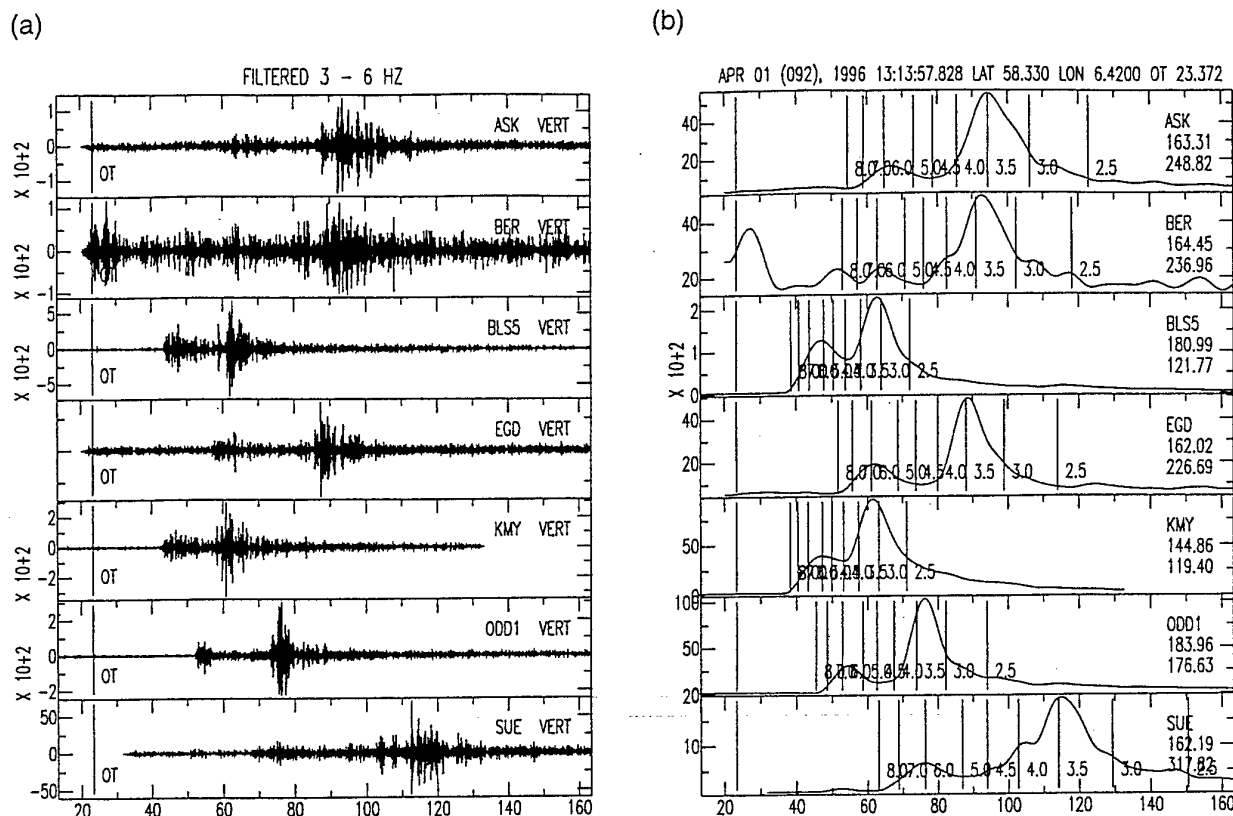
(a)

(b)

Figure 2.   (a) Record displays for an explosion in the Titania quarry in southern Norway recorded by the Norwegian Seismograph Network stations. A 3 to 6 Hz band-pass filter is used to enhance SNR. (b) Envelope transforms after smoothing of the records in (a), including group velocity markers (in km/sec) tied to the focal parameters displayed at the top of the figure. Epicenter azimuth and distance are listed below the station codes.

alyst (that is *Pg* and *Pn* arrival times) are also shown in Figure 4. Our envelope locations are occasionally even closer to the true ones than those appearing in the local bulletins. The envelope epicenters are based on NSN station records only while the bulletin solutions incorporate data from arrays to the east. This should give relatively better east–west resolution in the bulletin solutions, but this is not fully realized in practice due to inadequate travel-time tables. In Table 1, we give statistics of the location errors for both bulletin and envelope epicenter estimates.

Fennoscandian Array Records

Records from array center sensors of the arrays that have been offered for the International Monitoring System (Anonymous, 1996) are displayed in Figure 5 for an earthquake north of Bothnian Bay (Fig. 1). Again, predicted *PG* and *LG* arrival times coincide well with respective record peaks, although *PG* is weak beyond 400 km. As noted above, for location purposes, we may replace *PG* with *Pn*. Since we pick arrival times tied to wavelet peaks, the SNR

differences between an array beam trace and a single sensor envelope is moderate.

Envelope Analysis of Other Network Recordings

Since *Pg, Pn, Lg,* and *Sn* are globally observed crustal phases, we intuitively expect that envelope processing and subsequent epicenter determinations as described earlier are transportable to any seismic network area. The validity of this hypothesis has been tested on network recordings from Israel (Shapira *et al.,* 1996; Shoubik *et al.,* 1996), Italy and Germany (Ryzihkov *et al.,* 1996), and also New England (ourselves). The outcome of all these studies were similar to those obtained here, namely, that envelope records are dominated by *PG* and in particular *LG* phases having linear travel-time curves with velocities of approximately 6.1 and 3.5 km/sec, respectively. In the extreme, original waveform records were too complex for reading more than onset time of first-arriving *P* phase, while after envelope transformation, both *PG* and *LG* were easily pickable. In other words, envelope processing is clearly a viable alternative to conventional analysis of waveform recordings.
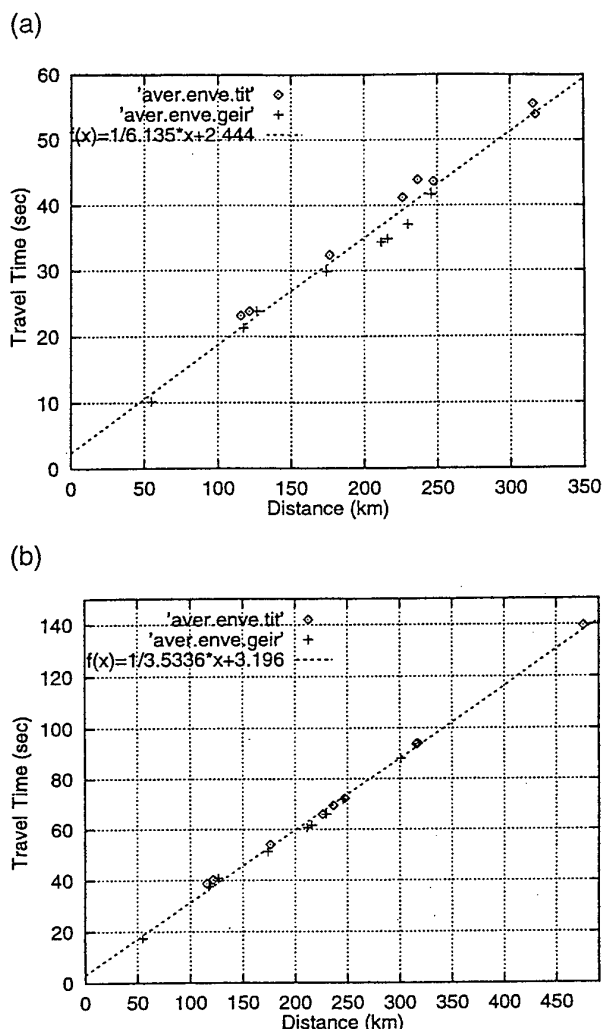
4

(a)

(b)

Figure 3.   *PG* and *LG* peak amplitude travel times as a function of distance. These curves were obtained from observed *PG* and *LG* arrival times for Titania and Geiranger explosions. Since site coordinates are exactly known, accurate origin times were calculated from *Pg* arrival times (for distances less than 100 km) with a presumed *Pg*-phase velocity of 6.1 km/sec. There are some scatters in the observations (system timing errors?), but the fitted straight lines have reasonable slopes. For even better fit to given travel-time curves, station corrections should be introduced.

Discussion and Conclusion

In this study, we have demonstrated that simple envelope processing is well suited for analysis of complex, local network recordings. The outstanding feature is the ease by which a substitute for the *Lg* phase can be picked. This phase is problematic in conventional analysis schemes whether working with single-component, three-component, or array records. The envelope records give excellent SNRs; picking arrival times at maximum wavelet amplitude means that meaningful signal attributes can be extracted from single-station records that otherwise may require array recordings. Envelope records from a seismograph network can be used for real-time monitoring purposes in much the same way as arrays (Ryzhikov *et al.*, 1996; Shapira *et al.*, 1996; Shoubik *et al.*, 1996). Magnitude determinations are easily performed from maximum amplitudes of *PG* and *LG* wavelets, as demonstrated by Mendi and Husebye (1994, 1995). Furthermore, envelope transform operations can easily be performed in the field, thus reducing transmission loads significantly in view of envelope sampling rates of 1 to 2 Hz compared to 40 to 100 Hz for waveforms.

Critical for accurate locations of local events is use of proper travel-time curves. In Fennoscandia, crustal thicknesses vary from 20 km (offshore Norway) to about 50 km in central Finland (Kinck *et al.*, 1993). All the seimological centers in the region use travel-time curves calculated from two- and three-layer 1D models with crustal thicknesses varying from 30 to 45 km. This may explain why gross location errors occasionally occur—in particular, in combination with poor network configuration like for events occurring outside the network. As discussed earlier, travel-time curves for *PG* and *LG* are much more easily established in comparison to those of the conventional crustal phases. To our surprise, occasionally, some gross mislocations were due to timing errors at one or more NSN stations despite on-line access to the GPS (satelite) clock. The reason for this appears to be the software used for calibrating the internal clock versus the GPS clock—apparently not an uncommon problem in local network operations.

What are the potential drawbacks with envelope processing? It is not foolproof; *PG* may be larger than *LG* (especially at distances less than 100 km), while *Lg* blockage is common for offshore events (Mendi *et al.*, 1997). These kinds of exceptional wave-propagation features would also cause problems in conventional analysis, emphasizing the need for analyst screening of automated bulletin results. Focal depths cannot be estimated from envelope wavelet attributes since these parameters are not particularly sensitive to source depth. Perhaps the most severe objection to envelope processing came from a colleague claiming that it "takes the fun out of seismology."

Envelopes of different events stemming from the same explosion site appear to be identical in form, implying that for such recordings there should be no need to undertake any form of phase reading. We are now testing a neural network scheme aimed at teaching the computer to recognize site-specific explosion recordings (Fedorenko *et al.*, 1997), thus attempting to mimic seismogram interpretation skills of a trained analyst (Israelsson, 1990; Riviere-Barbier and Grant, 1993).
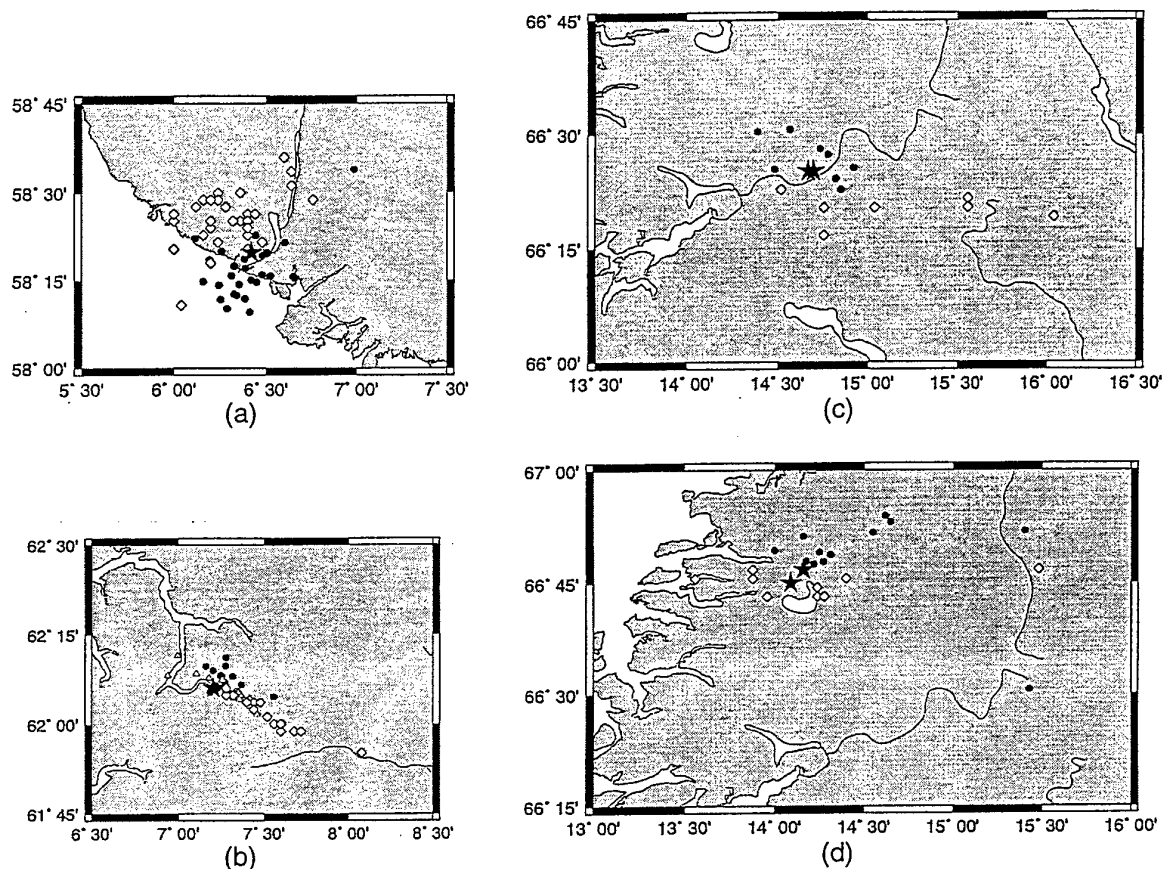
Figure 4.   (a) Envelope location experiment using Titania mining explosions, Southern Norway. *PG* and *LG* peak amplitude arrival times were read automatically from segmented detector output files, and epicenter coordinates were obtained by a grid-search procedure (Ruud *et al.,* 1993). Star is the mine site, diamonds, the envelope locations, and dots, the analyst-derived bulletin solutions. Almost all locations are within 10 km of the mining site. (b) Location of Geiranger quay construction explosions. Symbols as for (a). Station MOL (distance 55 km) is critical for accurate locations here, but only occasionally could PG arrival times be obtained due to *LG* interference. Also shown (white triangles) are new epicenter locations obtained by replacing *PG* times with corresponding *Pg* and *Pn* arrival times as read by analyst. (c) Rana mining explosions (two sites) used for preliminary envelope location experiments. Symbols as for (a)—same travel-time curves as for Titania. Since the network stations are deployed in the N–S direction (the "width" of Norway at this point is only 5 km), the E–W location is not well constrained. Bulletin solutions often incorporated readings from one or more arrays to the east, giving better E–W resolution. (d) Svartisen dam excavation explosion used in envelope location experiments. Symbols as for (a). Note the excellent latitude estimates obtained by the envelope locations (diamonds).

Table 1

Summary of location results for the four sites. Latitudes and longitudes are average results from a number of events. Standard deviations are computed relative to the average locations of the same events. Median location errors are computed relative to the known locations of the sites. Largest deviations are found for the N. Norway explosions Rana and Svartisen; the bulletin epicenter solutions benefit from access to phase readings from the arrays to the east.

Site Method	Latitude (deg. N)	Std. Dev. lat. (deg)	Longitude (deg. E)	Std. Dev. long. (deg)	Median Loc. Err. (km)	No. of Events
Titania	58.33		6.43			
Bergen bull.	58.27	0.10	6.41	0.18	11	29
Enve. $P + S$	58.43	0.08	6.31	0.20	17	29
Man. P + Enve. S	58.26	0.06	6.40	0.15	9	29
Geiranger	62.10		7.21			
Bergen, bull.	62.12	0.03	7.29	0.11	6	18
Enve. $P + S$	62.03	0.05	7.51	0.20	12	18
Man. P + Enve. S	62.09	0.04	7.29	0.14	8	20
Rana	66.42		14.69			
Bergen bull.	66.45	0.05	14.70	0.19	11	8
Enve. $P + S$	66.33	0.04	15.12	0.53	15	8
Man. P + Enve. S	66.39	0.06	14.99	0.20	13	16
Svartisen	66.77		14.13			
Bergen bull.	66.81	0.10	14.50	0.47	8	12
Enve. $P + S$	66.75	0.02	14.56	0.92	8	12
Man. P Enve. S	66.72	0.34	14.58	0.72	15	19
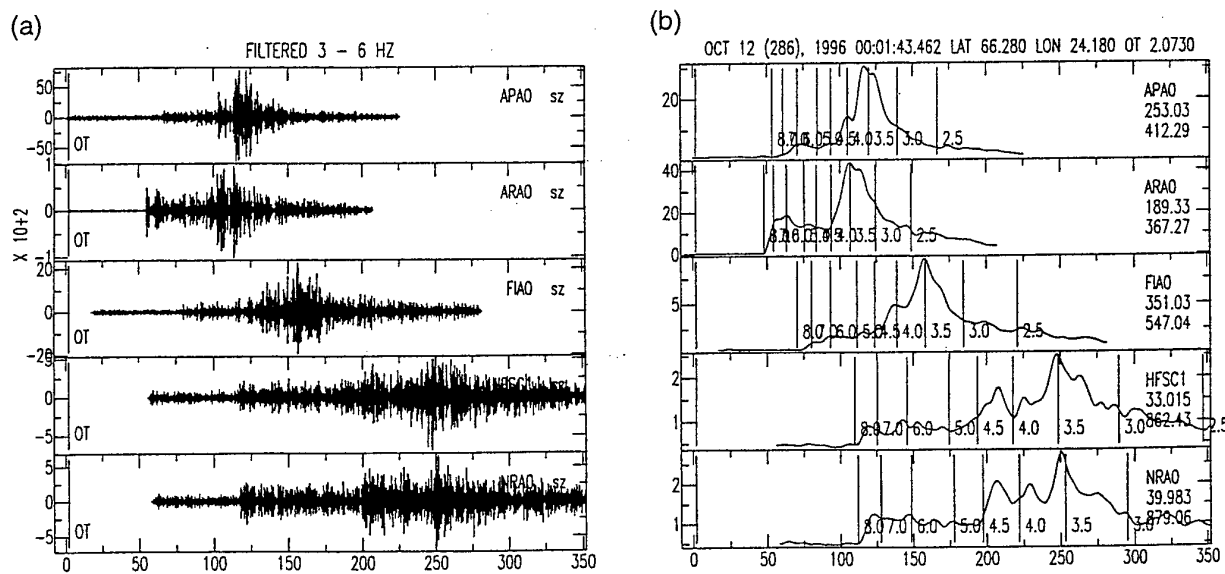
Figure 5. (a) Record displays for a local earthquake in Bothnian Bay, Finland, and recorded by the center seismometer for several array stations (Fig. 1). A 3 to 6 Hz bandpass filter was used. (b) The envelope transforms of the waveforms in (a) after smoothing, otherwise as for Figure 2b. Note the dominance of LG and that PG is reasonably prominent out to about 500 km. An alternative if PG is unclear is to read the first-arriving P wave (Pn). Our envelope epicenter solution coincided with that in the bulletin and shown in Figure 1. Phase readings from one or more of these arrays are used frequently in the Bergen bulletin epicenter solution; corresponding observations for the other events in this study were not available for our envelope locations.

Acknowledgments

References

Anonymous (1996). UN General Assembly: Comprehensive Nuclear Test Ban Treaty, Treaty Text and Annexes, http://www.cdidc.org:65120/librarybox/lib_top.html

Fedorenko, Y. V., E. S. Husebye, B. Heincke, and B. O. Ruud (1997). Recognizing explosion sites without seismogram readings: neural network analysis of envelope transformed multistation SP recordings in the 3–6 Hz band, in preparation.

Hansen, R. A., F. Ringdal, and P. G. Richards (1990). The stability of the RMS Lg measurements and their potential for accurate estimation of the yields of Soviet underground nuclear explosions, *Bull. Seism. Soc. Am.* **80**, 2106–2126.

Hestholm, S. O., E. S. Husebye, and B. O. Ruud (1994). Seismic wave propagation in complex crust-upper mantle media using 2D finite difference synthetics, *Geophys. J. Int.* **118**, 643–670.

Israelsson, H. (1990). Correlation of waveforms from closely spaced regional events, *Bull. Seism. Soc. Am.* **80**, 2177–2193.

Kinck, J. J., E. S. Husebye, and F. R. Larsson (1993). The Moho depth distribution in Fennoscandia and the regional tectonic evolution from Archean to Permian times, *Precambrian Res.* **64**, 23–51.

Kværna, T. and F. Ringdal (1995). Generalized beamforming, phase association and threshold monitoring using a global seismic network, in *Monitoring a Comprehensive Test Ban Treaty*, E. S. Husebye and A. M. Dainty (Editors), Kluwer Academic Publishers, Dordrecht, The Netherlands, 447–466.

Mendi, C. D. and E. S. Husebye (1994). Near real time estimation of magnitudes and moments for local seismic events, *Ann. Geofis.* **37**, 365–382.

Mendi, C. D. and E. S. Husebye (1995). Near real time estimation of seismic event magnitude and moment via P and Lg phases, in *Earthquakes Induced by Underground Nuclear Explosions*, R. Console and A. Nikolaev (Editors), Springer Verlag, Berlin, 281–300.

Mendi, C. D., B. O. Ruud, and E. S. Husebye (1997). The North Sea Lg-blockage puzzle, *Geophys. J. Int.* **130**, in press.

Mykkeltveit, S. and E. S. Husebye (1981). Lg wave propagation in Eurasia, in *Identification of Seismic Sources—Earthquake or Underground Explosion*, E. S. Husebye and S. Mykkeltveit (Editors), D. Reidel Publishing Company, Dordrecht, The Netherlands, 421–451.

Nuttli, O. W. (1973). Seismic wave attenuation and magnitude relations for eastern North America, *J. Geophys. Res.* **78**, 876–885.

Ringdal, F., E. S. Husebye, and A. Dahle (1975). *P*-wave envelope representation in event detection using array data, in *Exploitation of Seismograph Networks*, K. G. Beauchamp (Editor), Noordhoff Publ. Co., Leiden, The Netherlands, 353–372.

Riviere-Barbier, F. and L. T. Grant (1993). Identification and location of closely spaced mining events, *Bull. Seism. Soc. Am.* **80**, 1527–1546.

Ruud, B. O. and E. S. Husebye (1992). A new three-component detector and automatic single station bulletin production, *Bull. Seism. Soc. Am.* **82**, 221–237.

Ruud, B. O., C. D. Lindholm, and E. S. Husebye (1993). An exercise in automating seismic record analysis and network bulletin production, *Bull. Seism. Soc. Am.* **83**, 660–679.

Ryzhikov, G. A., M. S. Biryulina, and E. S. Husebye (1996). A novel approach to Automatic Monitoring of Regional Seismic Events, *IRIS Newslett.* **15**, 12–14.

Sereno, T. J. and S. R. Bratt (1989). Seismic detection capability at NORESS and implications for the detection threshold of a hypothetical network in the Soviet Union, *J. Geophys. Res.* **94**, 10397–10414.

Shapira, A., Y. Gitterman, and V. L. Pinsky (1996). Discrimination of seismic sources using the Israel Seismic Network, in *Proc. of the 18th Annual Seismic Research Symposium on Monitoring a CTBT*, James F. Lewkowicz, Jeanne M. McPhetres, and Delaine T. Reiter (Editors), PL-TR-96-2153, Phillips Laboratory, Hanscom AFB, Massachusetts, 612–621.

Shearer, P. M. (1997). Improving local earthquake locations using the L1 norm and waveform cross correlation: application to the Whittier Narrows, California, aftershock sequence, *J. Geophys. Res.* **102**, 8269–8284.

Shoubik, B. M., A. F. Kushnir, L. M. Haikin, and A. M. Dainty (1996). SCANLOC: Automatic seismic event location based on local seismic network data, in *Proc. of the 18th Annual Seismic Research Symposium on Monitoring a CTBT*, James F. Lewkowicz, Jeanne M. McPhetres, and Delaine T. Reiter (Editors), PL-TR-96-2153, Phillips Laboratory, Hanscom AFB, Massachusetts, 774–781.

Tarvainen, M., T. Tiira, and E. S. Husebye (1997). Locating near field seismic events with global optimization based on Interval Arithmetic method, submitted for publication.

Institute of Solid Earth Physics
University of Bergen
Allégt. 41
N-5007 Bergen, Norway
  (E.S.H., B.O.R.)

Earth Science Division
Phillips Laboratory
29 Randolph Rd.
Hanscom AFB, Massachusetts 01731-3010
  (A.M.D.)

Appendix 3

Comments on "The Political Sensitivity of Earthquake Locations by van der Vink and Wallace"

M. Henger and K. Koch, Federal Institute for Geosciences and Natural Resources, Germany

B. O. Ruud and E. S. Husebye, University of Bergen, Norway

In the Fall 1996 IRIS Newsletter, van der Vink and Wallace (1996) use as one of their examples a small seismic event (magnitude 2.4) on 13 January 1996 near the former USSR test site on Novaya Zemlya. Other seismologists who were requested to evaluate this event obtained a different epicenter location from that of van der Vink and Wallace although they used the same data, namely that from the ARCESS (ARA0) and Spitsbergen (SPA0) arrays. Data from the three-component Norilsk (NRI) station in Siberia indicates that the location determined by van der Vink and Wallace is incorrect and supports the other determinations (Figure 1).

Data Analysis

We extracted relevant time segments of recordings from the Norilsk three-component station. At ARA0 and SPA0 the noise conditions are dominated by strong, low-frequency microseisms up to 2 Hz, so the optimum signal-to-noise ratios (SNRs) are in the 2 - 10 Hz band. At NRI the local noise conditions are very different with much less noise at the low frequencies. The S-wave is visible even at very low frequencies and there is a clear wavelet near the expected P arrival time with a dominant frequency of 1.5 Hz (Figure 2a & b).

The methods for analyzing array-recorded signals are well established and in cases with good SNRs even simple bandpass filtering and subsequent stacking suffice to accurately pick Pn and Sn arrival times. For the 13 January event, this was not the case, due to interference in the SPA0 records with signals from an earthquake on the mid-oceanic ridge west of Spitsbergen (Ringdal, 1996). Van der Vink and
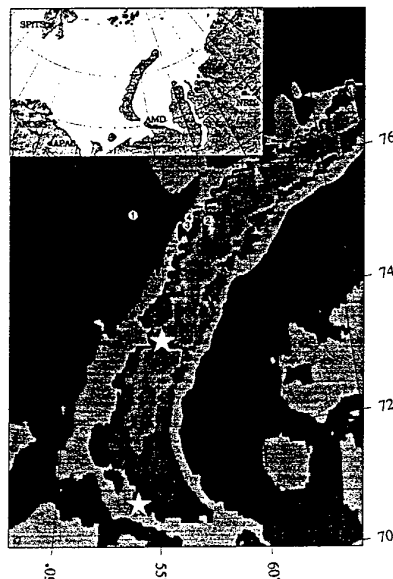

Figure 1. Various epicenter determinations for the 13 January 1996 event at/near Novaya Zemlya: (1) two-array location (SPA0 & ARA0) using IASPEI tables, (2) as for (1) but using Bergen University tables, (3) two arrays and the NRI station using IASPEI tables, and (4) same as (3) but using Bergen University tables. Note, Ringdal's (1996) two-array location at 75.38°N, 56.7°E is close to our epicenter (4). That of van der Vink and Wallace (1996) would coincide with (1) if we add 5 sec to their Sn-reading. The Novaya Zemlya test sites are marked by stars. The map insert shows the seismic arrays and 3C stations in the vicinity of Novalya Zemlya. Records from APA0 (Apatity) and the new AMD (Amderma) array were not available to us. To our understanding the APA0 array did not detect this event.

Wallace, being unaware of this, picked a too early Sn arrival at SPA0, which resulted in a shorter epicenter distance and hence 'moved' the epicenter well into the Barents Sea.

Apart from the misinterpretation of the Sn arrival due to the interfering

event, another aspect contributed to the move of the epicenter westward. The differential epicenter angle between SPA0 and ARA0 is only about 45 deg, so the epicenter location resolution is relatively poor in the east/west direction as it depends strongly on the traveltime model used. However, the accuracy improves considerably if relevant Pn and Sn arrival times can be extracted from the NRI records. An additional advantage here is that with three station observations the choice of traveltime table used for location is less critical (Kennett, 1996) if the azimuth coverage is reasonable.

Envelope processing (Husebye et al., 1998) proved successful, as demonstrated in Figure 2c. The top trace is the envelope for the 1.0 - 2.5 Hz passband and a prominent, presumably P-wave arrives at 113 sec. It was also seen in the original records. However, extensive 3C analysis gave an azimuth of about 260 degrees which is far off the 310 degrees expected for Novaya Zemlya and polarization characteristics were non-P. The corresponding waveform has some semblance to a local Rg-wave - no sharp onset and monochromatic pulses. In Figure 2c we also display the 3C envelope for the 2 - 5 Hz passband; a presumed weak P-arrival at 122 sec (SNR ~ 1.3) and a clear, presumed Sn-arrival at 243 sec (SNR ~ 1.5). A SNR of 1.5 is taken to indicate a significant signal in the 3C envelope since this process is similar to incoherent beamforming with a rather long STA window (a threshold of 1.6 is used for NORSAR incoherent beams). As an additional check, we used the Pisarenko et al. (1987) phase-picking algorithm, whose picks coincide with
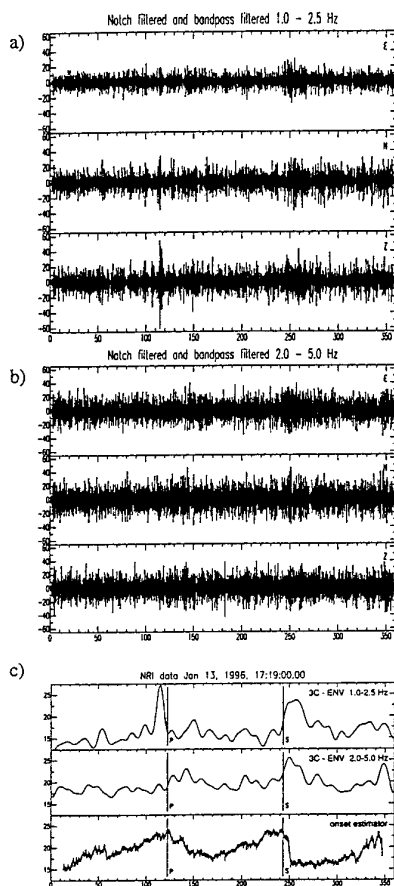
Figure 2. The 3-component NRI (Norilsk, Siberia) records for the 13 Jan 1996 event. The upper and middle parts) show filtered records in the 1.0 - 2.5 Hz and 2.0 - 5.0 Hz passbands respectively. Notch filters were used in addition to bandpass for removing spectral spikes. In c) the two upper traces are 3 C envelopes (Husebye et al. 1998) Pn-and Sn-arrival times as picked for this event are marked.

the envelope records (Figure 2c). Using the derived NRI Pn and Sn arrival times, we obtained an epicenter location of 75.38° N, 56.55° E, using the Bergen University traveltime curves (Figure 1). The residuals using the Bergen University traveltime curves are not unreasonably large (less than 1.6 sec), while for the IASPEI model the residuals varied +/- 5.6 sec, although the corresponding epicenter difference was less than 15 km. Note, the weak Pn-

arrival in the records are not critical for the epicenter determination; we have also located the event using a Pn arrival at 113 sec (see Figure 2c) and also without the P-arrival of NRI. In the first case the epicenter moved 10 km and in the second case only 2 km (in both cases the local traveltime tables were used).

Discussion and Conclusion

Reexamining the van der Vink and Wallace (1996) location, we found that their small misreading of the Sn-arrival time was not as critical as their use of the IASPEI tables. Non-Scandinavian scientists appear to consider the IASPEI tables to be adequate for signals recorded from Novalya Zemlya at stations in Fennoscandia, but the "local" scientists use somewhat different tables, which are more accurate for this region.

What can be said about the source of this much debated event of 13 January 1996? Its mb magnitude of only 2.4, which is equivalent to a yield not exceeding 100 tons TNT. Such small charges are typical of many chemical explosions and, even if it were nuclear in origin, it could hardly be termed a nuclear device in a CTBT context, as argued by van der Vink and Wallace. A criterion in favor of an earthquake source is the relatively small P/S-signal ratio (van der Vink and Wallace, 1996). We are not convinced that such a criterion can be used here without extensive modification, because the Barents Sea sedimentary basin blocks Lg-propagation, in other words, Lg-waves leak as S-waves into the upper mantle and reappear in the Sn coda (Mendi et al. 1997). Observationally, this is manifested in an extended Sn-wave train, as seen in Novaya Zemlya recordings.

Using the novel envelope analysis technique we could extract useful traveltime information from the Norilsk 3C station, despite the poor quality of the NRI records for an event of magnitude 2.4 at an epicenter distance of about 1200 km. However, we confess

that such low magnitude events can neither be accurately located nor clearly identified with seismological means only. In particular, the IASPEI travel time tables are not well suited for accurate event locations in the Novaya Zemlya area for regional epicenter distances. Clearly, certain event location areas remain politically sensitive, as this event has demonstrated.

REFERENCES

Husebye, E.S., B.O. Ruud A.M. Dainty (1998): Fast, robust and reliable epicenter determinations; Envelope processing of local network data, Bull. Seism. Soc. Am, Feb 1998

Kennett, B.L.N. (1996): Event location and source characterization, in: Monitoring a Comprehensive Test Ban Treaty, E.S. Husebye and A.M. Dainty (Editors), Kluwer Academic Publishers, Dordrecht, The Netherlands, 501 - 520.

Mendi, C.D., B.O. Ruud, E.S. Husebye (1997): The North Sea Lg-blockage puzzle, Geophys. J. Int., 130, 669 - 680.

Pisarenko, V.F., A.F. Kushnir and I.V. Savin (1987): Statistical adaptive algorithms for estimation of onset moments of seismic phases, Phys. Earth Planet. Int., 47, 4 - 10.

Ringdal, F. (1996): Study of low-magnitude seismic events near the Novaya Zemlya nuclear test site, Semiannual Technical Summary, 1 April - 30 September 1996, NORSAR Sci. Rep. No. 1 1996/97, Kjeller, Norway.

van der Vink, G.E. and T. Wallace (1996): The political sensitivity of earthquake locations, IRIS Newsletter, Vol XV, No 3, 20-23.

Response from van der Vink and Wallace

Gregory van der Vink, IRIS, and Terry Wallace, University of Arizona

We agree. Henger et al. provide a more accurate location for the epicenter of the 13 January event in Novaya Zemlya — one of the examples presented in our article. We based our location on the data from the ARCESS (ARA0) and Spitsbergen (SPA0) arrays, and were unaware that signals from Norilsk (NRI) indicated a contemporaneous earthquake on the mid-ocean ridge west of Spitsbergen.

The conclusions of our article, however, are in no way altered by the refinement of the epicenter location. As we have repeatedly seen, earthquakes that occur in sensitive areas during politically sensitive times are vulnerable to misinterpretation. Independent of which location is used (all of the epicenter determinations for the 13 January 1996 event are more than 200 kilometers from the Russian test site), the earthquake raised concern over Russian compliance with the ban on nuclear testing. Given the lowering of detection thresholds and the continuation of subcritical experiments, it is not surprising that such coincidences occur. And in fact, since the writing of our article, such a coincidence has occurred again. (see news articles inset and the bannergram of this Newsletter).

To help prevent such false alarms in the future, data from all available stations needs to be examined. Henger et al.'s extraction of critical travel-time information for a magnitude 2.4 event from a single 3-component station at a distance of 1200 km is an enlightening example for those who may still debate the importance of auxiliary stations for the monitoring of the CTBT. For the more recent 16 August 1997 false alarm, critical data came from the IRIS GSN station KEV, which is not even part of the official CTBT monitoring system.

We disagree with Henger at al in their assertion that a magnitude 2.4 event, which is equivalent to a yield not exceeding 100 tons of TNT, "could hardly be termed a nuclear device in a CTBT context". From the United States' perspective, it most certainly would. On August 11, 1996 President Clinton rejected proposals for continued sub-kiloton tests, and announced his decision to pursue a "true zero-yield comprehensive test ban." He based such a decision in recognition that the act of nuclear testing, not the threshold of such tests, is objectionable within the non-proliferation regime.

Both the United States and Russia are conducting hydrodynamic experiments at their test sites. Whether these experiments must remain sub-critical, or whether they can produce modest yields is unclear from the negotiations. Because nuclear materials such as plutonium are used in the experiments, they are conducted in a manner similar to nuclear tests. Although there is currently no precise agreed upon technical definition of the maximum explosive energy from hydrodynamic experiments, a seismic signal corresponding to 100 tons of tamped explosive would be assumed as a violation of the ban on nuclear testing by the United States.

Areas such as Novaya Zemlya, that are generally considered aseismic at teleseismic magnitude levels, will appear seismic at the lower magnitude levels detectable from regional coverage. Regional networks now provide a detection capability for the Novaya Zemlya area that is near mb 2.5 (NORSAR, 1996). Accordingly, we can expect to find events of concern every few years, such as 16 August 1997, 13 January 1996, 13 January 1995, and 31 December 1992. Open networks in the western United States, where the seismicity is greater and the coverage more extensive, provide a detection threshold below magnitude 2.2 for the US nuclear test site (Hennet et al. 1996). In fact, six days before the US' second 1997 subcritical experiment, a seismic event was recorded on the Nevada Test Site.

References

Hennet, C.B., G.E. van der Vink, P.G. Richards, V.V. Adushkin, Y.F. Kopnichev, and R. Greary, EOS, vol.77, no.31, July 30, 1996, p.289, 300, 301.

NORSAR semi-annual technical report, November 1996.

January 1996

U.S. officials suspect Russia staged nuclear test this year

Blast would violate moratorium imposed in '92

August 1997

Russia suspected of nuclear testing

Moscow says blast was an earthquake

Appendix 4

The North Sea *Lg*-blockage puzzle

C. Deniz Mendi, Bent O. Ruud and Eystein S. Husebye

University of Bergen, Institute of Solid Earth Physics, Allégt. 41, N-5007, Bergen, Norway

SUMMARY

The North Sea *Lg* blockage for wave paths across crustal graben structures is a well-established observational fact. Analysis of such observations implies that *Lg* blockage takes place in graben areas associated with sedimentary basin formation and crustal thinning. These intriguing observations have triggered many theoretical studies aimed at highlighting specific *Lg* loss mechanisms, albeit so far with only moderate success. Our approach to this problem is to simulate seismic wavefield propagation through the crustal waveguide using 2-D finite-difference techniques. The graben structures are known in detail from oil exploration works in the North Sea, which has enabled us to use realistic crustal models in our *Lg* synthetics. In the most extreme model tested, the crystalline crust thickness beneath the graben amounted to only 5 km, while the overlying sedimentary pile is nearly 10 km thick. At the base of the crust in the graben area the Moho is elevated nearly 10 km. This model has similarities to the oceanic crustal waveguide, where total *Lg* blockage is claimed for path lengths exceeding 100 km. The synthetic wavefields are displayed in terms of snapshots, semblance velocity analysis and time–space rms amplitudes. The dominant structural *Lg* loss mechanisms are the delay of the *Lg* waves in the thick sediments, *Lg*-to-*Rg* conversions (scattering) by lateral heterogeneities in the sediments, and *S*-wave leakage out of the crustal waveguide and into the upper mantle. A fraction of these upper-mantle *S* waves return to the crust and appear as *Sn* coda. Observationally, strong *Sn* phases of long duration are often associated with weak *Lg* phases and vice versa. Our synthetics produced *Lg* amplitude decay amounting at most to 6–10 dB, while observational data imply blockage amounting to 15–20 dB. The latter is equivalent to a *Pn*–*Lg* magnitude difference of nearly one magnitude unit. The main outcome of this study is therefore that *Lg*-wave propagation is very robust and that a dominant blockage effect associated with intrinsic attenuation, that is Q values of the order of 100 at 2 Hz for a path length of minimum 100 km, is necessary to conform to observations.

Key words: attenuation, finite-difference methods, *Lg* blockage, North Sea grabens, scattering, synthetic seismograms.

INTRODUCTION

An outstanding puzzle in observational seismology is that of *Lg*-wave blockage, which initially was reported for mixed ocean–continental paths (Press & Ewing 1952; Båth 1954). More recently, *Lg* blockage has been reported for intercontinental wave paths, particularly across structural boundaries such as grabens, mountains and sedimentary basin areas (Gregersen 1984; Baumgardt 1990). In view of the importance of *Lg* observations for event magnitude and yield estimation, and also as a potential discriminant, many *Lg* studies have been published recently (Israelsson 1994; Zhang *et al.* 1994; Xie & Lay 1995).

In view of the observational data at hand, many hypotheses or combinations thereof have been suggested to account for *Lg* blockage, namely crustal thickness variations, surface topography, geometry and thicknesses of sedimentary basins, mode conversions/leakage of *Lg* energy downwards into the mantle, *Lg*-to-*Rg* trapping in overlying sediments and naturally strong anelastic attenuation. In a recent study, Zhang *et al.* (1994) used a multivariate analysis approach in an attempt to quantify which of the above structural features is dominant for *Lg* blockage. Results were that waveguide geometry (abrupt crustal thickness variation) and anelastic attenuation were most important in this regard. Gregersen & Vaccari (1993) reached similar conclusions for *Lg*-blockage observations across the North Sea Viking Graben, and also pointed to the spreading of *S*-wave energy over a longer duration due to interaction with the overlying low-velocity sediments. Cao & Muirhead (1993) found

from finite-difference simulations that efficient *Lg* blockage occurred for models with a water depth of 2000 m. Their result does not apply to the North Sea grabens, since the water depth here (average *ca.* 100 m) is only a small fraction of the dominant wavelength.

The anomalous *Lg*-blockage observations have triggered many studies to explain this phenomenon in a theoretical manner. For example, Kennett (1986) used a ray diagram approach to explain qualitatively *Lg* blockage, while Bouchon (1981) used a discrete wavenumber representation for studying wave propagation in multi-layered media. Other scientists have studied *Lg* blockage effects across the Alpine Range and the Pyrenées (e.g. Chazalon *et al.* 1993; Campillo *et al.* 1993). Maupin (1989) used a coupled-mode approach for simulating North Sea *Lg* blockage, and Gregersen *et al.* (1988) and Gregersen & Vaccari (1993) used a similar approach for analysing *Lg* blockage in the same area. In recent years, finite-difference and finite-element methods have become popular in computing realistic wavefield responses as a tool for explaining *Lg*-blockage mechanisms, and we refer here to Regan & Harkrider (1989), Cao & Muirhead (1993) and Xie & Lay (1994). The feature in common for all the theoretical studies mentioned is the inability to explain fully the *Lg* blockage as observed across grabens in the North Sea and in other areas using realistic crustal models. The only way to obtain sufficiently strong blockage seems to be to introduce strong anelastic attenuation, since deformation of the crustal waveguides is unable to do this. As mentioned, for mixed continental–oceanic wave paths where the length of the latter is 100 km or more, *Lg* blockage is almost complete. Recently, Zhang & Lay (1995), using a normal-mode *Lg* representation, claimed that the overall thickness of the oceanic crustal waveguide is too thin to allow *Lg* to develop as a significant phase in the frequency band 0.3–2.0 Hz, thus explaining oceanic *Lg* blockage.

A general drawback with most of the theoretical approaches mentioned above is that the crustal models used are lacking many details on Moho undulation and sedimentary basins along the *Lg* propagation paths. Naturally, finite-difference modelling can easily incorporate such structural features and thereby provide better insight into *Lg* loss mechanisms. There have already been some efforts along these lines, such as the work of Cao & Muirhead (1993), Xie & Lay (1994) and Regan & Harkrider (1989) demonstrating in a convincing manner the complexity of *Lg* propagation even for slowly varying crustal models. In this paper, we simulate *Lg* blockage across the Central Graben through 2-D finite-difference (FD) synthesis, since *Lg* observations are readily available (Gregersen 1984; Kennett & Mykkeltveit, 1984; Kennett *et al.* 1985) and because the graben structure is mapped in considerable detail (Barton & Wood 1984; Gabrielsen *et al.* 1990).

OBSERVATIONAL DATA

The *Lg* blockage here is well documented in the literature, in particular in the works of Gregersen (1984), Kennett & Mykkeltveit (1984) and Kennett *et al.* (1985). The most pronounced blockage takes place for *Lg* paths with source locations to the west of the graben and landward recordings in SW Norway. To illustrate the North Sea *Lg* blockage, a few events have been chosen (source and receiver geometries
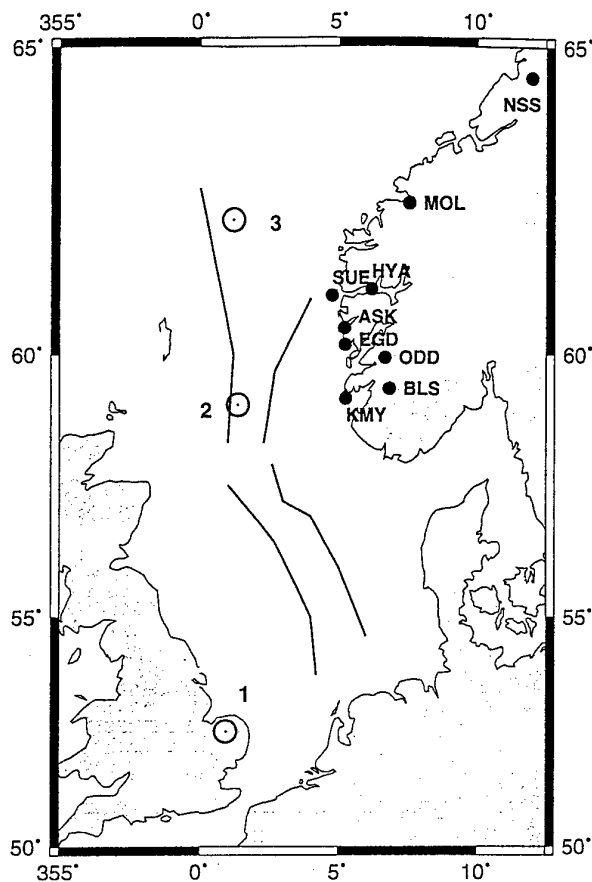

Figure 1. The two dominant North Sea graben segments are outlined; Central Graben to the South and the Viking Graben to the North. The seismograms displayed in Figs 2–4 are recordings from the earthquake locations marked by open circles. Station locations are marked with filled circles on the map.

in Fig. 1), and the seismograms displayed in Figs 2–4. The graben blockage effects are obvious; outstanding features are a relatively strong *Sn* phase and a nearly extinct *Lg* phase. The expected *Lg* arrivals are literally hidden in the *Sn* coda or tail in most of the seismograms.

MODEL BUILDING STRATEGY

The amplitude patterns are not always consistent, as small source–receiver path changes could exhibit large differences in *Lg* propagation efficiencies (Mykkeltveit & Husebye, 1981). Such variations are also obvious from North Sea event recordings as displayed in Figs 2–4. This observational variation in *Lg* blockage, part of which may relate to the source mechanism and focal depth, motivated a flexible modelling scheme as illustrated in Fig. 5. The idea here is that by subdividing the crust near the free surface and close to the Moho we can easily change the model types from the extreme of one layer over a half-space to others with thick unevenly distributed sediment strata, Moho ramps and associated crustal thinning. This approach allows great flexibility in model building; details are given in Table 1, which lists the set of graben models used in this study. Model 2 is the proper 'graben
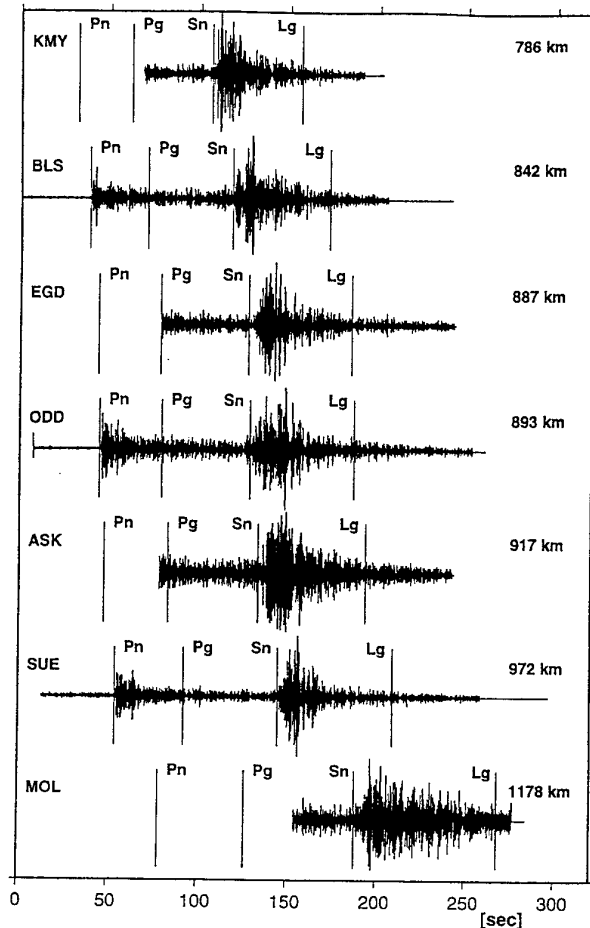
Figure 2. Seismic recordings from an earthquake in SE England (marked as 1 in Fig. 1) on 1994 February 15. The stations (see Fig. 1 for location) are operated in an automatic trigger mode, and the first-arriving *P* waves are occasionally lost. The expected arrival times of the *Pn*, *Pg*, *Sn* and *Lg* phases, calculated for the hypocentres and earth model used in the Norwegian Seismic Network Bulletin, are marked on each seismogram (for *Lg* a constant group velocity of 3.56 km s^{-1} is used). The traces have been bandpass filtered between 2 and 4 Hz. Outstanding features are strong *Sn* phases with long coda. The absence of the *Lg* phase is presumably caused by the North Sea graben block-age. The magnitude (M_L) of this event is reported as 4.0 by British Geological Survey. The *Pn* and *Lg* magnitudes for the displayed seismograms are estimated to be 3.9 and 2.7 respectively.

Figure 3. Seismic recordings from a central North Sea event on 1995 June 28 (marked as 2 in Fig. 1). Filtering and phase markings as for Fig. 2. Outstanding seismogram features for the first five stations (from EGD to HYA) are clear *Sn* phases of moderate duration followed by more prominent *Lg* phases. The far-away stations MOL and NSS are anomalous in this regard; strong *Sn* phases of long durations followed by relatively weak *Lg* wavetrains. The graben blockage appears modest for this earthquake, while some extra-ordinary structures between HYA and MOL/NSS cause *Lg* blockage at the latter two stations. M_L is reported as 3.2 by NORSAR. For the displayed seismograms, *Pn* and *Lg* magnitudes are estimated to be 3.0 and 3.1 except for the distant stations MOL and NSS which have *Lg* magnitudes of 2.4.

model', while Model 1 is a reference model with normal crust used for comparison (see also Fig. 10). Model 4 is exceptional as the crystalline crust thickness is reduced to about 5 km between the Moho bump and overlying graben sedimentary infill, and might thus be considered typical of oceanic crust. Model 3 is a reference model for Model 4. In Model 5 we have introduced random perturbations of velocities and density through von Karman functions (order 0.3) with rms velocity fluctuations of 8 per cent and correlation distances (horizontal and vertical) of 10 and 2.5 km (details in Hestholm *et al.* 1994) in the central part of the model (see Fig. 11). Apart from this, Model 5 is similar to Model 2. The 'prototype' model (Fig. 5) is based on a cross-section of the Viking Graben published by Gabrielsen *et al.* 1990.
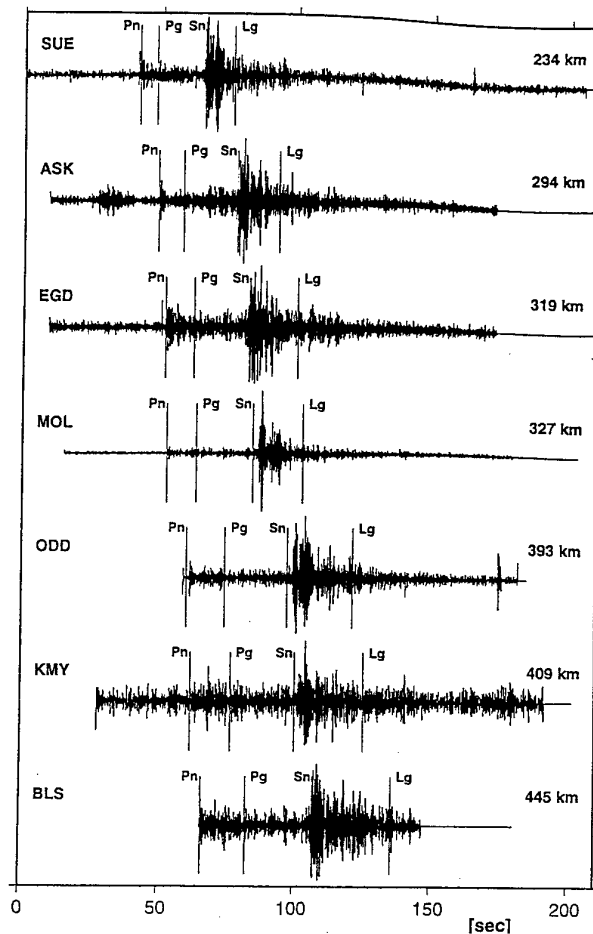
FINITE-DIFFERENCE SYNTHESIS

Our approach to 2-D FD modelling, including free-surface boundary conditions and source representation, is detailed in Hestholm *et al.* (1994). Absorbing boundary conditions were included in the form of 10 km thick damping layers along the side walls and bottom of the model. This technique effectively prevents artificial reflections from the model walls. Due to the absorbing boundaries, the useful distance range is 480 km (instead of the original 500 km shown in Fig. 5) and for this interval the vertical component of the wavefield is extracted at 1 km equidistant points along the top of the model. The source is located at a depth of 10 km and produces signal energy in the 0–5 Hz band with a peak frequency of 2.5 Hz. We have used a
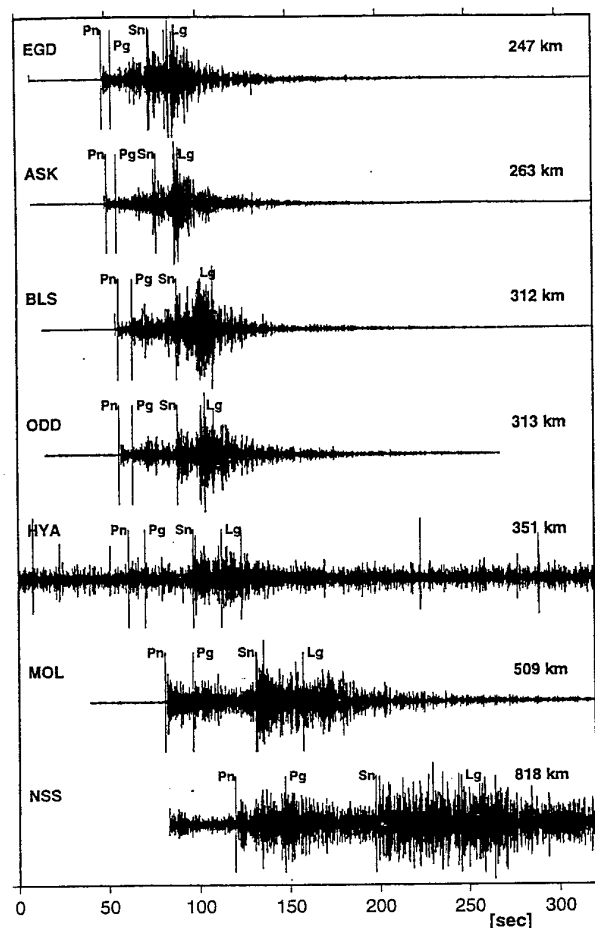
Figure 4. Seismic recordings from a northern North Sea earthquake on 1995 April 21 (marked as 3 in Fig. 1). Filtering and phase markings as for Fig. 2. Outstanding seismogram features are strong *Sn* phases of long duration followed by weak *Lg* phases. Apparently, the graben blockage causes *Lg* wave energy to leak as *S* waves into the upper mantle and subsequently reappear in the crust as part of the *Sn* coda. *Pn* and *Lg* magnitudes are measured to be 2.0 and 1.6, respectively.

rotation source that generates only *S* waves. However, *P* waves created by *P*-to-*S* conversions are also seen in the synthetics. A problem in many *Lg*-blockage studies is that of proper amplitude reference levels. Since the source is identical in all our synthetics, we can directly compare amplitudes for the various models. Since structural differences may give slightly different arrival times of the phases, the reference level could be slightly distorted. In practice, this is not much of a problem since the abundance of synthetic traces allows us to smooth the rms amplitudes over time and distance. In an analysis of real observations, the problem is more severe and an additional disadvantage is that potential reference phases such as *Pn, Sn* or even *Pg* themselves are distorted due to differences in source and/or propagation effects. The amplitudes of these phases depend on non-stationary parameters such as path, source type and focal depth and are thus not suited as reference levels. Our 2-D FD scheme for the synthetic wavefield calculation does not incorporate intrinsic attenuation (Q) and is in
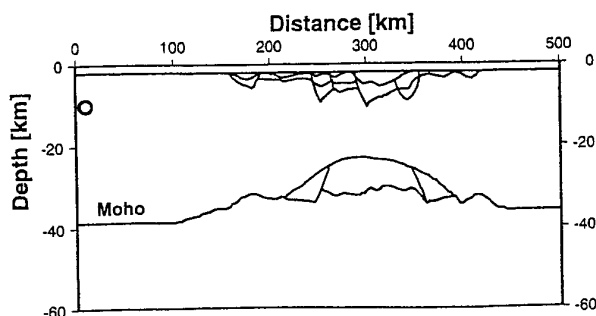

Figure 5. Prototype of northern North Sea graben model (Viking Graben). At the top there is a 2 km thick sediment layer extending over the entire length of the model. For the graben area (in the distance range 160–420 km) we have options for including the outlined sedimentary basins. Likewise, the blocks just above the Moho may be assigned either upper-mantle or crystalline-crust physical properties. Further details of the models actually used are given in Table 1. The source (open circle) is located 10 km from the left edge of the model and at a depth of 10 km. Note the different scaling of horizontal and vertical axes in this plot. In FD computations the model was extended downwards to a depth of 80 km.

this respect similar to many other blockage studies reported in the literature. However, intrinsic attenuation can be estimated in a manner similar to that used in *Lg* magnitude studies and will be discussed in a later section.

MODELLING RESULTS

Visual inspections of seismic records are instructive and provide us with a rough insight into wavefield propagation complexities. However, with finite-difference modelling the wavefield can also be displayed as snapshots and the synthetic seismograms can be analysed in terms of apparent velocities (semblance analysis) and rms amplitude variations.

Table 1. Summary of models used in this paper. The 'prototype' model, shown in Fig. 5, was manipulated by assigning specific sediment, crust or upper-mantle physical properties to the various blocks. The *P* velocities for sediments, crust and upper mantle are 3.6, 6.7 and 8.2 km s^{-1}, respectively. *S* velocities are derived from *P* velocities using a Poisson's ratio of 0.25, while densities are derived from *P* velocities using Birch's law. 'Crustal Thinning' implies that the middle part of the crust is made 9 km thinner than in the 'prototype' model while otherwise retaining the model geometry. For models marked with 'Sediment Layers' all the blocks in the upper part of the model were given sediment properties. The 2 km thick sediment layer at the top was retained in all models. 'Moho Bump' means that the three blocks near the Moho were assigned upper-mantle physical properties. 'Velocity Perturbation' of 8 per cent rms in the graben area was used only for Model 5; see Fig. 11 and text.

Model	Crustal Thinning	Sediment Layers	Moho Bump	Velocity Perturbation
1	-	-	-	-
2	-	√	√	-
3	√	-	-	-
4	√	√	√	-
5	-	√	√	√

Seismograms

In contrast to real seismograms (Figs 2–4), even for the most extreme graben structures used in this study, the wave energy in the expected phase-velocity window for *Lg*, i.e. 3.2–3.9 km s^{-1}, is stronger than that for *Sn*. In the Hestholm *et al.* (1994) study, we found that both *Pn* and *Sn* were always relatively weak phases, as expected from the strong geometrical spreading effects of head waves, being roughly proportional to r^{-2}, where r is the epicentral distance. Somewhat stronger *Pn* and *Sn* waves were obtained by introducing velocity gradients and heterogeneities beneath the Moho, so that *Pn* and *Sn* become a mixture of head waves and scattered waves. For ray paths entirely within the Baltic Shield, the *Sn* phase is generally weak and often not reported by the analyst (Vogfjord & Langston 1990).

A comparison of real (Figs 2–4) and synthetic records (Fig. 6) shows that observed *Sn* is relatively strong and of long duration, clearly implying that a considerable amount of shear waves leak out of the crustal waveguide (Gregersen & Vaccari 1993). In contrast, the synthetics exhibit a relatively weak *Sn* and relatively strong *Lg* of long duration. This does not mean that there is no *Lg* blockage in our synthetics. First, synthetic sensor positions may be too close to the graben for leaking *Sn* phases to be observed. In addition, there is a considerable contribution of *Rg* waves, generated by scattering in the sedimentary basin, to the *Lg* wavetrain in our synthetics. Note that *Rg* waves are generally not observed on stations in Norway for paths longer than 100 km. The reason for this is that near-surface topography and heterogeneities, in combination with strong intrinsic attenuation in the uppermost 2 km of the crust, efficiently wipe out *Rg* waves for longer paths (Ruud *et al.* 1993).

Snapshots

Such plots, showing the total spatial wavefield for a specific time, are convenient for visualizing scattering phenomena, and, in our context, also the leaking of energy out of the crustal waveguide. The Model 2 synthetic wavefields are instructive for illustrating these phenomena, as shown in Fig. 7. The strongest amplitudes in these snapshots are associated with the crustal *S* waves, i.e. *Sg* and *Lg*. Further comments for each time frame are given below.

Time frame 60 s

In the first snapshot, the *P* phases are seen in the distance interval 390 to 440 km. (The *Pn* appears stronger than *Pg* here because the latter have mainly horizontal particle motion—not shown in the snapshots) A strong *Lg* wavetrain has developed and has just reached the graben structure. The direct *S* wave (*Sg*) propagates at a velocity of 3.9 km s^{-1} and is seen at about 235 km offset. The *Lg* wavetrain, observed as up- and down-going wavefronts, is spread over an interval from about 190 km and up to the *Sg* phase. While the *Sg* phase is the strongest one seen in the snapshots, it is rather weak in the synthetic seismograms extracted at the free surface (Fig. 6). Taking a closer look at the snapshots, it appears that the *Sg* phase is hardly 'reaching up' to the surface. In fact, this is consistent with the theory that an *SV* wave propagating parallel to the free surface of a half-space should result in zero amplitude

at the surface. This result is due to the combined effects of the incoming *SV*, the reflected *SV* and the inhomogeneous *P* waves (see Aki & Richards 1980, p. 190, Problem 5.6). Although our model has a thin sedimentary layer near the surface, this result still seems to be approximately valid. The largest amplitudes usually recorded in the *S* wavetrain, that is the *Lg* phase, are created by *S* waves that have been repeatedly reflected within the crust ('guided waves'). These waves have higher apparent velocities but lower group velocities than the *Sg* phase. The waves with the highest apparent velocities, still undergoing total reflection at the crust–mantle boundary, will have the same apparent velocity as the *Sn* phase, i.e. about 4.7 km s^{-1} in our model. These waves will terminate the *Lg* wavetrain since *S* waves with higher apparent velocities will loose part of their energy when reflected at the Moho interface. The 'group' velocity (distance divided by traveltime) of the latest *Lg* waves can be found as follows. The sine of the incidence angle is $3.9/4.7 = 0.82$. The horizontal component of velocity of such a ray will thus be $3.9 \times 0.82 = 3.2$ km s^{-1}. In the analysis of *Lg* amplitudes we have taken this group velocity to define the end of the *Lg* window. The upper-mantle *S* wave (the *Sn* phase) has propagated out to about 270 km at this first snapshot and travels faster than the crustal *S* waves, reaching the edge of the displayed section at the 100 s time frame, as can be seen in the subsequent time frames.

Time frame 70 s

The squeezing of the crustal *S* waves associated with thinning of the crystalline crust is obvious in this time frame as well. Some energy is transferred into the overlying sediments (220–260 km) and in the later part of the *Lg* wavetrain much of the energy leaks down into the mantle. The dipping Moho interface results in a smaller incidence angle of the rays here so that the *S* waves are only partially reflected (instead of total reflection which is the rule for guided waves such as *Lg*).

Time frame 80 s

The direct *Sg* waves have now passed the thinnest part of the crystalline crust and relatively little *Lg* wave energy remains in the crustal waveguide, while forward-propagating *S* waves under the uplifted Moho are relatively strong. In the sedimentary basin much of the *Sg* and *Lg* wave energy seems to be trapped.

Time frame 90 s

Direct *S* and *Lg* waves are still confined to the thinnest part of the crustal waveguide (see Fig. 5). Between 350 and 380 km the crystalline crust thickens again and some of the sub-Moho propagating shear waves leak back into the crust. *Rg* waves are particularly energetic in the sedimentary basin, having phase velocities between 2.0 and 2.5 km s^{-1}.

Time frame 100 s

The *Sg* wavefront has partly been restored and again fills most of the crustal waveguide. Some of the *S* waves, which have leaked down into the upper mantle due to crustal thinning, also propagate approximately horizontally and partially leak up again into the crust as *Sn* coda waves (see the rather strong upper-mantle *S* waves around 400 km).
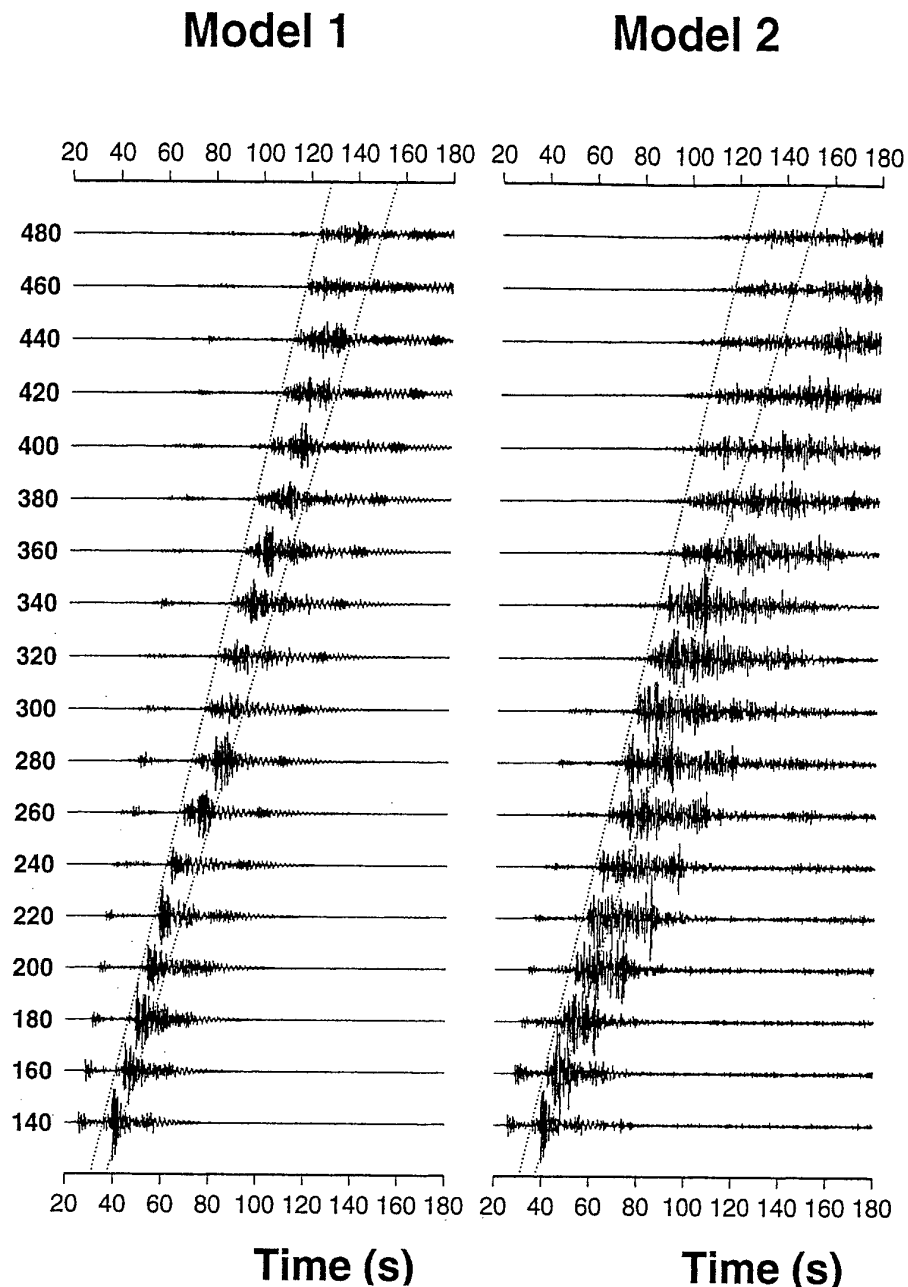
Model 1

Model 2

Figure 6. Synthetic seismograms for models 1 and 2 for the distance range 140–480 km using a station spacing of 20 km. The two dotted lines indicate the Lg group velocity window of 3.9 and 3.2 km s^{-1}. The numbers on the left are the distances from the source in kilometres. Up to about 150 km the two models are identical and the seismograms are very similar except for the backscattered waves seen in the later part of the Model 2 records. From 160 and up to 340 km the amplitude level in the Lg window is larger in the graben model (2) than in the reference model (1). There are several reasons for this: (i) the increased sediment thickness tends to amplify the waves, (ii) some body waves are converted to Rg waves at lateral heterogeneities near the surface, and (iii) some waves that are squeezed out of the crustal waveguide continue to propagate in the sediments as guided waves. Beyond 340 km, the crust gradually regains its normal structure and the partial blocking of the Lg phase becomes evident. The wave energy which was forced up into the sediment layers is delayed relative to the Lg phase and becomes smeared over a longer time interval. In both models the Sn phase is weak compared to Lg.

Time frame 110 s

For this timestep we show the wavefields for both Model 2 and Model 1 (lowest section). Note the different outlines of the Moho interface and sedimentary basin for the two sections.

The Sg and Lg waves of Model 2 have now left the graben structure and some blocking effect is clearly seen when comparing the two snapshots. For Model 1 the S wavefield is quite similar to that seen in the first snapshot, except for a horizontal stretching effect. The later part of the S-wavetrain

(*Lg*) has suffered more blockage than the *Sg* phase, which has propagated nearly horizontally in the middle part of the crust. By measuring amplitudes at 20 km depth, we find about 6 dB blocking for *Sg* and 9 dB for *Lg*. At the free surface the blocking is not so obvious; the *Sg* amplitude is very low for both models and the *Lg* waves are partially hidden by the strong surface waves confined to the sedimentary layer.

The essence of this series of snapshots is that when the *S* waves are 'forced' into the graben thinning areas, part of their energy is 'squeezed' out of the crystalline crust through *S*-to-*Rg* conversions in the sediments, and by shear waves penetrating the Moho interface. With increasing time and after the graben thinning area is overtaken, some *S* waves may leak back into the waveguide. In other words, a sort of *Lg* wavefield healing process appears to commence.

Semblance analysis

The synthetic records were also subjected to semblance analysis in specific distance intervals. This is essentially a time–velocity analysis convenient for the identification of various phases in the seismic records based on waveform similarities. It is computed as the normalized ratio of coherent energy to total energy within short moving time windows for varying stacking velocities (Taner & Koehler 1969). Semblance results for Model 1 (smooth) and Model 4 (complex) are displayed in Figs 8 and 9 for two distance ranges: 240–250 km and 300–310 km. In the first case, the smooth crustal waveguide model does not distort the synthetic wavefield much, as seen from the high semblance values signifying very good spatial correlation. *Pn* and *Pg* phase velocities in the velocity window 6.7–8.1 km s^{-1} are clearly observable in the time interval of 40–60 s with a subsequent *Sn* arrival at 62–67 s. These phases are followed by prominent *Sg* and *Lg* wavelets throughout the 67–90 s interval. The complex Model 4 wipes out signal correlations both for *P* and *S*, although we see some *P* and *S* scattered phases in the interval 42–52 s and *S*-to-*Rg* and *P*-to-*Rg* scattered phases (velocity range 2.0-2.5 km s^{-1}) in the interval 52–90 s. Semblance results in the distance range 300–310 km (Fig. 9) are quite similar to those at 240–250 km (Fig. 8). The Model 1 results are essentially unchanged except for a 10 sec time shift while those of the complex Model 4 show more *S*-type and *Rg*-type scattering contributions.

rms amplitudes

An instructive way to demonstrate how the seismic energy propagates across the model is given in Fig. 10 (Model 1—reference) and Fig. 11 (Model 5—perturbed graben model). Here the rms amplitude (in dB) for a 2 s moving time window is displayed as a function of distance and traveltime. *Pn* energy is reasonably well preserved in both models, while the distorted crustal waveguide beneath the graben (Model 5) effectively prevents *Pg*-type propagation (Fig. 11). *Sn* phases are visible in both models, and direct *Sg* waves are clear out to about 325 km. *Lg* energy is seen in the group-velocity interval 3.2–3.9 km s^{-1}, while in the interval 2.0–3.0 km s^{-1} *S*-to-*Rg* scattering contributions dominate. After passing over the graben (beyond 400 km), it is obvious that some of the *Lg* energy has been blocked for Model 5 as compared to Model 1. There is also a considerable amount of wave energy in

the upper-left part of Fig. 11 (but not in Fig. 10), which is identified as backscattered *Rg* waves.

In all discussion of *Lg* propagation, the term blockage is seldom given a quantitative definition. As mentioned, in the observational studies *Pn* and/or *Sn* phase amplitudes are used as a reference for measuring the extent of blockage. As demonstrated above, both *Sn* and in particular *Pg* phase amplitudes are affected by wavefield propagation through a complex waveguide. Our measure of relative *Lg* amplitude decay comes from comparing the root-mean-square (rms) amplitude distribution derived from the models with pronounced graben structure (Table 1) with those obtained for the reference model. The results are displayed in Figs 12 and 13 and the following comments apply: *Pn* amplitude decay is only a few decibels, while *Pg* amplitudes are down more than 12 dB or a factor of 4. *Sn* is down by a few to 6 dB, while the *Lg* waves, velocity interval 3.2–3.9 km s^{-1} are down 6–9 dB, i.e. a reduction by a factor of maximum 3, which is less than that for the *Pg* phase. In Figs 12 and 13, the slow *Rg* scattering wavelets appear as strongly amplified. The reason for this is that the reference models are almost void of *Rg* scattering contributions.

It was a bit disappointing to us that, even with realistic but nevertheless complex North Sea graben models, we are not able to synthesize *Lg* blockage as implied by real observations. The *Lg* amplitude reduction obtained is similar to that reported by Zhang & Lay (1995) in their normal model simulation of oceanic *Lg* blockage which they deemed successful. For our part, we do not entirely agree with this, since an amplitude reduction factor of 3 to 4 is hardly equivalent to blockage. In this respect we tend to agree with Maupin (1989), who also failed to simulate *Lg* blockage satisfactorily for the North Sea structure and thus concluded that *Lg* wave propagation was indeed robust. A potential defect of our waveguide models is that wave velocities are homogeneous within individual sedimentary layers, with constant velocities of respectively 6.7 and 8.1 km s^{-1} in the crystalline crust and below the Moho. As demonstrated by Hestholm et al. (1994), coda waves observed in local explosion and earthquake records require small-scale rms velocity perturbations of the order of 2–4 per cent. Since graben structures exhibit more structural variations than crustal layers, we introduced rms velocity fluctuations of 8 per cent (see Figs 11 and 13) to explore to what extent this would affect *Lg* propagation. The outcome is that *Lg* blockage amounted to roughly the same as for a very thin graben crustal waveguide, as implied by a visual comparison between Figs 12 and 13. A summary for this result section is that *Lg* blockage for realistic North Sea graben structures seldom exceeds 10 dB, even for the most extreme models. In other words, *Lg* propagation is very robust even under adverse structural conditions typical of graben areas.

In the above discussion we have identified various causes of *Lg*-blockage, such as (i) energy escaping through the Moho, (ii) energy delayed or converted in the sediments, or (iii) the thinning of the crystalline crust *per se*. It would be interesting to assess the relative importance of these mechanisms. Obviously, they cannot be considered to be independent of each other as, for instance, the thinning of the crystalline crust is a consequence of the thick sediments and the Moho shallowing. In physically realistic models, thick sediment basins are usually accompanied by thin crust (for isostatic compensation), but in our modelling experiments we can
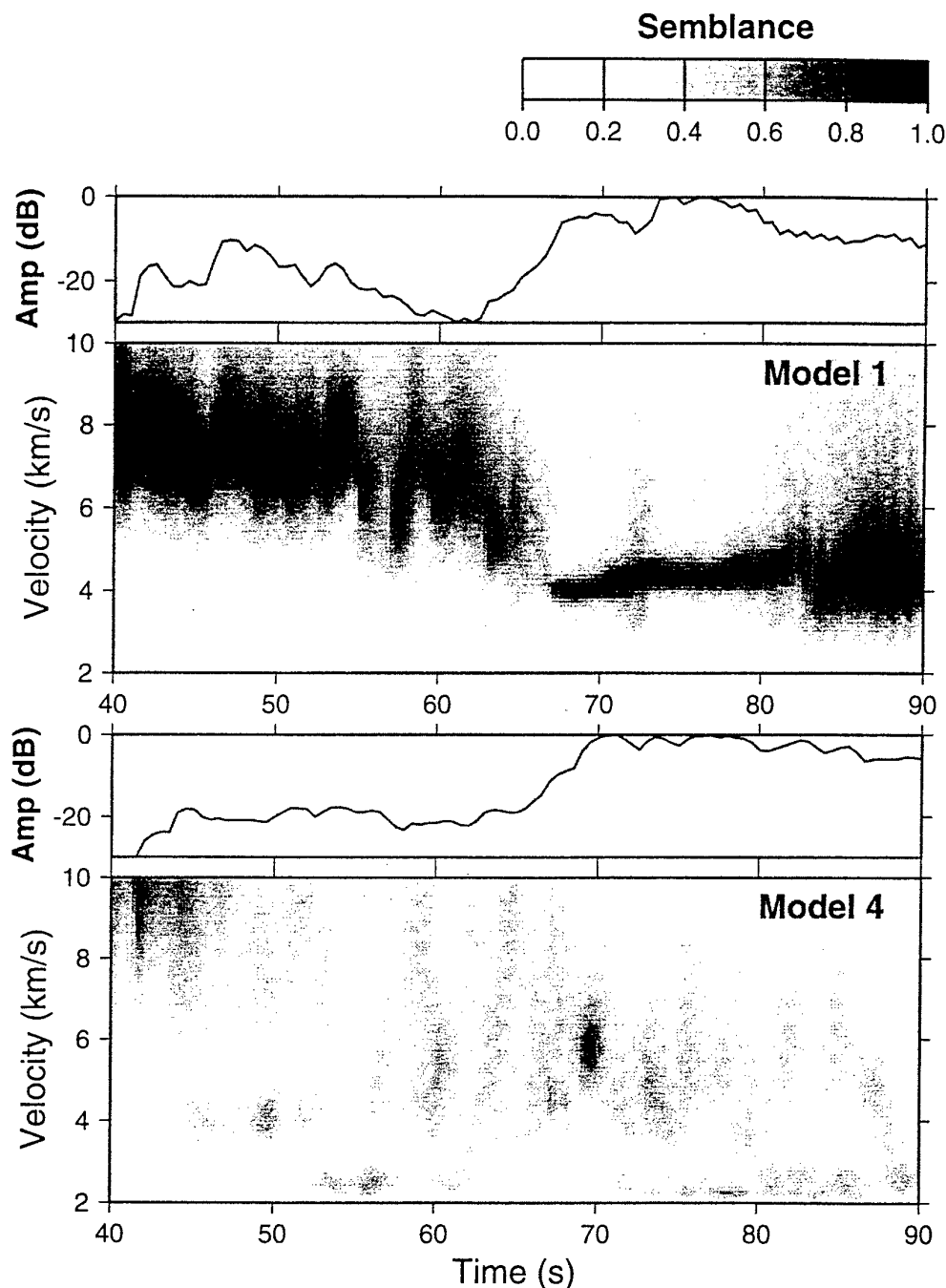
Semblance

Figure 8. Semblance analysis results for the distance range 240–250 km that is the graben entrance (see Fig. 10). The analysis was performed with bandpass-filtered (0.5–2 Hz) traces and a 1.5 s moving time window. The amplitude shown above each semblance plot is relative to the maximum rms amplitude of each section. For Model 1 (reference model—normal crust) the wavefield distortions are modest so the signal correlations across the 11 traces in this 10 km line array are good. Until the Lg waves start at about 65 s the synthetics are dominated by waves with apparent velocities above 6 km s^{-1}, i.e. P-type velocities. As expected, the apparent velocity in the Lg wavetrain is seen to increase slightly with time from about 4.0 to 4.2 km s^{-1}. For Model 4 (graben model with thin crust) the wavefield is severely distorted so semblance is weak. For this model the scattering contributions in terms of S (velocities about 4 km s^{-1}) and Rg waves (phase velocities slightly above 2.0 km s^{-1}) are seen over almost the entire time interval.

ignore this principle. Thus, besides the models in Table 1, we have tested a model with thick sediments but without Moho shallowing and another model with a shallow Moho but without thick sediments. These experiments indicate that thick sediments are a more effective blocking mechanism than crustal thinning. More interestingly, however, the sum of the individual blocking mechanisms (as measured in dB) is less than when they are working together. This result is reasonable:
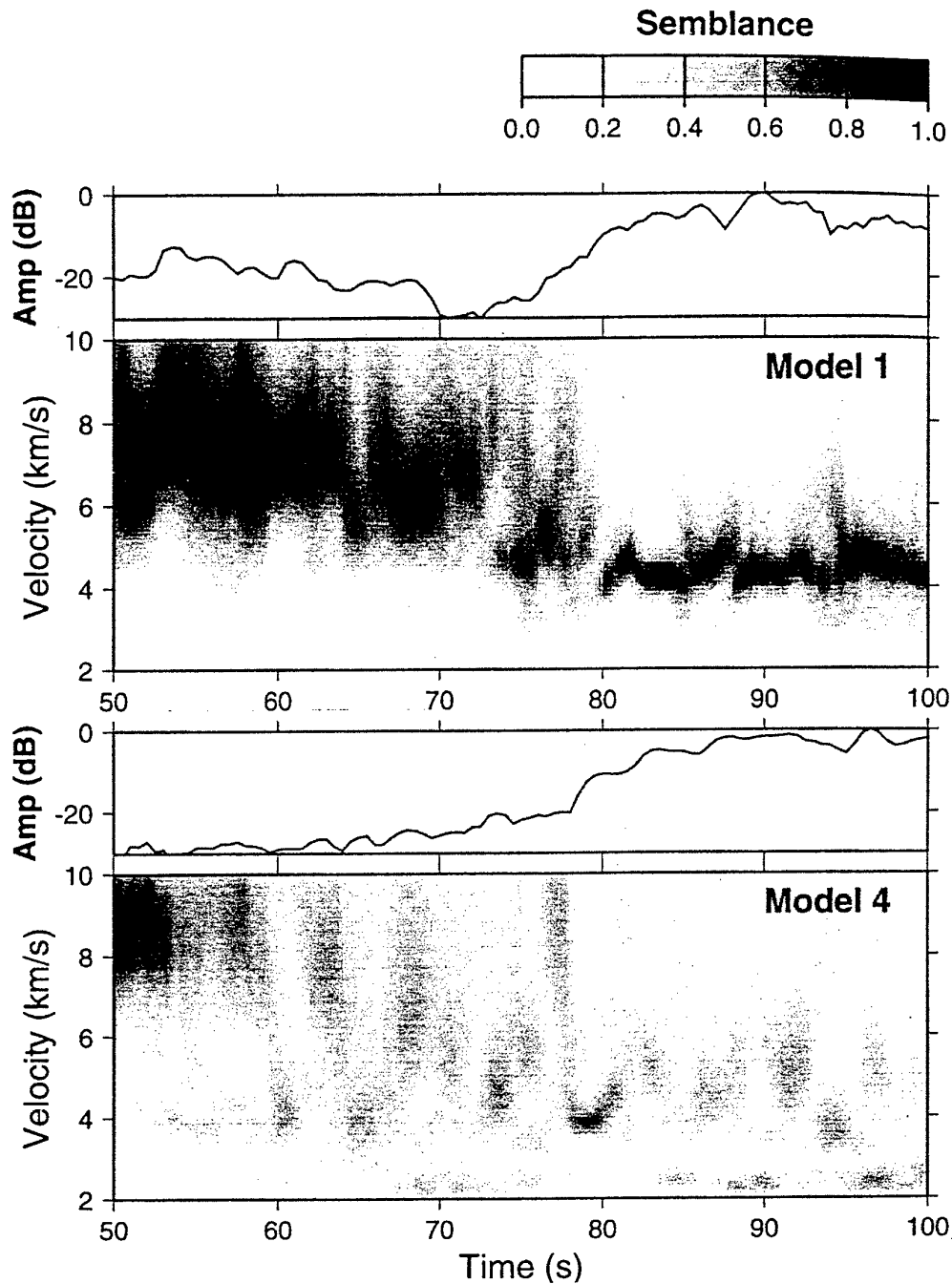
Semblance

Figure 9. Display of the semblance analysis results for the distance range 300–310 km, which is the central part of the graben structure for models 1 and 4. Results are quite similar to those in Fig. 8.

when the crystalline part of the crust gets thinner the Lg waves must undergo more reflections to traverse the same horizontal distance. Every time the waves are reflected from the free surface, they must pass through the sediments (except for the horizontally propagating Sg wave which is reflected from the bottom of the sediments). The delay these waves experience depends mainly on the sediment thickness and number of reflections. The conversion of Lg waves to Rg (or other waves)

in our model is probably controlled by the 'roughness' of the crust/sediment interface. We have not varied this parameter, so we cannot judge its importance. However, our model appears rather rough in this respect so it is unlikely that this effect is underestimated in our modelling. Lg wave energy 'penetrating' the Moho is most likely to occur for S waves with high apparent velocities, that is, for the later part of the Lg wave-train. For a Moho incidence angle of 10° less than the critical

angle, about 90 per cent of the energy will escape into the mantle (computed from plane-wave energy transmission/reflection coefficient). However, this mechanism is effective only while the *Lg* waves are propagating 'updip', whereas the effect of the thick sediments is active over the complete range of the graben structure.

To summarize, we find that the *combination* of thick sediments and thin crust is the most effective structural *Lg* blocking mechanism. This is confirmed by another result of our FD modelling experiments: if we compare the rms amplitudes of Model 2 with those of Model 1, we find that the *Lg* blockage is about 3 dB less than when comparing Model 4 with Model 3 (Fig. 12). The only difference between these two cases is the thickness of the crystalline part of the crust; the thicknesses of the sediments and the Moho structure are exactly the same. We also note that Model 2 is the one which best fits the North Sea grabens with respect to layer thicknesses.

DISCUSSION

From the results presented in the previous section, it is clear that even graben models with more adverse crustal thinning and velocity variations than what is found in the North Sea area are unable to block *Lg* waves to the extent observed. This also applies to cases where *Lg* traverse crystalline crust as thin as oceanic crust. With respect to model complexities, our modelling approach is very flexible in the sense that crucial crustal waveguide parameters, i.e. thickness, extent of sediment structures and Moho roughness, can easily be modified. In other studies, the Moho is often described by a simple ramp function and the sediment infill above by a trough. As mentioned, *Lg* blockage was not very efficient for our models—a factor of 2-to-4 in *Lg* amplitude reduction—so we introduced small-scale structural complexities in terms of 8 per cent rms velocity perturbation in the crust beneath the graben. The additional blockage effect of such extreme structures amounts to a maximum of 3 dB. In other words, *Lg* blockage cannot be fully attributed to structural features alone so the effect of intrinsic attenuation (*Q*) must be of importance. As mentioned, it is not a trivial task to incorporate such effects in a FD modelling scheme, although it can be done (Robertsson *et al.* 1995). However, since intrinsic attenuation is essentially a path-length effect, we can estimate fairly accurately the *Q* necessary to give a total *Lg* blockage of 20 dB relative to a 'normal' crust. In this regard we attribute 10 dB *Lg* amplitude loss to complex graben structures and need to account for an additional 10 dB amplitude reduction over a graben width of 100 km. In this regard, a *Q* value of 50 at 1 Hz (or 100 at 2 Hz) is needed for a 10 dB amplitude reduction. In continental crust, *Q* values are much higher but such values are not extreme in graben areas that have been subjected to much deformation in terms of stretching, thinning and block faulting. Literally a 'joker' in many geodynamical problems is the extent of water within the crust/upper mantle, since a water content of just a few per cent may significantly change physical rock characteristics (Anderson 1990). In the case of attenuation properties, rock inclusion of even moderate water content would tend to lower the *Q* value. Of course, it is not unreasonable to expect that crystalline rocks in oceanic and marine shelf areas have a higher water content than in continental areas. In other words, a 10 dB

amplitude reduction of *Lg* waves propagating through oceanic and graben areas of 100 km extent appears quite realistic.

At this stage, it may be appropriate to return to real North Sea seismic event recordings; a few examples are given in Figs 2–4. A remarkable feature for events 1 and 3 is the strong *Sn* phase, which, in addition, often has a long duration. Similar observations were reported by Baumgardt (1990) for events in Novaya Zemlya with paths crossing the Barents Sea. In contrast, all Canobe profiling shots in the North Sea (Fig. 2 in Kennett & Mykkeltveit 1984) exhibit weak *Sn* phases, irrespective of shot location west or east of the graben structures. For the three shot points west of the graben, the *Lg* phase is hardly visible compared with shot points east of the graben. The recordings here were at the NORSAR array to the east of the graben. Returning to our observations, Event 2 (Fig. 3) exhibits some remarkable features for an epicentre on the western side of the graben, namely that *Lg* is strong for the nearest stations on the west coast of Norway, while for stations further north (MOL and NSS) *Sn* is relatively strong and *Lg* correspondingly weak. This last point is the more surprising since the source–receiver paths to stations SUE and HYA initially coincide with those to MOL and NSS, so partial *Lg* blocking apparently takes place along the on-land path segments where sediments are lacking. For the MOL and NSS stations we notice the observational feature typical of events 1 and 3, namely a relatively strong *Sn* phase of considerable duration. These *Sn* features are typical for cases where *Sn* is relatively strong and *Lg* correspondingly weak, so it is tempting to explain this in terms of *Lg* leakage from the crustal waveguide into the mantle where subsequently some of it is returned to the crust and appears at the free surface as delayed *Sn* phases. The mode of returning *S*-wave energy leakage from the crustal waveguide is demonstrated in our snapshots of the synthetic wavefield (Fig. 7). The example with *Sn–Lg* recordings for stations MOL and NSS for Event 2 clearly rules out the strong *Sn* phase being a specific source effect. In general, for most local event recordings in Fennoscandia the *Sn* phase is at best weak and sometimes not observable at all. In this respect, the strong *Sn* phases often seen in North Sea event recordings could be a result both of strong attenuation of the *Lg* waves in the crust and of excessive *S*-wave energy in the upper mantle due to *Lg* leakage. We may have simulated this phenomenon more realistically by introducing a strong velocity gradient just below the Moho so that *Sn* becomes a combination of direct (head) and diving waves and thus appears stronger (Hestholm *et al.* 1994).

Finally, we also examined some of the observational evidence reported in the literature for *Lg* blockage in the North Sea. When *Lg* amplitude decay is estimated from the *Sn/Lg* ratio there may be a bias since *Lg* energy leaking into the mantle seemingly returns later in the *Sn* coda. Another aspect here is that in the North Sea *Lg* blockage and graben structural complexities are almost synonymous concepts, which in turn reflect observational results presented by Gregersen (1984) and Kennett *et al.* (1985) among others. Kennett *et al.* (1985) used a back projection scheme for identifying blockage areas in the North Sea and found these to be coincident with the dominant Central and Viking grabens (Fig. 1). A visual inspection of the observational data at hand gave that the wave path cross-sampling was poor; that is *Lg*-blockage contributions may also reflect off-graben structural peculiarities. In essence, graben blockage of *Lg* waves may be less than generally assumed and
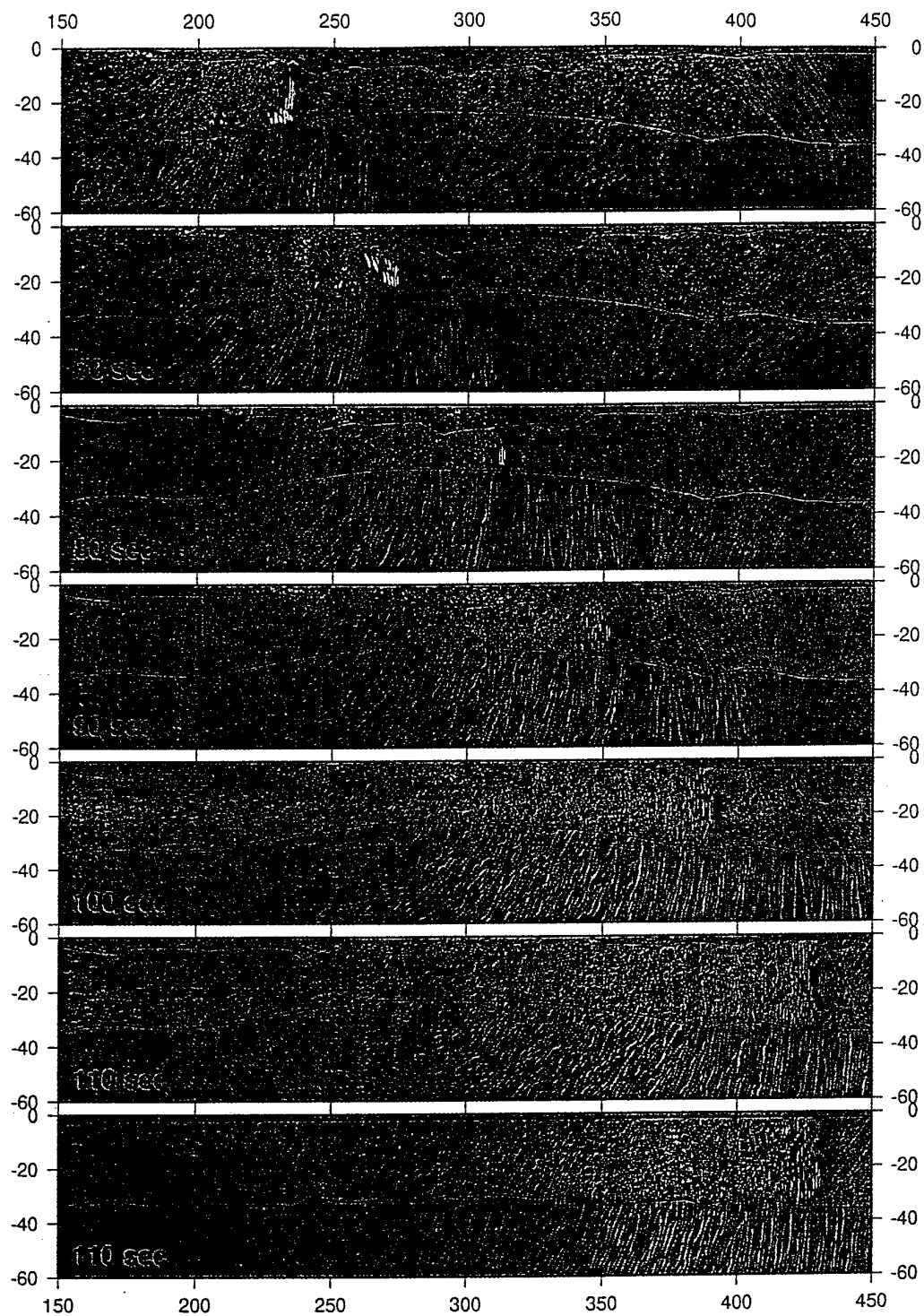
Figure 7. A series of snapshots illustrating wave propagation through a typical graben area (Model 2 in Table 1). The horizontal axis gives the distance from the source (in km) and the vertical axis gives the depth from the surface (in km). The Moho and the sediment/crust interfaces are shown as solid lines. The time (in s) is given in the lower left corner of each snapshot. The two last snapshots are for the same time but for different models—in the lowermost snapshot, the wavefield of Model 1 is shown for comparison. See text for discussion.
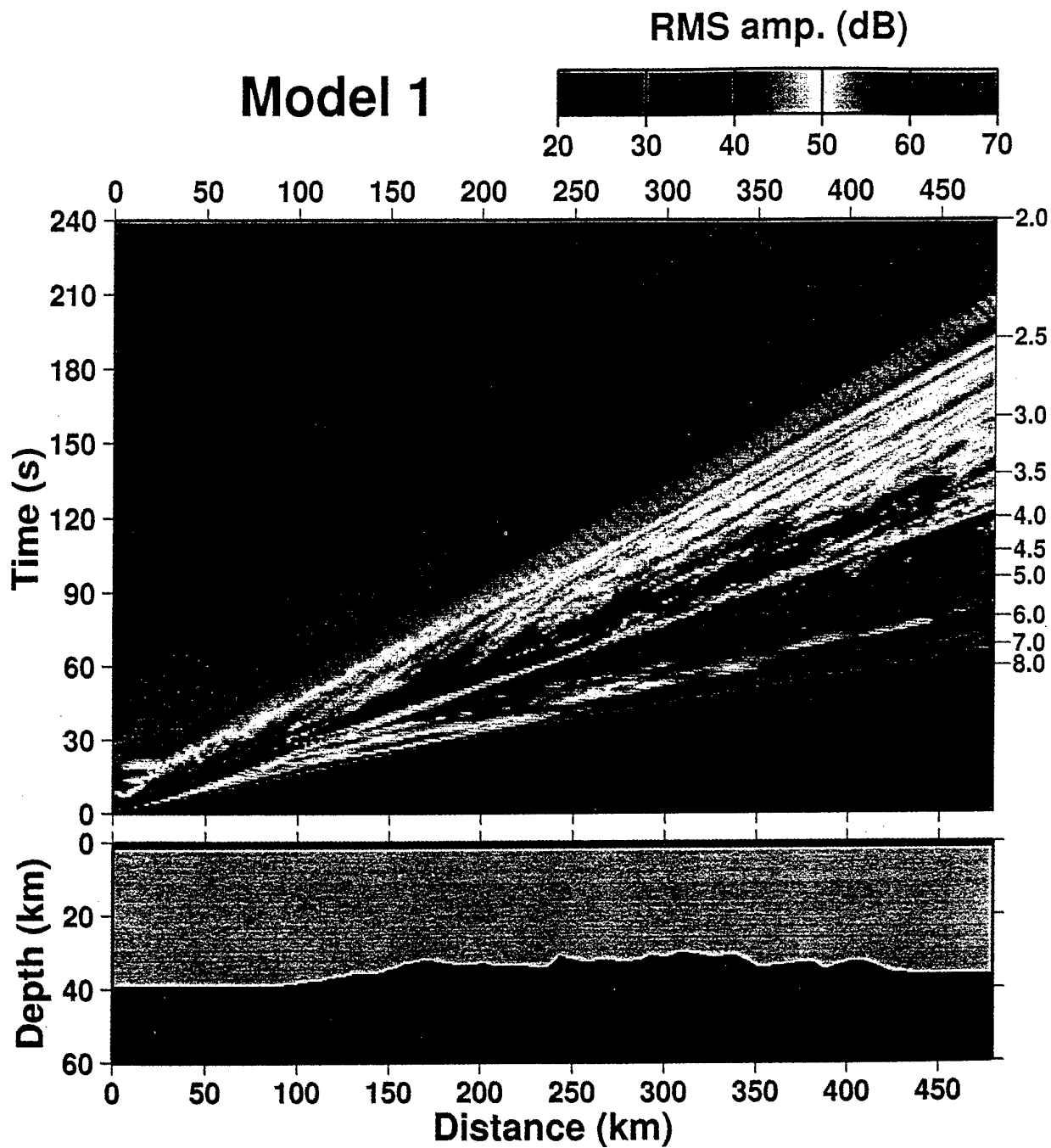
Figure 10. RMS amplitude display for Model 1 (the reference model). The lower part of the figure shows a section of the model. RMS amplitudes were computed for each sensor at the surface (1 km spacing) with a 2 s long moving time window. On the right vertical axis of the rms plot the group velocities are given in km s^{-1}. Typical *Lg* group velocities are in the interval 3.2 to 3.9 km s^{-1} and coincide with the strongest amplitude in this plot.
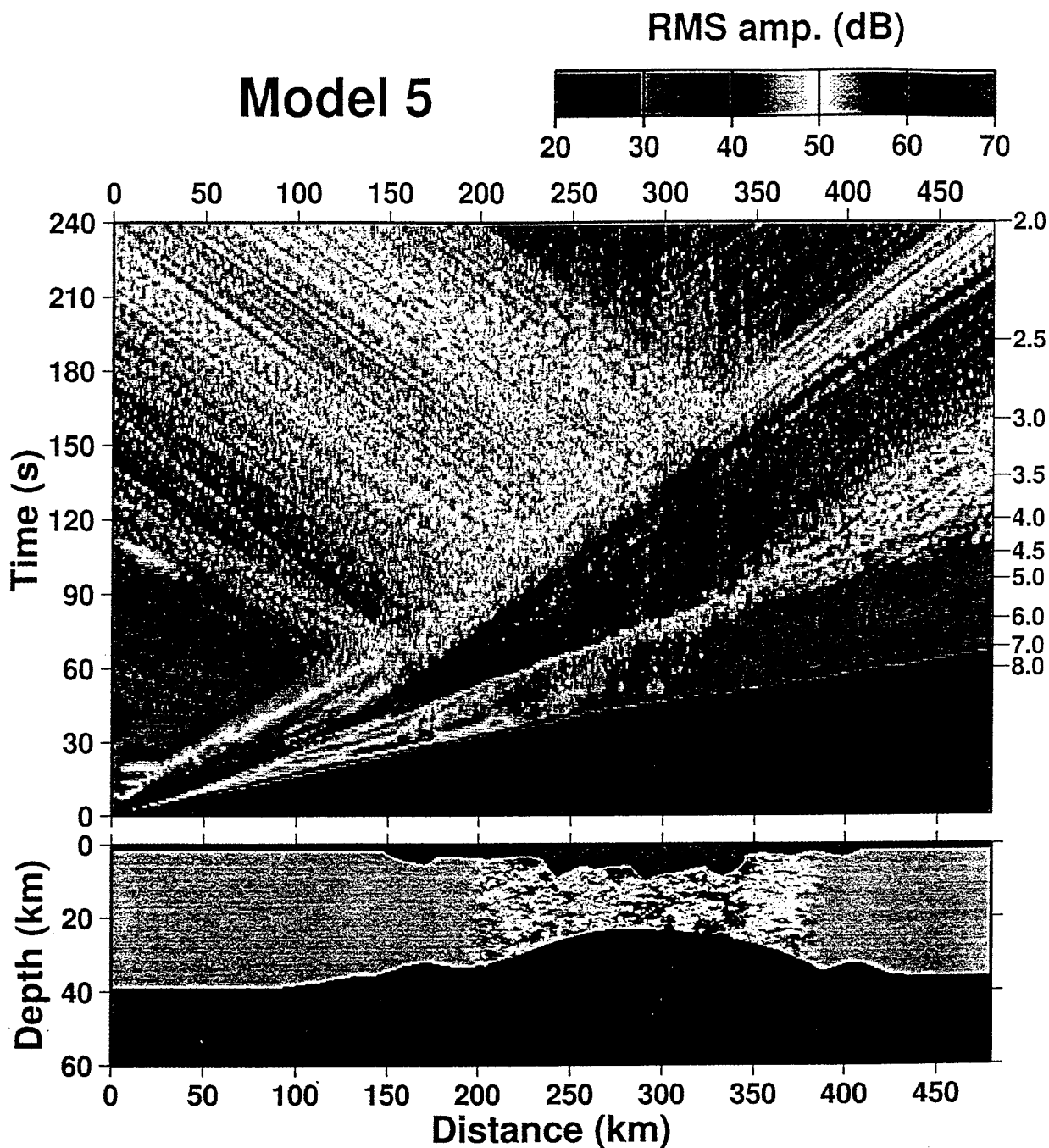
Figure 11. RMS amplitude display for Model 5 with 8 per cent velocity perturbation of the crustal velocities in the graben region as shown in the lower part of the figure. *Pg* and *Lg* amplitudes are reduced compared to Model 1 (Fig. 10), while the outstanding features are the large amplitudes stemming from forward and backward *S*-to-*Rg* scattering from the sedimentary basins and in particular from the perturbed region. The group velocity of these *Rg* waves (propagating mainly in the sedimentary layer) is less than 2.0 km s^{-1}.
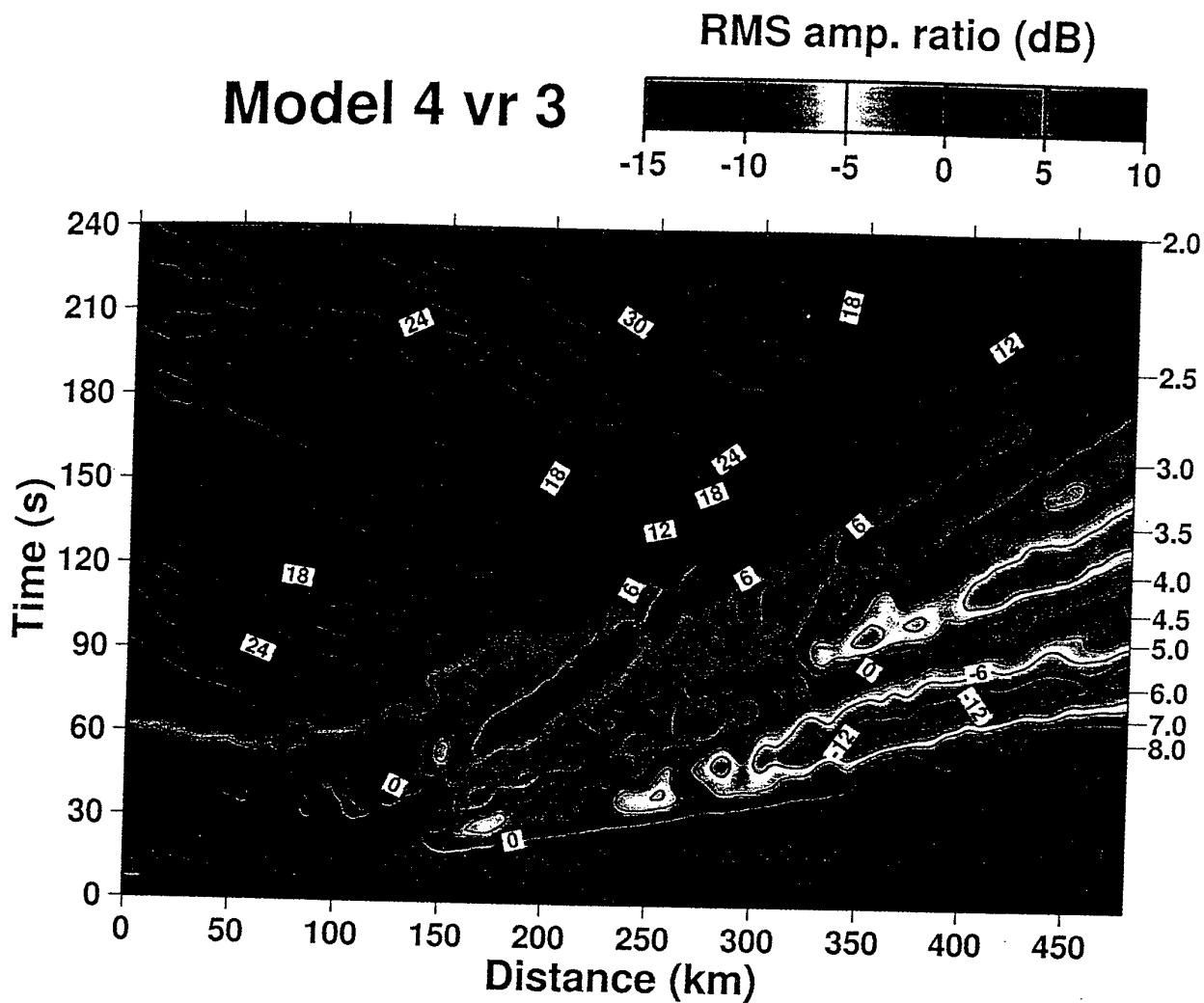
Figure 12. Relative rms amplitudes for the Model 4 versus Model 3 wavefields. The relative amplitudes were computed from rms amplitudes similar to those shown in Figs 10 and 11. Before contouring, the image was smoothed with a rectangular cosine tapered window of size 10 s by 10 km. The light shading implies amplitude losses (blockage), which in this case seldom exceeds 6 dB for the most effectively blocked Lg waves (group velocity about 3.5 km s^{-1}) and 12 dB for Pg (group velocity about 5.5 km s^{-1}). The strong amplification (positive dB values) in the upper left part of the figure is due to the fact that the reference model (3) is practically void of scattered Rg waves.
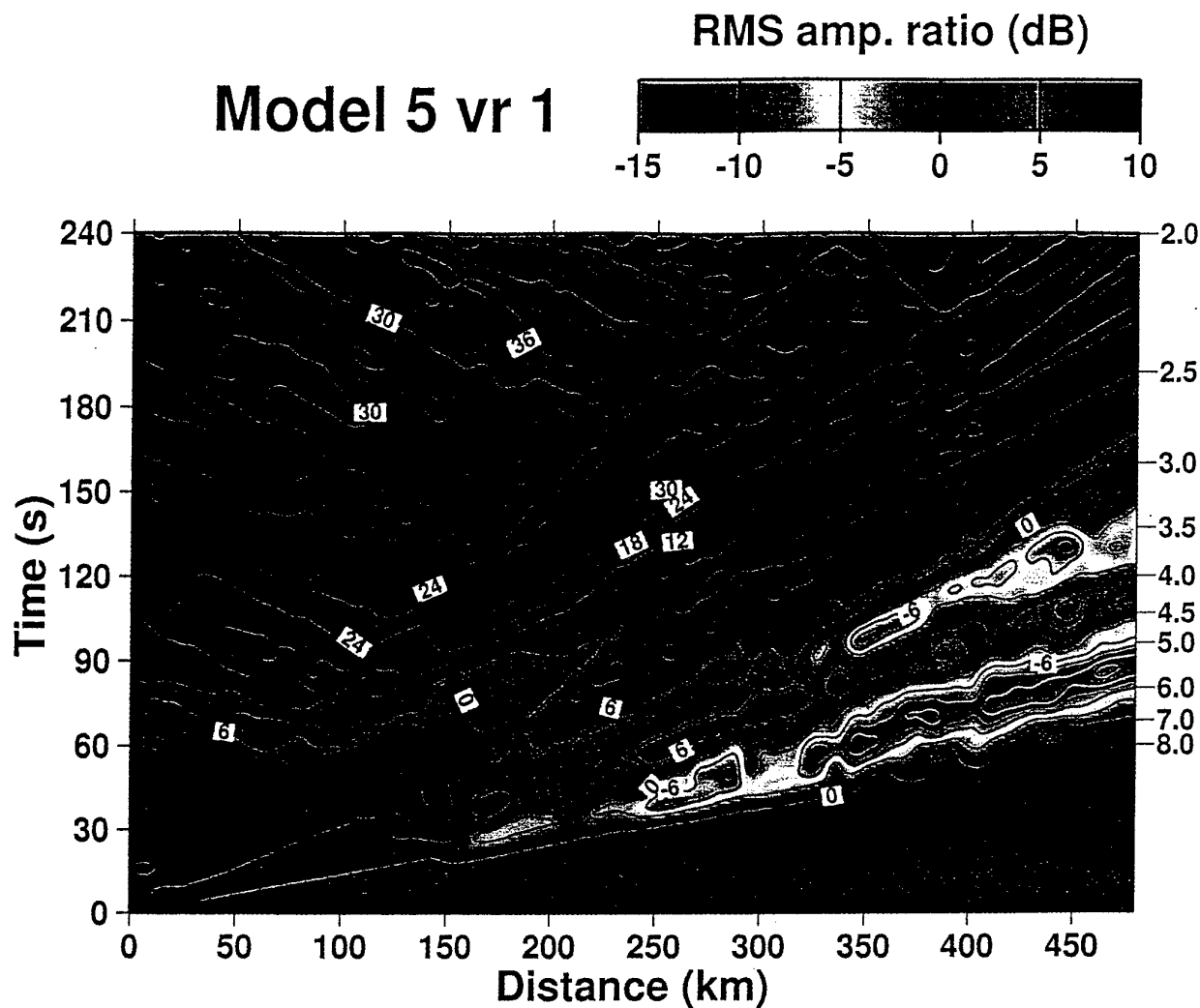
Figure 13. Relative rms amplitudes of the most complex crustal model (5, Fig. 11) considered in our blockage analysis as compared to the reference model (1, Fig. 10). The relative amplitudes were computed and plotted in the same way as for Fig. 12. *Lg* blockage is also in this case moderate, with a maximum of about 9 dB. The additional *Lg* blockage of the perturbed Model 5 is generally less than 3 dB higher than for the corresponding unperturbed Model 2.

hence the current gap between observed and calculated *Lg* blockage may in fact be less than presumed. The three sets of event records displayed in Figs 2–4 imply an *Lg* blockage of roughly 20, 0 and 6 dB, respectively, based on M_L magnitude differences using *Pn* and *Lg* amplitudes (Mendi & Husebye 1995). By far the strongest blockage is obtained for Event 1, which also has the longest wave paths. For Event 2, there is no apparent *Lg* blockage for the coastal stations, except for MOL and NSS where the blockage is about 6 dB and takes place along the non-marine path segment. For Event 3, the *Lg* blockage is 6 dB on average.

The North Sea grabens are obviously related to *Lg* blockage but not in a uniform manner. Our Event 2 (Fig. 3) is one such example, and Gregersen (1984) gives observational evidence of non-blocking *Lg* paths through North Sea graben areas. The Himalayas are also well known for efficient *Lg* blockage (Ruzaikin *et al.* 1977), although non-blocking *Lg* paths can be found (Mykkeltveit & Husebye 1981). In other words, very efficient *Lg* blockage appears to be related to special crustal features like graben and mountain ranges. Strong intrinsic attenuation (low *Q* values) is one obvious candidate here while others may be sharp basin wedges towards crystalline rocks and extensive cracks and faults due to relative recent tectonic reworkings. Naturally, *Lg*-blockage mechanisms as mentioned here may also exist outside graben areas as exemplified by the Event 2 recordings at MOL and NSS. In a recent study, Xie & Lay (1993) demonstrated the problem of identifying clear *Lg* blocking mechanisms—not unexpected in view of the large fluctuations in the observational data.

Finally, a possible limitation in our 2-D FD modelling experiments, besides that of not incorporating intrinsic *Q* attenuation, is that the code is for two dimensions. We intuitively expect to have more severe scattering in a 3-D environment and less scattered wavelets would return into the model 'box'. On the other hand, grabens are dominantly 2-D tectonic features and most of the North Sea observational data are for paths nearly perpendicular to the elongated graben. There also seems to be a clear relationship between strong *Sn* and weak *Lg*, i.e. a considerable fraction of *Lg* energy leaking into the mantle reappears in the *Sn* coda. These features are not clear in our synthetics, as they would require a strong positive velocity gradient beneath the Moho and/or a more laminated or heterogeneous sub-Moho structure for proper modelling (Hestholm *et al.* 1994).

CONCLUSIONS

In this study, we have simulated *Lg* blockage phenomena for realistic North Sea graben structures using 2-D finite-difference (FD) synthetics although intrinsic *Q* attenuation is not incorporated. The main results are as follows.

(1) For extremely thin graben models with crystalline crust thicknesses of about 5 km plus sedimentary basins, *Lg* blockage amounts to 6–9 dB.

(2) When an 8 per cent rms velocity perturbation was added in the graben crust only a few extra decibels *Lg* decay were obtained.

(3) The dominant structural *Lg*-blockage mechanisms are the delay of the *Lg* waves in the thick sediments, *Lg*-to-*Rg* conversions (scattering) by lateral heterogeneities in the sediments, and *Lg*-wave leakage out of the crustal waveguide.

(4) The above-mentioned *Lg* blockage mechanisms are more efficient in a thin crust than in a thick crust.

(5) Part of the mantle waves are returned to the crust and appear in the *Sn* coda.

(6) Real *Lg* observations require a somewhat strong blockage of the order of 15-20 dB which in turn require relatively strong intrinsic attenuation. A *Q* value of 100 at 2 Hz would suffice in this regard.

(7) Our synthetics agree well with similar studies, although some authors concluded optimistically that synthetic blockage simulated real conditions well at *ca.* 6–10 dB amplitude reductions.

(8) We also made comparisons with real observations (records from West Norway stations shown for three earthquakes in the North Sea), where a strong *Sn* phase with an extended coda is often synonymous with strong *Lg* blockage.

(10) *Lg* blockage has also been observed outside the North Sea Graben area, so blockage mechanisms must be complex and again low *Q* (strong attenuation) is likely to be a decisive factor.

Our final concluding statement is that *Lg* exhibits very robust propagation characteristics and except for high intrinsic attenuation or very thin crustal waveguides in combinatin with thick sediments it is difficult to pinpoint specific blockage mechanisms.

ACKNOWLEDGMENTS

The authors would like to thank Drs Søren Gregersen and Anton M. Dainty for many useful discussions on *Lg* blockage. Dr Yann Grundt is thanked for his assistance in generating the prototype model. Many of the figures in this paper were produced using GMT (Wessel & Smith 1991). This work was supported by the Air Force Office of Scientific Research, USAF under Grant F49620-94-1-0278.

REFERENCES

Anderson, D.L., 1990. *Theory of the Earth*, Blackwell Scientific Publications, Boston, MA.

Barton, P. & Wood, R., 1984. Tectonic evolution of the North Sea basin: crustal stretching and subsidence, *Geophys. J. R. astr. Soc.*, **79**, 987–1022.

Båth, M. (1954). The elastic waves Rg and *Lg* along Euraistic Paths, *Arkiv Geofysik*, **2**, 295–342.

Baumgardt, D.R., 1990. Investigation of teleseismic *Lg* blockage and scattering using regional arrays, *Bull. seism. Soc. Am.*, **80**, 2261–2281.

Bouchon, M., 1981. A simple method to calculate Green's function for elastic layered media, *Bull. seism. Soc. Am.*, **71**, 959–971.

Campillo, M., Feignier, B., Bouchon, M. & Bethoux, N., 1993. Attenuation of crustal waves across the Alpine Range, *J. geophys. Res.*, **98**, 1987–1996.

Cao, S. and K.J. Muirhead (1993). Finite difference modelling of *Lg* blockage, *Geophys. J. Int.*, **115**, 85–96.

Chazalon, A., Campillo, M., Gibson, R. & Carreno, E., 1993. Crustal wave propagation anomaly across the Pyrenean Range. Comparison between observations and numerical simulations, *Geophys. J. Int.*, **115**, 829–838.

Gabrielsen, R.H., Færseth, R.B., Steel, R.J. & Kløvjan, O.S., 1990. Architectural styles of basin fill in the northern Viking Graben, in *Evolution of the North Sea Rifts*, pp. 158–179, eds Blundell, D. & Gibbs, A., Oxford University Press, Oxford.

Gregersen, S., 1984. *Lg* wave propagation and crustal structure differences near Denmark and the North Sea, *Geophys. J. R. astr. Soc.*, **79**, 217–234.

Gregersen, S. & Vaccari, F., 1993. *Lg*-wave modelling for the North Sea, *Geophys. J. Int.*, **114**, 76–80.

Gregersen, S., Panza, G.F. & Vaccari, F., 1988. Developments toward computations of synthetic seismograms in laterally inhomogeneous anelastic media, *Phys. Earth planet. Inter.*, **51**, 55–58.

Hestholm, S.O., Husebye, E.S. & Ruud, B.O., 1994. Seismic wave propagation in complex crust-upper mantle media using 2-D finite-difference synthetics, *Geophys. J. Int.*, **118**, 643–670.

Israelsson, H., 1994. Analysis of historical seismograms: Root mean square Lg magnitudes, yields and depths of explosions at the Semipalatinsk test range, *Geophys. J. Int.*, **117**, 591–609.

Kennett, B.L.N., 1986. *Lg* Waves and structural boundaries, *Bull. seism. Soc. Am.*, **76**, 1133–1141.

Kennett, B.L.N. & Mykkeltveit, S., 1984. Guided wave propagation in laterally varying media—II. *Lg* waves in north-western Europe, *Geophys. J. R. astr. Soc.*, **79**, 257–267.

Kennett, B.L.N., Gregersen, S., Mykkeltveit, S. & Newmark, R., 1985. Mapping of crustal heterogeneity in the North Sea basin via the propagation of *Lg*-waves, *Geophys. J. R. astr. Soc.*, **83**, 299–306.

Maupin, V., 1989. Numerical modelling of *Lg* wave propagation across North Sea Central Graben, *Geophys. J. Int.*, **99**, 273–283.

Mendi, C.D. & Husebye, E.S., 1995. Near real time estimation of seismic event magnitude and moment via *P* and *Lg* phases, in *Proceedings of Earthquakes Induced by Underground Nuclear Explosions*, pp. 281–300, eds Console, R. & Nikolaev, A., Springer, Berlin.

Mykkeltveit, S. & Husebye, E.S., 1981. *Lg* wave propagation in Eurasia, in *Identification of Seismic Sources–Earthquake or Explosion?*, pp. 421–451, eds Husebye, E.S. & Mykkeltveit, S., Reidel, Dordrecht.

Press, F. & Ewing, M., 1952. Two slow surface waves across North America, *Bull. seism. Soc. Am.*, **42**, 219–228.

Regan, J. & Harkrider, D.G., 1989. Numerical modelling of SH *Lg* waves in and near continental margins, *Geophys. J. Int.*, **98**, 107–130.

Robertsson, J.O.A., Blanch, J.O. & Symes, W.W., 1995. Viscoelastic finite-difference modeling, *Geophysics*, **59**, 1444–1456.

Ruud, B.O., Husebye, E.S. & Hestholm, S.O. (1993). Rg observations from four continents: inverse- and forward-modelling experiments, *Geophys. J. Int.*, **114**, 465–472.

Ruzaikin, A.I., Nersesov, I.L., Khalturin, V.I. & Molnar, P., 1977. Propagation of *Lg* and lateral variations of crustal structure in Asia, *J. geophys. Res.*, **82**, 307–316.

Taner, M.T. & Koehler, F., 1969. Velocity spectra—digital derivation and applications of velocity functions, *Geophysics*, **34**, 859–881.

Vogfjord, K.S. & Langston, C.A., 1990. Analysis of regional events recorded at NORESS, *Bull. seism. Soc. Am.*, **80**, 2016–2031.

Wessel, P. & Smith, W.H.F., 1991. Free Software Helps Map and Display Data, *EOS, Trans. Am. geophys. Un.*, **72**, 441.

Xie, X.B. & Lay, T., 1994. The excitation of *Lg* waves by explosions: A finite-difference investigation, *Bull. seism. Soc. Am.*, **84**, 324–342.

Xie, X.B. & Lay, T., 1995. The log(rms *Lg*)-mb scaling law, *Bull. seism. Soc. Am.*, **85**, 834–844.

Zhang, T.R. & Lay, T., 1995. Why the *Lg* phase does not traverse oceanic crust, *Bull. seism. Soc. Am.*, **85**, 1665–1678.

Zhang, T.R., Schwartz, S.Y. & Lay, T., 1994. Multivariate analysis of waveguide effects on short-period regional wave propagation in Eurasia and its application in seismic discrimination, *J. geophys. Res.*, **99**, 21 929–21 945.

Appendix 5

Instabilities in applying absorbing boundary conditions to high order seismic modeling algorithms

A. Simone[1] and S. Hestholm[2]

[1] ENEA-Energy Research Center, Casaccia, Via Anguillarese 301, 00060 S. Maria di Galeria, Rome, Italy

[2] Rice Univ., dept. of Geology and Geophysics, 6100 Main, Houston, TX 77005-1892.

Introduction

The problem of artificial reflections from grid boundaries in the numerical discretization of elastic and acoustic wave equations has since long plagued geophysicists. Even if modern computers have made it possible to extend the synthetics over more wavelengths, equivalent to larger propagation distances, efficient absorption methods are still needed in order to minimize interference from unwanted reflections from the numerical grid boundaries. In this study we examine applicabilities and stabilities of the Optimal Absorbing Boundary Condition (OABC) of Peng and Toksöz (1994, 1995) for 2-D and 3-D acoustic and elastic wave modeling. As a basis for comparison we use the Exponential Damping (ED) (Cerjan et. al. 1985), in which velocities and stresses are multiplied by progressively decreasing terms when approaching the boundaries of the numerical grid.

Peng and Toksöz (1994, 1995) emphasized the importance of stability in the choice of aborbing boundary condition. As an example, they mentioned that Emerman and Stephen (1983) demonstrated that the boundary condition of Clayton and Engquist (1977) was unstable for a wide range of elastic parameters, and further that Mahrer (1986) found the boundary condition of Reynolds (1978) to be unstable as well. Peng and Toksöz (1994) gave some examples of 3-D elastic finite-difference simulations where OABC was used. The employed scheme was 4th order accurate in space and 2nd order accurate in time.

Elastic wave propagation in an unbounded homogeneous medium (without a free surface), were simulated, and the results were stable. They also made a comparison between the OABC, Reynolds' (1978) and Higdon's (1990) boundary conditions and found that using the OABC led to less artificial reflections than the two other schemes. Our study may be considered a further test of absorbing boundary conditions. We therefore implement both the OABC and ED in our 2-D finite-difference elastic wave algorithm (Hestholm and Ruud, 1994) and check their respective performances. Our goal is to find higher order accuracy algorithms using both methods.

2-D finite-difference implementation

We employ a 2-D finite-difference velocity-stress formulation (Hestholm and Ruud, 1994), that solves the equations governing wave propagation in an elastic isotropic medium. Following Levander (1988) and Virieux (1986) we discretize the elastodynamic equations with two staggered numerical space differentiators. Details of this numerical discretization can be found in Kindelan et al. (1990), who developed optimal spatial finite difference methods based on the work of Holberg (1987). In the present work we use a method which is spatially accurate to 8th order in the interior of the computational domain. For time stepping a leap frog technique (accurate to 2nd order) is used. This allows us to achieve an upper bound of 1.5% for the relative error of the numerical group velocity at only 3 nodes per wavelength. A schematic of our staggered grid is given in Figure 1.

The OABC method extrapolates values on the numerical edges of a finite-difference grid. We express these values as a linear combination of the wave field at previous time steps and/or interior grids by exploiting the zeros and poles of the reflection coefficients in the complex plane. Approaching the grid edges, including the free surface, we apply successively lower order central, staggered finite-difference operators used for discretizing the spatial derivatives. We apply stress-free boundary conditions at the upper boundary. OABC is used at the bottom and sides of the grids. It is worthwhile to note that in the

implementation of the OABC it is important to avoid using corner points of the staggered grid.

The ED method involves some restrictions on the useable part of our computational grid, since it is necessary to generate finite thickness damping strips along the grid edges. We exponentially damp velocity and stress in the strip by multiplying them by $\exp(-(\alpha \times \Delta)^2)$. Δ is the number of grid points to the inner boundary of the strip, and α is a constant equal to 0.015. Damping is enforced within absorption strips of 20 grid points or 7 wavelengths at 60 Hz and 1 wavelength at 10 Hz along the bottom and the sides of the grid. For both OABC and ED, the coefficients are precomputed before time extrapolation is started.

Test cases

In our numerical tests the model size is 100 km by 70 km, or 40 by 30 wavelengths at the central frequency of 2.5 Hz, giving 351 grid points vertically and 501 grid points horizontally for a grid size of $\Delta x = \Delta z = 0.2$ km. We design two different types of models in order to compare the artificial reflections using the OABC and the ED. The first model is homogeneous with a constant P-velocity of 7.1 km/s. The second model is a multilayer realization of the crust and upper mantle consisting of several constant velocity layers (Figure 6). In all cases the S-wave layer velocity is related to the P-wave velocity via the Poisson ratio of $v_p/v_s = \sqrt{3}$. Densities ρ are linear functions of the P-velocities: $\rho = 0.613 + 0.000328 \cdot v_p$, given in kg/m^3 with v_p given in m/s. The source is a Ricker wavelet (derivative of a Gaussian) in both space and time and is located 50 km from the left edge of the grid and 0.5 km below the surface.

Stability of OABC

We found that the OABC became unstable for long time simulations when using our 8th order accurate finite difference algorithm. We tried to use 8th order of accuracy in the interior of the domain combined with second order along three levels adjacent to the absorbing boundaries (thus a very sharp discontinuity in the order of accuracy). We encountered

---

Optimal Absorbing Boundary Condition   3

instabilities after O(100) time steps, with the instability being initiated either along the absorbing boundaries or at the bottom corners of the computational grid. As already mentioned, Peng and Toksöz (1994) achieved stable results for the OABC when used with spatially 4th order accurate schemes in a 3-D homogeneous medium. Thus for a realistic test of OABC using our scheme it was natural to experiment with lowering the spatial finite-difference order. This led to successful runs whether using 2nd or 4th order accurate finite-difference operators throughout the grid; in both cases we obtained completely stable runs with greater numerical dispersion.

We therefore modified the OABC algorithm to achieve stability in our higher order scheme, thereby obtaining higher accuracy. We solved the problem by decreasing the finite-difference order gradually when approaching the boundaries. We had to perform several tests in order to find the proper number of grid points near the boundaries on which to apply a certain finite-difference order. It seems important to use 2nd order finite differences at exactly two grid points adjacent to the boundaries. Inside this layer the number of grid points of higher order finite differences should be increased gradually with order up to where the 8th order method starts.

In our implementation we arrived at a total number of 12 grid points adjacent to the boundaries at which the finite-difference order were gradually lowered. We used 8th order in the interior of the grid, then 6th, 4th and 2nd order as approaching the boundaries. The following procedure was found to be optimal (in the sense that it delayed instabilities the longest) in our scheme when approaching the grid boundaries: 6 layers of 6th order finite differences, then 4 layers of 4th order and finally 2 layers of 2nd order adjacent to the grid boundary. In this way we were able to run for at least 14000 time steps (about 60 seconds of simulated time) before a slowly growing instability started appearing along the absorbing boundaries. Simulating wavefields for such large time laps enable the most interesting wave phenomena to be adequately synthesized.

The OABC requires the zeros and poles of the reflection coefficients to be in the first quadrant of the complex plane (Peng and Toksöz, 1994, 1995), which leads to $k\Delta x \leq \pi/2$,

where Δx is the grid size and k the wavenumber. From this it follows that $\Delta x \leq \lambda/4$, where $\lambda = 2\pi/k$ is the shortest wavelength. Therefore the OABC requires at least 4 samples per shortest wavelength to ensure stability, at least near the grid edges. In our context of a broadband Gaussian point source this cannot be ensured, since we do not have explicit control over the complete frequency range that propagates. The Ricker wavelet source is widely used in seismic simulations. However, the central frequency of the source is 2.5 Hz, which leads to a wavelength of 2.8 km for our choice of P-wave velocity in the homogeneous medium. This leads to 14.2 samples per wavelength, which is 3.5 times more than is needed for the OABC. Nevertheless, the source excites also a high-frequency part that seems to destroy stability of the OABC when used together with higher order finite differences. The high-frequency part generally needs finer sampling in order for the stability criterion to be satisfied, and instability occurs specifically in connection with higher order finite differences. Of course, an obvious solution to this problem would be to replace the Ricker wavelet with a bandlimited wavelet.

Another aspect that should be emphasized is the use of a free surface in our applications. This leads to Rayleigh waves propagating with much smaller speeds and wavelengths than the P- and S-waves, which consequently may violate the stability criterion of the OABC. This problem is common with absorbing boundary conditions, and the effect becomes even more prominent in the case of free surface topography.

For reasons described, and particularly in order to be able to use realistic sources in connection with OABC, we developed the given optimal procedure of implementing OABC in our higher order finite-difference scheme. Following this procedure, instability is delayed until the most interesting wave phenomena have been synthesized.

Efficiency

In the first simulations the homogeneous medium model was used, using (1) the OABC (Figures 2 and 3) and (2) the ED (Figures 4 and 5). All plots were scaled according to the maximum value anywhere in the grid at each time step. If a permanent maximum value were used, reflections would be invisible. In Figure 2 the L_2-norm of the velocity vector is

---

displayed in a snapshot 11 s after a pressure wave has been initiated. Here, the P-wave front has just reached the bottom of the model. The snapshot reveals a weak P-P reflection from the bottom, while stronger artificial P-P and P-S reflections can be seen from both sidewalls. Interestingly, the reflections from the left sidewall are stronger than the ones from the right sidewall. The reason is our staggered grid description of Figure 1. Since we use the same number of grid points of each field variable in each grid dimension, a different set of variables generates the left and right grid edges (Figure 1). Specifically, the three (of totally five) variables δ_{xx}, δ_{zz} and w are absorbed further inside the grid on the right than on the left grid edge and explains the better absorption on the right edge (Figure 2). Figure 2 also shows a P-SV head-wave propagating from the upper left corner only. This is because the velocity analog of the stress-free surface conditions (Hestholm and Ruud, 1994) is implemented in an asymmetric way according to Figure 1.

In Figure 3 the velocity vector modulus (L_2-norm) is displayed in a snapshot 22 s after the pressure wave has been initiated. Predominantly artificial reflections can be identified here, since the dominant non-artificial wavefield has passed out of the model frame. The reflections from the S-wave are stronger than from the P-wave due to our choice of maximum P-wave absorption (Peng and Toksöz, 1994, 1995). The strongest reflections are seen to come from the bottom, while the vertically oriented wave front seen near the right boundary is the P-wave reflection from the left boundary.

Figures 4 and 5 are similar to Figures 2 and 3, except that ED was applied within 20 grid points wide strips along the numerical boundaries at the bottom and sides. Clearly, the ED scheme works better than the OABC in absorbing both P-waves and S-waves. It absorbs equally well along the bottom and the sidewalls. In Figure 5 the non-artificial waves have passed out of the model, and only artificial grid reflections remain. Investigating amplitude values at the layer adjacent to the grid edges, these reflections were found to be weaker than the corresponding reflections with the OABC by a factor of approximately 10^{-2}, and furthermore, the run is completely stable. Again, because of the staggering, a Rayleigh wave can be distinguished propagating along the surface on the right part of Figure 5, whereas the one on the left is too weak to be seen.

Application of lower order finite differences near boundaries introduces extra dispersion. This dispersion seems to be less well handled by the OABC than by the ED. The reason is probably that high frequencies are quickly attenuated by ED. Methods like ED (Cerjan et. al., 1985) are known to absorb reflections of relatively short wavelengths better than most methods. Because of this, we see that ED absorbs both the high-frequency part from the broadband source and the Rayleigh waves at the surface quite well. In our examples, the high-frequency part from the source seems especially problematic for the OABC to absorb. The problem may be partly due to unspecified behavior of the OABC when it is used to absorb frequency parts for which its stability criterion is not satisfied.

A homogeneous model is an oversimplification of the real Earth, and so further comparison between OABC and ED is tied to wavefield simulation using a multilayered crust - upper mantle model shown in Figure 6. Velocity vector modulii (amplitudes) as in Figures 2-5 are shown in Figures 7 and 8, but now using the background model of Figure 6. This fact, together with the multiple additional reflections from the various layer boundaries, cause these snapshots to be less clear than those for the homogeneous medium model (Figures 2-5). Figure 7 shows the wavefield 22 seconds after the pressure wave was initiated, using OABC. Also here asymmetric P-P and P-S reflections from the sidewalls can be seen, together with long term effects of wave conversions and reflections from the layers. The absorption at the bottom is seen to be somewhat better than that at the sidewalls due to the staggered grid.

Figure 8 shows the corresponding run using ED. The absorption strips of 20 grid points' width are clearly visible along the numerical boundaries. In comparing amplitudes at locations of artificial reflections from the last two runs we found them on the average $O(10)$ stronger from using OABC than from using ED.

Conclusions

While a naive implementation of the OABC in our 2-D finite-difference scheme resulted in instabilities, a simple modification of the original algorithm allowed us to delay them beyond the time of interest. We arrived at an optimal procedure for implementing Peng

and Toksöz's OABC algorithm, and then compared the OABC results with those obtained by using ED.

In implementing the OABC we found the choice of spatial finite-difference order to be important. With broadband Gaussian point source types the stability criterion of the OABC is not fulfilled for the complete frequency range, even though stable behavior is achieved by using 2nd and 4th order spatial finite differences throughout the grid. OABC always behaves unstably when using higher order spatial finite differences. The order of accuracy must be decreased when approaching the numerical boundaries in order to delay the instability. In our synthetic discretization scheme an 8th order accurate spatial finite-difference approximation is used in the interior of the grid. In moving from the interior towards the boundaries we found the following procedure to be optimal: 6 layers of 6th order finite differences, then 4 layers of 4th order and finally 2 layers of 2nd order adjacent to the numerical boundary. It seems clear that ED absorbs better than OABC. In a homo-geneous medium, the artificial reflection amplitudes from using ED within a thin strip were smaller by a factor 10^{-2} compared to using OABC. A reason might be insufficient sampling of higher frequencies near boundaries using OABC, and thereby violating its stability criterion for this frequency range. Another reason is the OABC's apparently smaller ability to handle dispersions arising from using lower order finite differences near boundaries. The mentioned drawback of additional computer storage are offset by the shorter simulation time using ED. In our 2-D applications we absorb at 13.2 % of the total number of grid points. In a 3-D application using the same grid as here with the second horizontal dimension length equal to the first, we would use 6.3 % of the grid points for absorption.

Acknowledgments

References

Cerjan, C., Kosloff, D., Kosloff, R. and Reshef, M., 1985, A nonreflecting boundary condition for discrete acoustic and elastic wave equations: Geophysics, **50**, 705-708.

Clayton, R. and Engquist, B., 1977, Absorbing boundary conditions for acoustic and elastic wave equations: Bull. Seism. Soc. Am., **67**, 1529-1540.

Emerman, S. H. and Stephen, R. A., 1983, Comment on absorbing boundary conditions for acoustic and elastic wave equations by R. Clayton and B. Engquist: Bull. Seism. Soc. Am., **73**, 661-665.

Hestholm, S. O. and Ruud, B. O., 1994, 2-D finite-difference elastic wave modelling including surface topography: Geoph. Prosp., **42**, 371-390.

Higdon, R. L., 1990, Radiation boundary conditions for elastic wave propagation: SIAM J. of Num. Analysis, **27**, 831-870.

Holberg, O., 1987, Computational aspects of the choice of operator and sampling interval of numerical differentiation in large--scale simulation of wave phenomena: Geoph. Prosp., **35**, 629-655.

Kindelan, M., Kamel, A. and Sguazzero, P., 1990, On the construction and efficiency of staggered numerical differentiators for the wave equation: Geophysics, **55**, 107-110.

Levander, A. R., 1988, Fourth-order finite difference P-SV seismograms: Geophysics, **53**, 1425-1436.

Mahrer, K. D., 1986, An empirical study of instability and improvement of absorbing boundary conditions for the elastic wave equation: Geophysics, **51**,1499-1501.

Peng, C. and Toksöz, M. N., 1994, An optimal absorbing boundary condition for finite difference modeling of acoustic and elastic wave propagation: J. Acoust. Soc. Am., **95**, 733-745.

Peng, C. and Toksöz, M. N., 1995, An optimal absorbing boundary condition for elastic wave modeling: Geophysics, **60**, 296-301.

Reynolds, A. C., 1978, Boundary conditions for the numerical solution of wave propagation problems: Geophysics, **43**, 1099-1110.

Virieux, J., 1986, P-SV wave propagation in heterogeneous media: velocity-stress finite-difference method: Geophysics, **51**, 889-901.

Figure Captions

FIG. 1. Schematic of staggered grid variable definition.

FIG. 2. Snapshot of the velocity vector amplitude at t=11 s after a pressure wave has been initiated from a Gaussian point source at depth 0.5 km below the surface. The medium is homogeneous and OABC is used.

FIG. 3. Snapshot of the velocity vector amplitude for the same situation as in Figure 2 at t=22 s.

FIG. 4. Snapshot of the velocity vector amplitude for the same situation as in Figure 2, but in this case ED is used.

FIG. 5. Snapshot of the velocity vector amplitude for the same situation as in Figure 4 at t=22s.

FIG. 6. Snapshot of the velocity vector amplitude at t=1.2 s after a pressure wave has been initiated from a Gaussian point source at depth 0.5 km below the surface. The source position and the background model of the layered medium are clearly visible. The maximum P-velocity is 8.18 km/s right below the Moho. The Moho is located at 35 km depth. The closest layer above the Moho represents a P-velocity of 6.9 km/s. The next layer is the maximum velocity layer in the crust with a P-velocity of 7.1 km/s. Just below the free plane surface there is the minimum velocity layer with a P-velocity of 6.6 km/s.

FIG. 7. Snapshot of the velocity vector amplitude at t=22 s after a pressure wave has been initiated from a Gaussian point source at depth 0.5 km below the surface. The medium model is layered (Figure 6) and OABC is used.

FIG. 8. Snapshot of the velocity vector amplitude for the same situation as in Figure 7, but in this case ED is used.
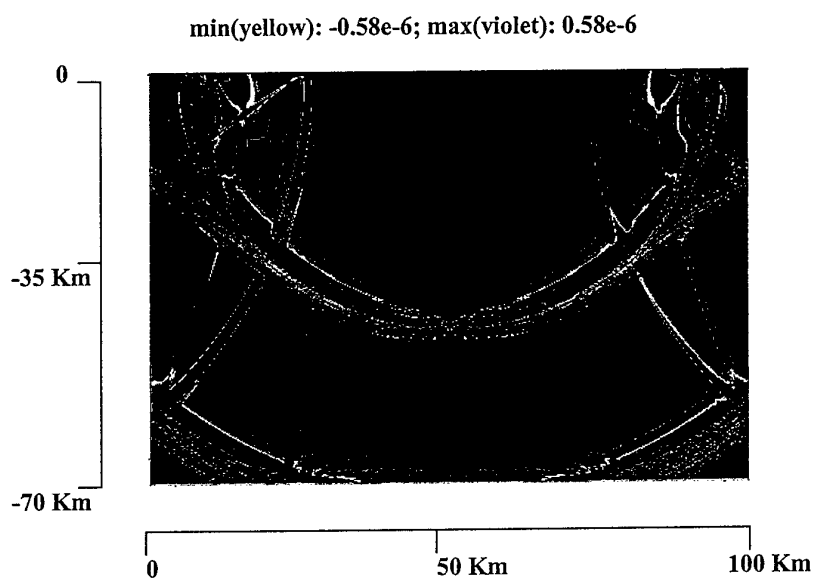
FIGURE 1.
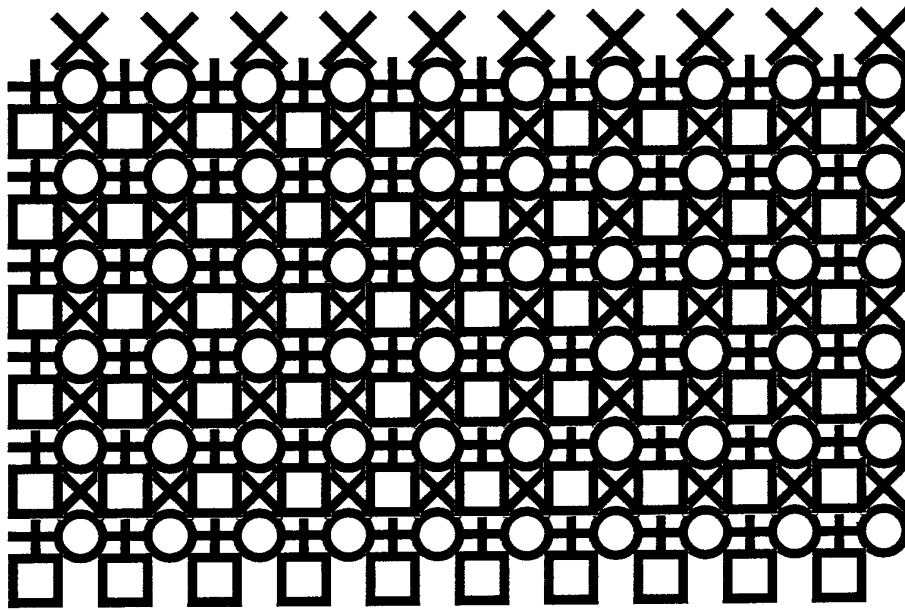
$\square$: diagonal stresses δ_{xx} and δ_{zz}

$\bigcirc$: non-diagonal stress δ_{zx}

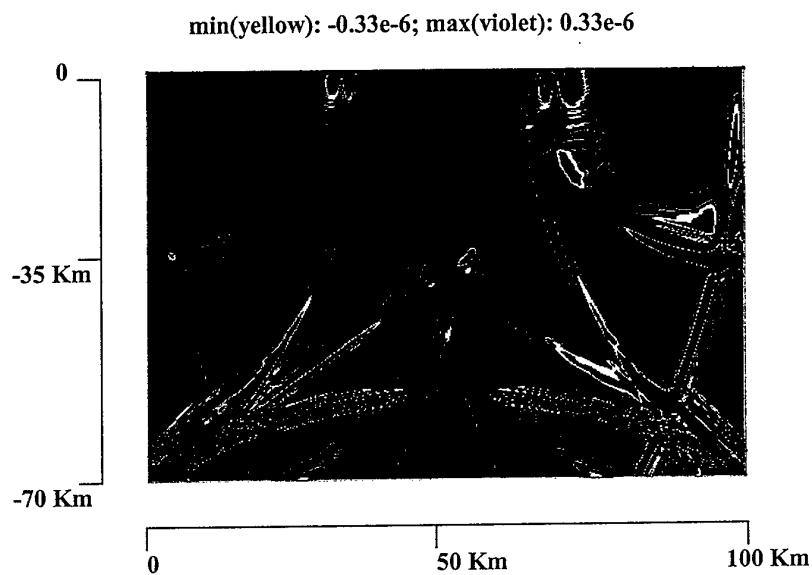$+$: vertical particle velocity w

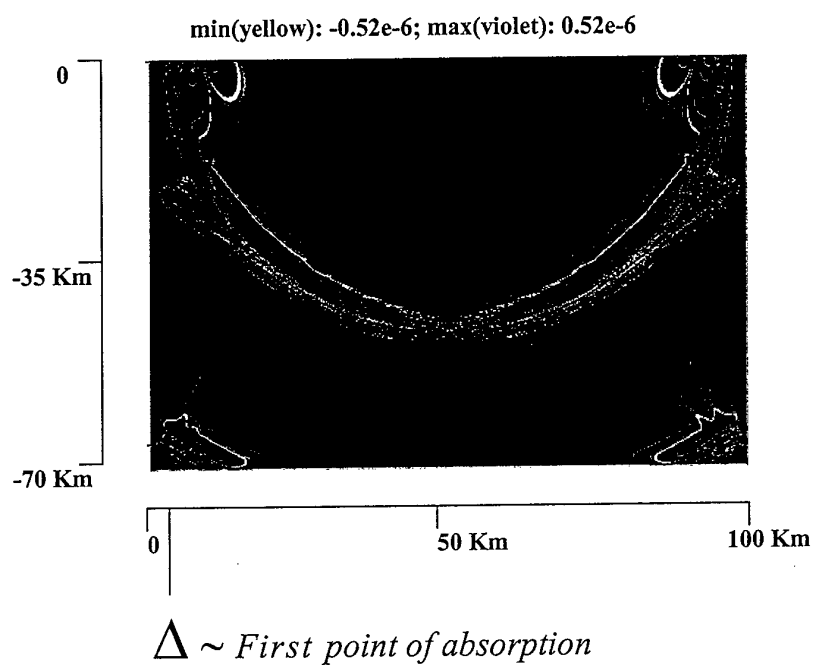$\times$: horizontal particle velocity u

Simone and Hestholm

Page width

FIGURE 2.

min(yellow): -0.58e-6; max(violet): 0.58e-6

Simone and Hestholm

Page width

FIGURE 3.

min(yellow): -0.33e-6; max(violet): 0.33e-6

Simone and Hestholm

Page width

FIGURE 4.

min(yellow): -0.52e-6; max(violet): 0.52e-6

Δ ~ *First point of absorption*

Simone and Hestholm

Page width

FIGURE 5.

min(yellow): -0.38e-8; max(violet): 0.38e-8

$\Delta \sim$ *First point of absorption*
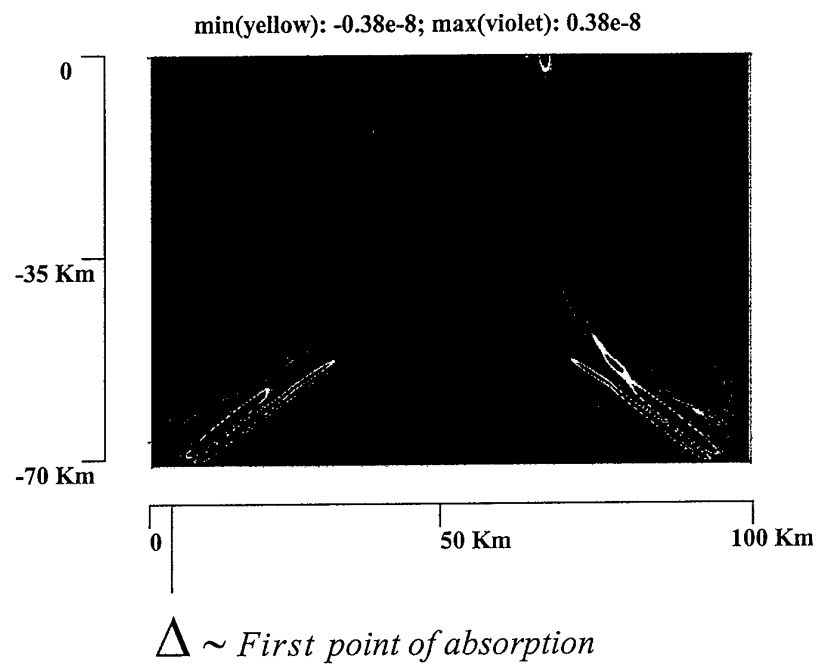
Simone and Hestholm

Page width

FIGURE 6.

Simone and Hestholm

Page width

FIGURE 7.

min(yellow): -0.51e-5; max(violet): 0.51e-5

Simone and Hestholm

Page width

FIGURE 8.

min (yellow); -0.68e-6; max(violet): 0.68e-6

Δ ~ *First point of absorption*
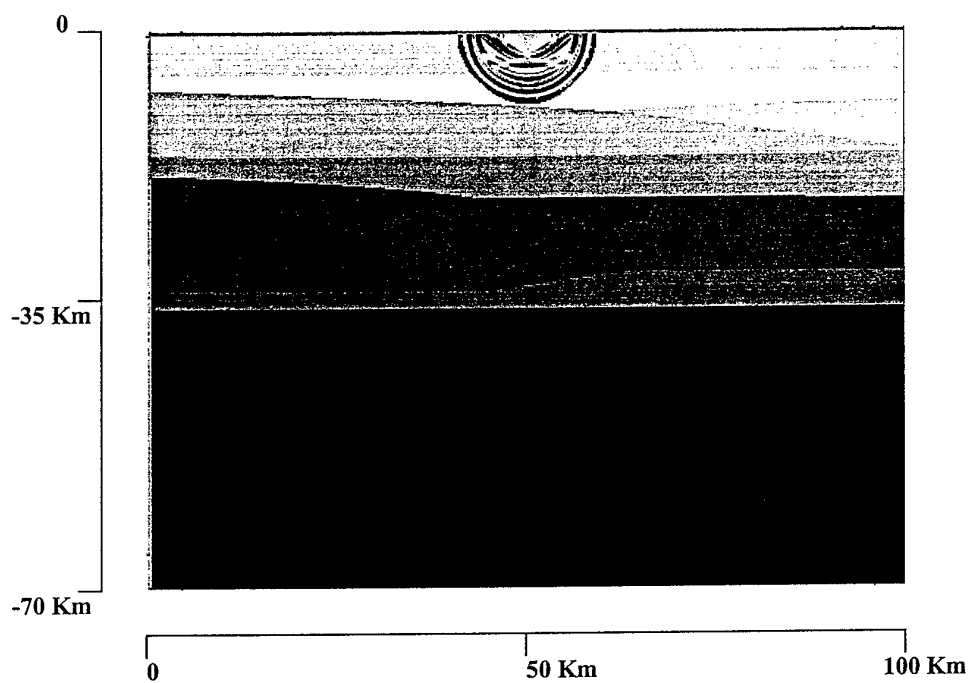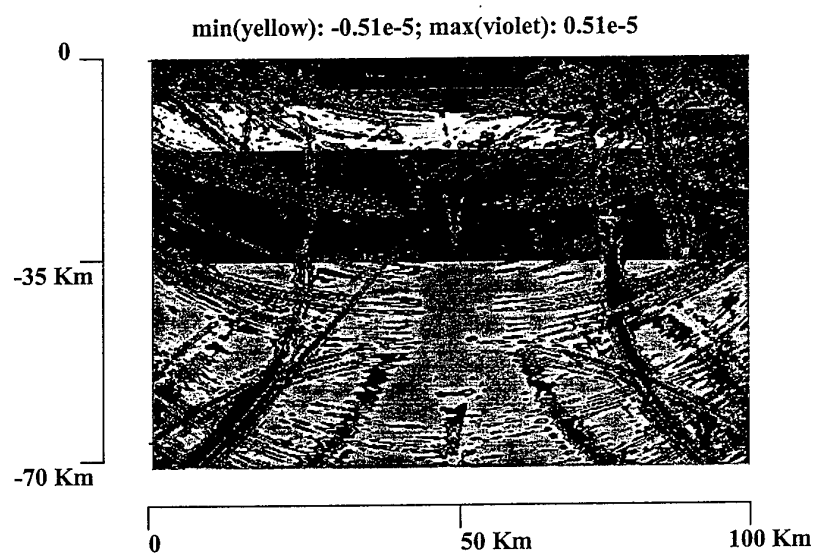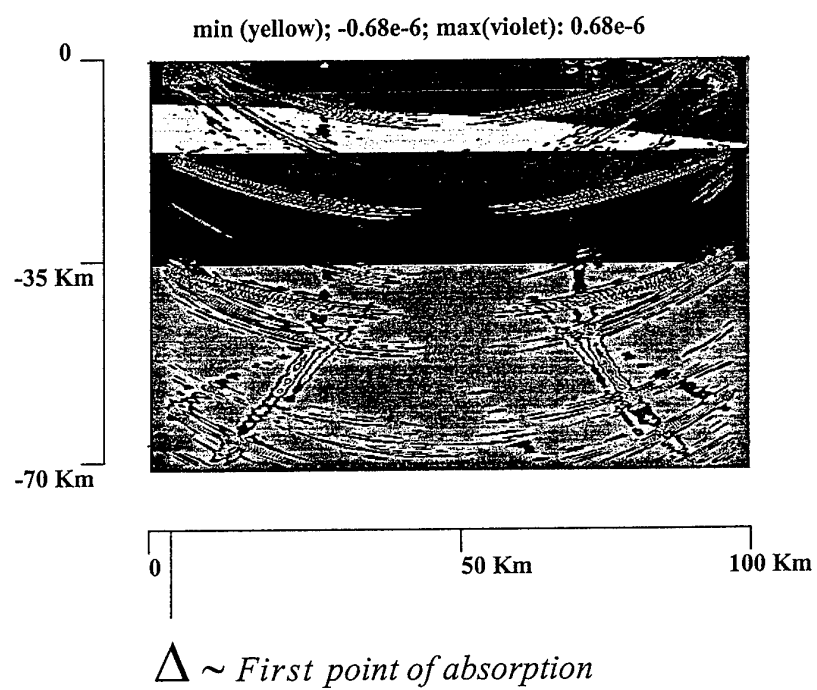
Simone and Hestholm

Page width

Appendix 6

3–D Finite Difference Elastic Wave Modeling

including Surface Topography

Stig Hestholm

Rice Univ., Dept. of Geology and Geophysics, 6100 Main, Houston, TX 77005–1892

Bent Ruud

Univ. of Bergen, Dept. of Solid Earth Physics, Allégt. 41, N–5008 Bergen, Norway

(January 29, 1997)

ABSTRACT

Three-dimensional (3–D) finite–difference (F–D) modeling of seismic scattering from free surface topography has been pursued. We have developed exact 3–D free surface topography boundary conditions for the particle velocities. A velocity–stress formulation of the full elastic wave equations together with the boundary conditions has been numerically modelled by an 8th order F–D method on a staggered grid. We give a numerical stability criterion for combining the boundary conditions with curved grid wave equations, where a curved grid represents the physical medium with topography. Implementation of this stability criterion stops instabilities from arising in areas of steep and rough topographies. We have simulated scattering from teleseismic P–waves using a plane, vertically incident wavefront and real topography from a 40 × 40 km area centered at the NORESS array of seismic receiver stations in south-eastern Norway. Synthetic snapshots and seismograms of the wavefield show clear conversion from P– to Rg– (short period fundamental mode Rayleigh) waves in an area of rough topography approximately 10 km east of NORESS. This result is consistent with numerous observations.

1

INTRODUCTION

The theory presented here is a direct extension from 2-D to 3-D of the corresponding theory in Hestholm and Ruud (1994). Inclusion of topography at the free surface of an elastic medium leads to improved modeling of near-surface scattering effects, especially those in the high frequency part of the wave field. Relatively little has been published on the modeling of free surface topography in 2-D and even less on the modeling of 3-D surface topography. This applies both to F-D methods and any other numerical discretization method. However, a work on this problem is that of Frankel and Leith (1992) who used an F-D scheme of fourth order accuracy in space and a density taper to zero starting at the height of the free surface while keeping the medium P-velocity unaltered. They achieved stable results by multiplying the crustal density by 0.4 for the locations one grid point above the free surface, by 0.16 for the locations two grid points above the free surface, and so on. In this manner they were able to obtain reasonable modeling results for free 3-D surface topography models.

More recently, Tessmer and Kosloff expanded their procedure for elastic wave modeling with free surface topography from 2-D to 3-D (Tessmer et al., 1992; Tessmer and Kosloff, 1994). They use a spectral discretization in space, being different in the horizontal and vertical directions. The velocity-stress formulation of the elastic wave equations is transformed into a curved grid. At the free surface, the stresses and velocities are transformed into a local system in which the vertical coordinate axis is normal to the surface element. The free surface conditions are then implemented by a 'characteristic' treatment of the velocity and stress components, before rotated back to the original system. In this method, both velocities and stresses are rotated into the local system at each point of the topography surface.

In the present work explicit 3-D boundary conditions for a free surface topography are derived. The basis is the vanishing stress condition for a free surface. As

in Tessmer and Kosloff (1994), a 3–D curved grid which is stretched in the vertical direction is adapted to the surface topography, i. e. the top surface of the grid coincides with the surface topography. A coordinate transform is then introduced for transferring the elastic, isotropic wave equations from the curved to a rectangular grid in which the numerical computations are done. At the topography surface, the velocity boundary conditions for a free surface are implemented into a local, rotated system at each point on the surface. Each of these systems has its vertical coordinate direction coinciding with the direction of the normal vector of the surface at the given point. The velocity boundary conditions are subsequently rotated back to the rectangular system. Once the boundary conditions are given in this system, the numerical discretization can be performed.

In the following paragraphs, the 3–D equivalents to the 2–D equations (Hestholm and Ruud, 1994) will be stated. In each instance, it is possible to verify coincidence between the 3–D and the 2–D case by eliminating the τ–direction (2nd coordinate direction of the computational grid) in 3–D. We can also verify the coincidence between the plane surface conditions in 3–D and the 3–D surface topography conditions applied to a plane surface. A description of the numerical discretization will be given and stability criteria for the method will be assessed. Then we present simulated scattering from teleseismic P–waves using a plane vertically incident wavefront and real topography from an area centered at the NORESS array in south-eastern Norway. Snapshots and synthetic seismograms of the wavefield will be shown, clearly displaying Rg waves in areas of rough topography. Finally, we look at future prospects for 3–D F–D modeling, particularly in light of the recent parallellization of the seismic code.

ELASTIC WAVE MODELING FORMULATION

The basic equations governing wave propagation in a continuous elastic medium are the equations of motion and the stress–strain relationship. The velocity–stress formulation (Achenbach, 1975; Virieux, 1986) can be written in 3–D as

$$\rho \frac{\partial u}{\partial t} = \frac{\partial \sigma_{xx}}{\partial x} + \frac{\partial \sigma_{xy}}{\partial y} + \frac{\partial \sigma_{xz}}{\partial z} + f_x, \tag{1}$$

$$\rho \frac{\partial v}{\partial t} = \frac{\partial \sigma_{xy}}{\partial x} + \frac{\partial \sigma_{yy}}{\partial y} + \frac{\partial \sigma_{yz}}{\partial z} + f_y, \tag{2}$$

$$\rho \frac{\partial w}{\partial t} = \frac{\partial \sigma_{xz}}{\partial x} + \frac{\partial \sigma_{yz}}{\partial y} + \frac{\partial \sigma_{zz}}{\partial z} + f_z, \tag{3}$$

$$\frac{\partial \sigma_{xx}}{\partial t} = \lambda \left(\frac{\partial u}{\partial x} + \frac{\partial v}{\partial y} + \frac{\partial w}{\partial z} \right) + 2\mu \frac{\partial u}{\partial x}, \tag{4}$$

$$\frac{\partial \sigma_{yy}}{\partial t} = \lambda \left(\frac{\partial u}{\partial x} + \frac{\partial v}{\partial y} + \frac{\partial w}{\partial z} \right) + 2\mu \frac{\partial v}{\partial y}, \tag{5}$$

$$\frac{\partial \sigma_{zz}}{\partial t} = \lambda \left(\frac{\partial u}{\partial x} + \frac{\partial v}{\partial y} + \frac{\partial w}{\partial z} \right) + 2\mu \frac{\partial w}{\partial z}, \tag{6}$$

$$\frac{\partial \sigma_{xy}}{\partial t} = \mu \left(\frac{\partial v}{\partial x} + \frac{\partial u}{\partial y} \right), \tag{7}$$

$$\frac{\partial \sigma_{xz}}{\partial t} = \mu \left(\frac{\partial w}{\partial x} + \frac{\partial u}{\partial z} \right), \tag{8}$$

$$\frac{\partial \sigma_{yz}}{\partial t} = \mu \left(\frac{\partial w}{\partial y} + \frac{\partial v}{\partial z} \right). \tag{9}$$

where ρ is the density and λ and μ are Lamé's parameters. f_x, f_y and f_z are the components of the body forces, u, v and w are the particle velocity components and σ_{xx}, σ_{yy}, σ_{zz}, σ_{xy}, σ_{xz} and σ_{yz} are the stress components.

We introduce a linear mapping from a rectangular (ξ, τ, η)–system (Figure 1) to a curved (x, y, z)–system (Figure 2), where both systems have positive direction upwards for the vertical coordinate. The 3–D mapping can be written as

$$x(\xi, \tau, \eta) = \xi, \tag{10}$$

$$y(\xi, \tau, \eta) = \tau, \tag{11}$$

$$z(\xi, \tau, \eta) = \frac{\eta}{\eta_{max}} z_0(\xi, \tau), \tag{12}$$

where $z_0(\xi, \tau)$ is the topography function, and the rectangular (ξ, τ, η)–system is limited by $\xi = 0$, $\xi = \xi_{max}$, $\tau = 0$, $\tau = \tau_{max}$, $\eta = 0$ and $\eta = \eta_{max}$. For the curved (x, y, z)–system the degree of stretching is proportional to the distance from the bottom plane of the system $(z = 0)$. From equations (10)–(12) we get, for a differentiable function $f(x, y, z)$,

$$\frac{\partial f}{\partial x} = \frac{\partial f}{\partial \xi} + \frac{\partial f}{\partial \eta}\frac{\partial \eta}{\partial x}, \tag{13}$$

$$\frac{\partial f}{\partial y} = \frac{\partial f}{\partial \tau} + \frac{\partial f}{\partial \eta}\frac{\partial \eta}{\partial y}, \tag{14}$$

$$\frac{\partial f}{\partial z} = \frac{\partial f}{\partial \eta}\frac{\partial \eta}{\partial z}, \tag{15}$$

Expressions for the partial derivatives, which are needed in the medium equations, are found from equations (10)–(12) (see Appendix A),

$$\frac{\partial \xi}{\partial x} = 1, \qquad \frac{\partial \xi}{\partial y} = 0, \qquad \frac{\partial \xi}{\partial z} = 0, \tag{16}$$

$$\frac{\partial \tau}{\partial x} = 0, \qquad \frac{\partial \tau}{\partial y} = 1, \qquad \frac{\partial \tau}{\partial z} = 0, \tag{17}$$

$$A(\xi, \tau, \eta) = \frac{\partial \eta}{\partial x} = -\frac{\eta}{z_0(\xi, \tau)}\frac{\partial z_0(\xi, \tau)}{\partial \xi}, \tag{18}$$

$$B(\xi, \tau, \eta) = \frac{\partial \eta}{\partial y} = -\frac{\eta}{z_0(\xi, \tau)}\frac{\partial z_0(\xi, \tau)}{\partial \tau}, \tag{19}$$

$$C(\xi, \tau) = \frac{\partial \eta}{\partial z} = \frac{\eta_{max}}{z_0(\xi, \tau)}. \tag{20}$$

The velocity–stress formulation of the equations of motion and Hooke's law is given in the curved (x, y, z)–grid by equations (1)–(9). Expanding these by the chain rule (Appendix B) as in Hestholm and Ruud (1994), we get the medium equations in the rectangular (ξ, τ, η)–system,

$$\rho\frac{\partial u}{\partial t} = \frac{\partial \sigma_{xx}}{\partial \xi} + A(\xi, \tau, \eta)\frac{\partial \sigma_{xx}}{\partial \eta} + \frac{\partial \sigma_{xy}}{\partial \tau} + B(\xi, \tau, \eta)\frac{\partial \sigma_{xy}}{\partial \eta} + C(\xi, \tau)\frac{\partial \sigma_{xz}}{\partial \eta} + f_x, \tag{21}$$

$$\rho\frac{\partial v}{\partial t} = \frac{\partial \sigma_{xy}}{\partial \xi} + A(\xi, \tau, \eta)\frac{\partial \sigma_{xy}}{\partial \eta} + \frac{\partial \sigma_{yy}}{\partial \tau} + B(\xi, \tau, \eta)\frac{\partial \sigma_{yy}}{\partial \eta} + C(\xi, \tau)\frac{\partial \sigma_{yz}}{\partial \eta} + f_y, \tag{22}$$

$$\rho\frac{\partial w}{\partial t} = \frac{\partial \sigma_{xz}}{\partial \xi} + A(\xi, \tau, \eta)\frac{\partial \sigma_{xz}}{\partial \eta} + \frac{\partial \sigma_{yz}}{\partial \tau} + B(\xi, \tau, \eta)\frac{\partial \sigma_{yz}}{\partial \eta} + C(\xi, \tau)\frac{\partial \sigma_{zz}}{\partial \eta} + f_z, \tag{23}$$

$$\frac{\partial \sigma_{xx}}{\partial t} = (\lambda + 2\mu)\left(\frac{\partial u}{\partial \xi} + A(\xi, \tau, \eta)\frac{\partial u}{\partial \eta}\right) + \lambda\left(\frac{\partial v}{\partial \tau} + B(\xi, \tau, \eta)\frac{\partial v}{\partial \eta} + C(\xi, \tau)\frac{\partial w}{\partial \eta}\right), \tag{24}$$

5

$$\frac{\partial \sigma_{yy}}{\partial t} = \lambda \left(\frac{\partial u}{\partial \xi} + A(\xi, \tau, \eta) \frac{\partial u}{\partial \eta} + C(\xi, \tau) \frac{\partial w}{\partial \eta} \right) + (\lambda + 2\mu) \left(\frac{\partial v}{\partial \tau} + B(\xi, \tau, \eta) \frac{\partial v}{\partial \eta} \right), \quad (25)$$

$$\frac{\partial \sigma_{zz}}{\partial t} = \lambda \left(\frac{\partial u}{\partial \xi} + A(\xi, \tau, \eta) \frac{\partial u}{\partial \eta} + \frac{\partial v}{\partial \tau} + B(\xi, \tau, \eta) \frac{\partial v}{\partial \eta} \right) + (\lambda + 2\mu) C(\xi, \tau) \frac{\partial w}{\partial \eta}, \quad (26)$$

$$\frac{\partial \sigma_{xy}}{\partial t} = \mu \left(\frac{\partial v}{\partial \xi} + A(\xi, \tau, \eta) \frac{\partial v}{\partial \eta} + \frac{\partial u}{\partial \tau} + B(\xi, \tau, \eta) \frac{\partial u}{\partial \eta} \right), \quad (27)$$

$$\frac{\partial \sigma_{xz}}{\partial t} = \mu \left(\frac{\partial w}{\partial \xi} + A(\xi, \tau, \eta) \frac{\partial w}{\partial \eta} + C(\xi, \tau) \frac{\partial u}{\partial \eta} \right), \quad (28)$$

$$\frac{\partial \sigma_{yz}}{\partial t} = \mu \left(\frac{\partial w}{\partial \tau} + B(\xi, \tau, \eta) \frac{\partial w}{\partial \eta} + C(\xi, \tau) \frac{\partial v}{\partial \eta} \right), \quad (29)$$

Equations (21)–(29) are the momentum conservation equations and Hooke's law given in the rectangular (ξ, τ, η)–system.

FREE SURFACE BOUNDARY CONDITIONS

The 3–D free boundary conditions for the velocities at a locally horizontal surface (or in a system where the z–axis is parallell to the local normal vector of the surface) resulting from the vanishing stress condition can be written

$$\frac{\partial u}{\partial z} = -\frac{\partial w}{\partial x}, \quad (30)$$

$$\frac{\partial v}{\partial z} = -\frac{\partial w}{\partial y}, \quad (31)$$

$$\frac{\partial w}{\partial z} = -\frac{\lambda}{\lambda + 2\mu} \left(\frac{\partial u}{\partial x} + \frac{\partial v}{\partial y} \right), \quad (32)$$

with x and y the horizontal coordinates and z the vertical coordinate. We want to apply these conditions to a topography surface. At each surface point, we introduce a local coordinate system (x', y', z') in which the z'–axis coincides with the local normal vector direction of the surface. In this local system we impose the conditions (30)–(32). Once this is done, they have to be rotated back to the rectangular system (ξ, τ, η) where the numerical computations can be done. This rotation is expressed by

$$\vec{v} = \mathbf{A} \vec{v}\,', \quad (33)$$

6

where $\vec{v}$ and $\vec{v}\,'$ are the particle velocity vectors in the (ξ, τ, η)– and the (x', y', z')–systems respectively. $\mathbf{A}$ is the rotation matrix, which can be given by

$$\mathbf{A} = \begin{pmatrix} \cos\theta & 0 & \sin\theta \\ -\sin\theta\sin\phi & \cos\phi & \cos\theta\sin\phi \\ -\sin\theta\cos\phi & -\sin\phi & \cos\theta\cos\phi \end{pmatrix}. \tag{34}$$

where θ is the rotation angle between the ξ–axis and the local x'–axis in the (ξ, η)–plane and ϕ is the rotation angle between the τ–axis and the local y'–axis in the local (y', z')–plane. We also have the relations $\tan\theta = \partial z_0(\xi, \tau)/\partial\xi$ and $\tan\phi = \partial z_0(\xi, \tau)/\partial\tau \cos\theta$ (see Appendix C).

Now the calculations of the rotation from the local (x', y', z')–system back to the (ξ, τ, η)–system can be performed as in Appendix C. We arrive at the 3–D boundary conditions for free surface topography given in the computational (ξ, τ, η)–system by

$$\left(\frac{d^2}{q} + 1\right)\frac{\partial u}{\partial\eta} = d\left(1 - \frac{1}{q}\right)\frac{\partial u}{\partial\xi} - \left(d^2 r + p\right)\frac{\partial v}{\partial\xi} - \left(d^2 q + 1\right)\frac{\partial w}{\partial\xi} + \frac{p}{e}\frac{\partial u}{\partial\tau}$$
$$- \frac{dpr}{e}\frac{\partial v}{\partial\tau} - \frac{dr}{e}\frac{\partial w}{\partial\tau} + d\left(r - p\right)\frac{\partial v}{\partial\eta} + d\left(q - 1\right)\frac{\partial w}{\partial\eta}, \tag{35}$$

$$\left(ep^2 + 1\right)\frac{\partial v}{\partial\eta} = \frac{dfp}{q}\frac{\partial u}{\partial\xi} + \left(d + fp^2\right)\frac{\partial v}{\partial\xi} + p\left(f - d\right)\frac{\partial w}{\partial\xi} - \frac{d}{q}\frac{\partial u}{\partial\tau}$$
$$+ p\left(\frac{1}{e} - 1\right)\frac{\partial v}{\partial\tau} - \left(\frac{p^2}{e} + 1\right)\frac{\partial w}{\partial\tau} - \frac{fp}{q}\frac{\partial u}{\partial\eta}$$
$$+ p\left(1 - e\right)\frac{\partial w}{\partial\eta}, \tag{36}$$

$$\left(\zeta\left[\frac{d^2}{q} + \frac{p^2}{e}\right] - 1\right)\frac{\partial w}{\partial\eta} = \frac{1}{q}\left(\frac{\zeta}{q} - d^2\right)\frac{\partial u}{\partial\xi} - dp\left(\zeta\left[\frac{1}{q} + \frac{1}{e}\right] + 1\right)\frac{\partial v}{\partial\xi}$$
$$+ d\left(\zeta\left[\frac{p^2}{e} - \frac{1}{q}\right] - 1\right)\frac{\partial w}{\partial\xi} - \frac{dp}{eq}\frac{\partial u}{\partial\tau} + \frac{1}{e}\left(\frac{\zeta}{e} - p^2\right)\frac{\partial v}{\partial\tau}$$
$$- \frac{p}{e}\left(\frac{\zeta}{e} + 1\right)\frac{\partial w}{\partial\tau} + \frac{d}{q}\left(\frac{\zeta}{q} + 1\right)\frac{\partial u}{\partial\eta}$$
$$+ p\left(\zeta\left[\frac{1}{e} - \frac{d^2}{q}\right] + 1\right)\frac{\partial v}{\partial\eta}, \tag{37}$$

with

$$\zeta = \frac{\lambda}{\lambda + 2\mu}, \tag{38}$$

7

$$d = \frac{\partial z_0(\xi, \tau)}{\partial \xi}, \tag{39}$$

$$e = \cos\left[\arctan\left(d\right)\right], \tag{40}$$

$$f = \sin\left[\arctan\left(d\right)\right], \tag{41}$$

$$p = \frac{\partial z_0(\xi, \tau)}{\partial \tau}e, \tag{42}$$

$$q = \cos\left[\arctan\left(p\right)\right], \tag{43}$$

$$r = \sin\left[\arctan\left(p\right)\right]. \tag{44}$$

Equations (35)–(44) are exact 3–D boundary conditions for an arbitrary, smooth, free surface topography. They result from rotating the velocity free surface conditions from local systems at each point of the surface topography into a rectangular system (Appendix C). The vertical axis in each of the local systems is normal to the local topography. Also, the boundary conditions (35)–(44) are obviously not restricted to the F–D method or any other numerical discretization technique.

NUMERICAL DISCRETIZATION

For the numerical discretization, we refer to the corresponding paragraph in Hestholm and Ruud (1994). The same spatial and time discretization methods as in the 2–D case (Kindelan et al., 1990) are used. The schemes employ a staggered discretization stencil as in Levander (1988) of the velocity–stress formulation of the elastodynamic wave equations, which is again based on the work of Virieux (1986). An advantage of using a staggered definition of variables is that we can avoid explicit definition of the stresses at the surface topography as it suffices to define the velocities there. In order to get the velocities and stresses explicitly defined at each time step, we have to stagger the vertical velocity component w one half grid length downwards. Corresponding numerical definitions of the other variables have to be implemented. Generally, u is staggered one half grid length in the positive ξ–direction, v is staggered one half grid length in the positive τ–direction, while w is staggered

8

one half grid length in the negative η–direction (downwards). The 3–D boundary conditions, equations (35)–(37) are discretized by 2nd order, staggered F–D operators (Fornberg, 1988). Below the free surface, the central, staggered F–D method's order is gradually increased with depth, via 4th and 6th up to 8th order, the latter is the order used inside the domain. This 8th order method is dispersion–bounded and cost–optimized (Kindelan et al., 1990). Along the artificial grid boundaries exponential damping according to Cerjan et al. (1985) is used. In a layer of 20 points along each grid boundary, the stresses and velocities are multiplied by exponentially decreasing terms towards the boundary.

To find the velocity components at the surface topography from the closed system (35)–(37), we solve it directly as a linear system with respect to the velocities at the surface as they are defined in the vertical derivative discretizations. In this procedure, the horizontal derivatives are defined half a grid length below the free surface, and the derivatives are discretized by 2nd order finite differences.

STABILITY CRITERION FOR THE SURFACE TOPOGRAPHY MODELING

A numerical stability criterion for the surface topography modeling comes from the equations of motion in the medium. A necessary condition to keep a run stable is that the absolute values of the parameters $A(\xi, \tau, \eta)$, $B(\xi, \tau, \eta)$ and $C(\xi, \tau)$ all be kept less than 1. This necessary condition can be written as

$$\frac{z_0(\xi, \tau)}{\eta_{max}} > \max \begin{cases} 1, \\ \|\partial z_0(\xi, \tau)/\partial \xi\|, \\ \|\partial z_0(\xi, \tau)/\partial \tau\|, \end{cases}$$

where η_{max} is the total depth of the numerical (ξ, τ, η)–grid and $\partial z_0(\xi, \tau)/\partial \xi$ and $\partial z_0(\xi, \tau)/\partial \tau$ are topography slopes. This condition must be satisfied at every point on the surface. Note that this condition can always be satisfied, if necessary, by

uniformly increasing $z_0(\xi, \tau)$ everywhere. Equivalently, η_{max} can be decreased to satisfy the inequality.

For some combinations of sources and reliefs, this condition might not be sufficient to avoid an unstable growth right below the surface at the steepest parts of the topography. In these cases, η_{max} should be reduced enough for stability to be maintained. By decreasing η_{max} rather than increasing $z_0(\xi, \tau)$ uniformly, the original physical model (represented by the curved grid) is conserved. It is a matter of experimentation, then, how much η_{max} must be reduced in order to make wavefield simulations stable for a specific relief. The number of vertical samples must be the same in the curved and rectangular systems. This means that in order to maintain accuracy and simultaneously retain stability gained from increased curved to rectangular grid depth ratio, the vertical grid distance (vertical distance between grid points) in the numerical (ξ, τ, η)–system must be reduced by an appropriate factor.

For most sources/topography constellations, it turns out that $min\{(z_0(\xi, \tau)\} \approx 3\eta_{max}$ is enough for a simulation to be stable. Therefore, this criterion might be stated as a sufficient condition for stability in most cases. From our experiments, this order of magnitude for the ratio between the physical model and the numerical grid depth appears necessary whenever the topography data exhibits rough behaviour (large spatial second derivatives) near its steepest slopes. For rough topography without large spatial derivatives or steep topography without large second derivatives, this ratio may be smaller in order to achieve stability. In many such cases the stated necessary stability condition is also sufficient.

P– TO RG–SCATTERING FROM TOPOGRAPHIC RELIEF

Since 3–D topography surfaces in general, and real reliefs in particular, are seldom used in detailed wavefield modeling, we hope that the above approach should constitute a powerful method for the F–D elastic wave modeling including surface

topography. The main goal of the research performed is to improve our understanding of wave propagation and scattering phenomena for local and regional distance travel paths. An interesting case here is observationally well documented. Scattering of teleseismic P–wave energy into Rg have been extensively studied using data from the 3 km aperture NORESS array in south–eastern Norway (Bannister et al., 1990; Gupta et al., 1993; Hedlin et al., 1991; Hedlin et al., 1994). For our 3–D F–D simulation of this phenomenon we have obtained digital elevation data for an area of 100 × 100 km centered on the NORESS array (Figure 3). Due to the huge computer memory requirements of 3–D F–D methods, we have so far been restricted to a model of size 40 × 40 × 35 km with 0.2 km sampling. However, this situation is now improved by parallellization of our code. In all the examples shown the incoming wave is a vertically incident plane P–wave simulating a teleseismic short period P–phase. The center frequency of the Ricker wavelet is 2.5 Hz, the P–wave velocity of the homogeneous medium is 6.0 km/s and the Poisson ratio is 0.25.

In our present experiment the elevations were multiplied by 0.5 so that topography undulations were damped. By doing this the magnitudes of $A(\xi, \tau, \eta)$ and $B(\xi, \tau, \eta)$ were reduced so as to achieve stable results without the need of increasing the model depth beyond the depth of the numerical grid. Alternatively, the numerical grid depth could have been reduced or the model grid depth could have been increased by some factor. Snapshots of the wavefield (vertical component of the particle velocity) are shown in Figure 4. A dominant feature here is the low–frequency/long–wavelength artificial reflections from the absorbing model boundaries. Although the exponential damping technique is the most efficient absorbing boundary method we have tested, a wave incident at an angle of 90° with the boundary is the most difficult case. Fortunately, the artificial reflections are frequency dependent, with longer wavelengths than most of the surface waves scattered by the topography, and can therefore be removed by filtering and image processing techniques. As seen from Figure 4 the scattered surface waves appear to radiate out from secondary point sources which

coincide with areas of high topographic gradients (Figure 3). The dominant scattering points are along the steep valley side east of 'Bronkeberget' about 10 km east of NORESS (Bannister et al., 1990). Also in seismograms from the west–east profile P–to–Rg scattering from this area is clearly seen (Figure 5).

In order to quantify and locate areas of significant topographic features, we have computed different functions depending on first and second order derivatives of the topography function $z = z_0(x, y)$. First, we computed the slope, i.e., the length of the topography gradient vector as

$$|\nabla z_0(x, y)| = \left[\left(\frac{\partial z_0}{\partial x} \right)^2 + \left(\frac{\partial z_0}{\partial y} \right)^2 \right]^{1/2} \tag{45}$$

This vector is useful for defining areas of strong scattering. Additionally, smooth topography is assumed in deduction of the boundary conditions. As a measure for topography roughness, we compute the Frobenius norm of the Hessian matrix of $z_0(x, y)$, i.e.,

$$\|H(x, y)\|_F = \left[\left(\frac{\partial^2 z_0}{\partial x^2} \right)^2 + \left(\frac{\partial^2 z_0}{\partial x \partial y} \right)^2 + \left(\frac{\partial^2 z_0}{\partial y \partial x} \right)^2 + \left(\frac{\partial^2 z_0}{\partial y^2} \right)^2 \right]^{1/2} \tag{46}$$

Both these functions have their largest values in the areas of strongest scattering (Figure 6).

Recently, we modified the code to run on parallel computers. The tool used for parallellization was MPI (Message Passing Interface), which is the first attempt of standardization to some degree of parallel programming tools. Besides speeding up computations, the parallellization also allows us to use a larger computer memory, which is essential for realistic seismic wavefield simulation. Test runs employing up to 2GBytes of memory have been performed. For a simulation of this size we used 48 hours on 48 processors on the Intel Paragon machine at the Univ. of Bergen, Norway. Increasing the number of processors to 80, which is the maximum possible number of processors on the machine's batch queue, the simulation time was reduced to a little more than 6 hours, i. e. a speed-up factor of 8. The main reason for the significant

12

speed-up in the latter case is that the complete 2GB of memory was distributed over real memory on the processors, so that no virtual memory had to be used, and thus paging to and from disk was avoided.

DISCUSSION AND CONCLUSIONS

Even for small scale experiments 3–D F–D synthetic wavefield analysis provides, as demonstrated here, improved insight and a better understanding of surface scattering phenomena. We find it particularly gratifying that the strong P–to–Rg scattering from the Bronkeberget hill, observed by Bannister et al. (1990) through analysis of NORESS recordings, can be realistically synthesized. Another interesting feature is that for certain spatial low–frequency variants of the local NORESS topography the Rg–wave propagation seems to change abruptly over relatively small distances. Probably, this is due to strong directionality dependence of the scattering from some topographic features. Such wavefield characteristics are sometimes observed in NORESS recordings and at the German array GERESS located in the Bavarian hills – at some sensors the Rg–phase is prominent while hardly visible at nearby sensors less than a kilometer away. In other words, also small scale crustal features may contribute to blocking effects as often observed for Rg– and Lg–phases across structural obstacles. Many of such wavefield phenomena are out of range for 2–D F–D synthetic experiments; hence our emphasis on continuous research efforts on 3–D synthetic simulation of crustal wave field propagation.

Future directions of our research will be to increase the model size to also include the scattering areas south–east of Lake Mjøsa (Bannister et al., 1990). Furthermore, in order to compare directly with NORESS recordings it is necessary to allow for non–vertical incident waves and to use source time functions derived from teleseismic P–beams. We also plan to implement the topography boundary conditions into 2–D and 3–D viscoelastic schemes. This will be done in order to be able to simulate a

realistic attenuation of waves, in particular the strong waves generated from areas of significant surface topography. In addition, this will greatly improve the absorbing boundary conditions. Although the physical dimensions of 3–D models used in simulation will still be relatively small compared to 2–D models employed, the use of parallel computer technology opens new avenues to the study of 3–D scattering phenomena in fields like random media and corrugated interface scattering.

ACKNOWLEDGMENTS

REFERENCES

Achenbach, J. D., 1975, Wave propagation in elastic solids: North–Holland Publishing Co.

Bannister, S. C., Husebye, E. S., and Ruud, B. O., 1990, Teleseismic p–coda analyzed by three-component and array techniques – deterministic location of topographic p–to–rg scattering near the noress array: Bull. Seism. Soc. Am., **80**, 1969–1986.

Cerjan, C., Kosloff, D., Kosloff, R., and Reshef, M., 1985, Short note on a nonreflecting boundary condition for discrete acoustic–wave and elastic–wave equations: Geophysics, **50**, 705–708.

Fornberg, B., 1988, Generation of finite difference formulas on arbitrary spaced grids: Mathematics of Computation, **51**, 699–706.

Frankel, A., and Leith, W., 1992, Evaluation of topographic effects on p and s–waves of explosions at the northern novaya zemlya test site using 3–d numerical simulations: Geoph. Res. Lett., **19**, 1887–1890.

Gupta, I. N., Lynnes, C. S., and Wagner, R. A., 1993, An array study of the effects of known local scatterers on regional phases: Bull. Seism. Soc. Am., **83**, 53–63.

Hedlin, M. A., Minster, J. B., and Orcutt, J. A., 1991, Beam-stack imaging using a small aperture array: Geoph. Res. Lett., **18**, 1771–1774.

Hedlin, M. A., Minster, J. B., and Orcutt, J. A., 1994, Resolution of prominent crustal scatterers near the noress small-aperture array: Geoph. J. Int., **119**, 101–115.

Hestholm, S. O., and Ruud, B. O., 1994, 2d finite difference elastic wave modeling including surface topography: Geoph. Prosp., **42**, 371–390.

Kindelan, M., Kamel, A., and Sguazzero, P., 1990, On the construction and efficiency of staggered numerical differentiators for the wave equation: Geophysics, **55**, 107–110.

Levander, A. R., 1988, Fourth–order finite–difference p–sv seismograms: Geophysics, **53**, 1425–1436.

Tessmer, E., and Kosloff, D., 1994, 3–d elastic modeling with surface topography by a chebychev spectral method: Geophysics, **59**, 464–473.

Tessmer, E., Kosloff, D., and Behle, A., 1992, Elastic wave propagation simulation in the presence of surface topography: Geoph. J. Int., **108**, 621–632.

Virieux, J., 1986, P-sv wave propagation in heterogeneous media: velocity–stress finite–difference method: Geophysics, **51**, 889–901.

APPENDIX A–PARTIAL DERIVATIVES IN MEDIUM EQUATIONS

For the medium equations we need $\partial\eta/\partial x$, $\partial\eta/\partial y$ and $\partial\eta/\partial z$. They are found from

$$\frac{\partial x}{\partial \xi}\frac{\partial \xi}{\partial x} + \frac{\partial x}{\partial \tau}\frac{\partial \tau}{\partial x} + \frac{\partial x}{\partial \eta}\frac{\partial \eta}{\partial x} = 1, \tag{A-1}$$

$$\frac{\partial y}{\partial \xi}\frac{\partial \xi}{\partial x} + \frac{\partial y}{\partial \tau}\frac{\partial \tau}{\partial x} + \frac{\partial y}{\partial \eta}\frac{\partial \eta}{\partial x} = 0, \tag{A-2}$$

$$\frac{\partial z}{\partial \xi}\frac{\partial \xi}{\partial x} + \frac{\partial z}{\partial \tau}\frac{\partial \tau}{\partial x} + \frac{\partial z}{\partial \eta}\frac{\partial \eta}{\partial x} = 0, \tag{A-3}$$

$$\frac{\partial x}{\partial \xi}\frac{\partial \xi}{\partial y} + \frac{\partial x}{\partial \tau}\frac{\partial \tau}{\partial y} + \frac{\partial x}{\partial \eta}\frac{\partial \eta}{\partial y} = 0, \tag{A-4}$$

$$\frac{\partial y}{\partial \xi}\frac{\partial \xi}{\partial y} + \frac{\partial y}{\partial \tau}\frac{\partial \tau}{\partial y} + \frac{\partial y}{\partial \eta}\frac{\partial \eta}{\partial y} = 1, \tag{A-5}$$

$$\frac{\partial z}{\partial \xi}\frac{\partial \xi}{\partial y} + \frac{\partial z}{\partial \tau}\frac{\partial \tau}{\partial y} + \frac{\partial z}{\partial \eta}\frac{\partial \eta}{\partial y} = 0, \tag{A-6}$$

$$\frac{\partial x}{\partial \xi}\frac{\partial \xi}{\partial z} + \frac{\partial x}{\partial \tau}\frac{\partial \tau}{\partial z} + \frac{\partial x}{\partial \eta}\frac{\partial \eta}{\partial z} = 0, \tag{A-7}$$

$$\frac{\partial y}{\partial \xi}\frac{\partial \xi}{\partial z} + \frac{\partial y}{\partial \tau}\frac{\partial \tau}{\partial z} + \frac{\partial y}{\partial \eta}\frac{\partial \eta}{\partial z} = 0, \tag{A-8}$$

$$\frac{\partial z}{\partial \xi}\frac{\partial \xi}{\partial z} + \frac{\partial z}{\partial \tau}\frac{\partial \tau}{\partial z} + \frac{\partial z}{\partial \eta}\frac{\partial \eta}{\partial z} = 1. \tag{A-9}$$

This leads to

$$\frac{\partial \eta}{\partial x} = \left(\frac{\partial y}{\partial \xi}\frac{\partial z}{\partial \tau} - \frac{\partial z}{\partial \xi}\frac{\partial y}{\partial \tau}\right)/J, \tag{A-10}$$

$$\frac{\partial \eta}{\partial y} = \left(\frac{\partial z}{\partial \xi}\frac{\partial x}{\partial \tau} - \frac{\partial x}{\partial \xi}\frac{\partial z}{\partial \tau}\right)/J, \tag{A-11}$$

$$\frac{\partial \eta}{\partial z} = \left(\frac{\partial x}{\partial \xi}\frac{\partial y}{\partial \tau} - \frac{\partial y}{\partial \xi}\frac{\partial x}{\partial \tau}\right)/J, \tag{A-12}$$

where

$$J = \frac{\partial x}{\partial \xi}\left(\frac{\partial y}{\partial \tau}\frac{\partial z}{\partial \eta} - \frac{\partial z}{\partial \tau}\frac{\partial y}{\partial \eta}\right) - \frac{\partial x}{\partial \tau}\left(\frac{\partial y}{\partial \xi}\frac{\partial z}{\partial \eta} - \frac{\partial y}{\partial \eta}\frac{\partial z}{\partial \xi}\right) + \frac{\partial x}{\partial \eta}\left(\frac{\partial y}{\partial \xi}\frac{\partial z}{\partial \tau} - \frac{\partial z}{\partial \xi}\frac{\partial y}{\partial \tau}\right). \tag{A-13}$$

With our choice of mapping functions, equations (10)–(12), we get

$$\frac{\partial x}{\partial \xi} = 1, \qquad \frac{\partial x}{\partial \tau} = 0, \qquad \frac{\partial x}{\partial \eta} = 0, \qquad \text{(A-14)}$$

$$\frac{\partial y}{\partial \xi} = 0, \qquad \frac{\partial y}{\partial \tau} = 1, \qquad \frac{\partial y}{\partial \eta} = 0, \qquad \text{(A-15)}$$

$$\frac{\partial z}{\partial \xi} = \frac{\eta}{\eta_{max}} \frac{\partial z_0(\xi, \tau)}{\partial \xi}, \qquad \frac{\partial z}{\partial \tau} = \frac{\eta}{\eta_{max}} \frac{\partial z_0(\xi, \tau)}{\partial \tau}, \qquad \frac{\partial z}{\partial \eta} = \frac{z_0(\xi, \tau)}{\eta_{max}} \qquad \text{(A-16)}$$

and

$$J = \frac{\partial z}{\partial \eta} = \frac{z_0(\xi, \tau)}{\eta_{max}}. \qquad \text{(A-17)}$$

From this we get the expressions (16)–(20).

18

APPENDIX B–MEDIUM EQUATIONS

Applying the chain rule to equations (1)–(9) and using the properties of equations (13)–(15) leads to

$$\rho \frac{\partial u}{\partial t} = \frac{\partial \sigma_{xx}}{\partial \xi} + \frac{\partial \sigma_{xx}}{\partial \eta}\frac{\partial \eta}{\partial x} + \frac{\partial \sigma_{xy}}{\partial \tau} + \frac{\partial \sigma_{xy}}{\partial \eta}\frac{\partial \eta}{\partial y} + \frac{\partial \sigma_{xz}}{\partial \eta}\frac{\partial \eta}{\partial z} + f_x, \tag{B-1}$$

$$\rho \frac{\partial v}{\partial t} = \frac{\partial \sigma_{xy}}{\partial \xi} + \frac{\partial \sigma_{xy}}{\partial \eta}\frac{\partial \eta}{\partial x} + \frac{\partial \sigma_{yy}}{\partial \tau} + \frac{\partial \sigma_{yy}}{\partial \eta}\frac{\partial \eta}{\partial y} + \frac{\partial \sigma_{yz}}{\partial \eta}\frac{\partial \eta}{\partial z} + f_y, \tag{B-2}$$

$$\rho \frac{\partial w}{\partial t} = \frac{\partial \sigma_{xz}}{\partial \xi} + \frac{\partial \sigma_{xz}}{\partial \eta}\frac{\partial \eta}{\partial x} + \frac{\partial \sigma_{yz}}{\partial \tau} + \frac{\partial \sigma_{yz}}{\partial \eta}\frac{\partial \eta}{\partial y} + \frac{\partial \sigma_{zz}}{\partial \eta}\frac{\partial \eta}{\partial z} + f_z, \tag{B-3}$$

$$\frac{\partial \sigma_{xx}}{\partial t} = \lambda \left(\frac{\partial u}{\partial \xi} + \frac{\partial u}{\partial \eta}\frac{\partial \eta}{\partial x} + \frac{\partial v}{\partial \tau} + \frac{\partial v}{\partial \eta}\frac{\partial \eta}{\partial y} + \frac{\partial w}{\partial \eta}\frac{\partial \eta}{\partial z} \right) + 2\mu \left(\frac{\partial u}{\partial \xi} + \frac{\partial u}{\partial \eta}\frac{\partial \eta}{\partial x} \right), \tag{B-4}$$

$$\frac{\partial \sigma_{yy}}{\partial t} = \lambda \left(\frac{\partial u}{\partial \xi} + \frac{\partial u}{\partial \eta}\frac{\partial \eta}{\partial x} + \frac{\partial v}{\partial \tau} + \frac{\partial v}{\partial \eta}\frac{\partial \eta}{\partial y} + \frac{\partial w}{\partial \eta}\frac{\partial \eta}{\partial z} \right) + 2\mu \left(\frac{\partial v}{\partial \tau} + \frac{\partial v}{\partial \eta}\frac{\partial \eta}{\partial y} \right), \tag{B-5}$$

$$\frac{\partial \sigma_{zz}}{\partial t} = \lambda \left(\frac{\partial u}{\partial \xi} + \frac{\partial u}{\partial \eta}\frac{\partial \eta}{\partial x} + \frac{\partial v}{\partial \tau} + \frac{\partial v}{\partial \eta}\frac{\partial \eta}{\partial y} + \frac{\partial w}{\partial \eta}\frac{\partial \eta}{\partial z} \right) + 2\mu \left(\frac{\partial w}{\partial \eta}\frac{\partial \eta}{\partial z} \right), \tag{B-6}$$

$$\frac{\partial \sigma_{xy}}{\partial t} = \mu \left(\frac{\partial v}{\partial \xi} + \frac{\partial v}{\partial \eta}\frac{\partial \eta}{\partial x} + \frac{\partial u}{\partial \tau} + \frac{\partial u}{\partial \eta}\frac{\partial \eta}{\partial y} \right), \tag{B-7}$$

$$\frac{\partial \sigma_{xz}}{\partial t} = \mu \left(\frac{\partial w}{\partial \xi} + \frac{\partial w}{\partial \eta}\frac{\partial \eta}{\partial x} + \frac{\partial u}{\partial \eta}\frac{\partial \eta}{\partial z} \right), \tag{B-8}$$

$$\frac{\partial \sigma_{yz}}{\partial t} = \mu \left(\frac{\partial w}{\partial \tau} + \frac{\partial w}{\partial \eta}\frac{\partial \eta}{\partial y} + \frac{\partial v}{\partial \eta}\frac{\partial \eta}{\partial z} \right). \tag{B-9}$$

Substituting for $\partial \eta / \partial x$, $\partial \eta / \partial y$ and $\partial \eta / \partial z$ from equations (16)–(20), we get the medium equations (21)–(29).

APPENDIX C–BOUNDARY CONDITIONS

Assume a velocity vector $\vec{v}$ with components u, v and w is given in the (ξ, τ, η)–coordinate system with basis vectors $\vec{i}$, $\vec{j}$ and $\vec{k}$. This system is then rotated through angles (θ, ϕ) into a new (x', y', z')–coordinate system with basis vectors $\vec{i'}$, $\vec{j'}$ and $\vec{k'}$. θ is the rotation angle between the ξ–axis and the x'–axis in the (ξ, η)–plane. ϕ is the rotation angle between the τ–axis and the y'–axis in the (y', z')–plane. In this new system the vector $\vec{v}$ is denoted by $\vec{v'}$ with components u', v' and w'. Then we have the relationships

$$\begin{pmatrix} \vec{i'} \\ \vec{j'} \\ \vec{k'} \end{pmatrix} = \mathbf{A} \begin{pmatrix} \vec{i} \\ \vec{j} \\ \vec{k} \end{pmatrix}, \tag{C-1}$$

where $\mathbf{A}$ is the rotation matrix, given by equation (34). Correspondingly,

$$\begin{pmatrix} \vec{i} \\ \vec{j} \\ \vec{k} \end{pmatrix} = \mathbf{A}^{-1} \begin{pmatrix} \vec{i'} \\ \vec{j'} \\ \vec{k'} \end{pmatrix} = \mathbf{A}^{\mathrm{T}} \begin{pmatrix} \vec{i'} \\ \vec{j'} \\ \vec{k'} \end{pmatrix}, \tag{C-2}$$

where $\mathbf{A}^{-1}$ and $\mathbf{A}^{\mathrm{T}}$ are the inverse and transposed of $\mathbf{A}$ respectively.

Using $|\vec{n}| = \sqrt{\left(\frac{\partial z_0}{\partial \xi}\right)^2 + \left(\frac{\partial z_0}{\partial \tau}\right)^2 + 1}$, a unit normal vector to a surface topography element can be written as

$$\hat{n} = \frac{\vec{n}}{|\vec{n}|} = \frac{1}{|\vec{n}|} \left(-\frac{\partial z_0(\xi, \tau)}{\partial \xi}, -\frac{\partial z_0(\xi, \tau)}{\partial \tau}, 1\right)^{\mathrm{T}}$$
$$= (-\cos\phi\sin\theta, -\sin\phi, \cos\phi\cos\theta)^{\mathrm{T}} \tag{C-3}$$

with our choice of rotation angles. From this we get

$$\frac{\tan\phi}{\cos\theta} = \frac{\partial z_0(\xi, \tau)}{\partial \tau}, \text{ i.e. } \tan\phi = \frac{\partial z_0(\xi, \tau)}{\partial \tau}\cos\theta, \tag{C-4}$$

$$\cos\phi = \cos\left[\arctan\left(\frac{\partial z_0(\xi, \tau)}{\partial \tau}\cos\theta\right)\right] \tag{C-5}$$

$$\text{and } \sin\phi = \sin\left[\arctan\left(\frac{\partial z_0(\xi, \tau)}{\partial \tau}\cos\theta\right)\right]. \tag{C-6}$$

20

The coordinate transformation for $\vec{v}$ is given by $\vec{v} = \mathbf{A}\vec{v'}$, or $\vec{v'} = \mathbf{A}^{-1}\vec{v}$. Componentwise this is

$$u' = (\cos\theta)u - (\sin\theta\sin\phi)v - (\sin\theta\cos\phi)w, \qquad\text{(C-7)}$$

$$v' = (\cos\phi)v - (\sin\phi)w, \qquad\text{(C-8)}$$

$$w' = (\sin\theta)u + (\cos\theta\sin\phi)v + (\cos\theta\cos\phi)w. \qquad\text{(C-9)}$$

Applying the chain rule to a differentiable function f, we then get

$$\frac{\partial f}{\partial x'} = \frac{\partial f}{\partial \xi}\frac{\partial \xi}{\partial x'} + \frac{\partial f}{\partial \tau}\frac{\partial \tau}{\partial x'} + \frac{\partial f}{\partial \eta}\frac{\partial \eta}{\partial x'} = \frac{\partial f}{\partial \xi}\cos\theta + \frac{\partial f}{\partial \eta}\sin\theta, \qquad\text{(C-10)}$$

$$\begin{aligned}\frac{\partial f}{\partial y'} &= \frac{\partial f}{\partial \xi}\frac{\partial \xi}{\partial y'} + \frac{\partial f}{\partial \tau}\frac{\partial \tau}{\partial y'} + \frac{\partial f}{\partial \eta}\frac{\partial \eta}{\partial y'} \\ &= \frac{\partial f}{\partial \xi}(-\sin\theta\sin\phi) + \frac{\partial f}{\partial \tau}\cos\phi + \frac{\partial f}{\partial \eta}\cos\theta\sin\phi,\end{aligned} \qquad\text{(C-11)}$$

$$\begin{aligned}\frac{\partial f}{\partial z'} &= \frac{\partial f}{\partial \xi}\frac{\partial \xi}{\partial z'} + \frac{\partial f}{\partial \tau}\frac{\partial \tau}{\partial z'} + \frac{\partial f}{\partial \eta}\frac{\partial \eta}{\partial z'} \\ &= \frac{\partial f}{\partial \xi}(-\sin\theta\cos\phi) + \frac{\partial f}{\partial \tau}(-\sin\phi) + \frac{\partial f}{\partial \eta}\cos\theta\cos\phi.\end{aligned} \qquad\text{(C-12)}$$

The free boundary conditions (30)–(32) for the velocities have to be enforced in the local (x', y', z')–system, where the z'–axis is normal to the surface at the local point, i.e.

$$\frac{\partial u'}{\partial z'} = -\frac{\partial w'}{\partial x'}, \qquad\text{(C-13)}$$

$$\frac{\partial v'}{\partial z'} = -\frac{\partial w'}{\partial y'}, \qquad\text{(C-14)}$$

$$\frac{\partial w'}{\partial z'} = -\frac{\lambda}{\lambda + 2\mu}\left(\frac{\partial u'}{\partial x'} + \frac{\partial v'}{\partial y'}\right), \qquad\text{(C-15)}$$

If the chain rule is applied as above, we get

$$\begin{aligned}\frac{\partial u'}{\partial \xi}(-\sin\theta\cos\phi) &+ \frac{\partial u'}{\partial \tau}(-\sin\phi) + \frac{\partial u'}{\partial \eta}\cos\theta\cos\phi \\ &= -\frac{\partial w'}{\partial \xi}\cos\theta - \frac{\partial w'}{\partial \eta}\sin\theta,\end{aligned} \qquad\text{(C-16)}$$

$$\begin{aligned}\frac{\partial v'}{\partial \xi}(-\sin\theta\cos\phi) &+ \frac{\partial v'}{\partial \tau}(-\sin\phi) + \frac{\partial v'}{\partial \eta}\cos\theta\cos\phi \\ &= -\frac{\partial w'}{\partial \xi}(-\sin\theta\sin\phi) - \frac{\partial w'}{\partial \tau}\cos\phi - \frac{\partial w'}{\partial \eta}\cos\theta\sin\phi,\end{aligned} \qquad\text{(C-17)}$$

21

$$\frac{\partial w'}{\partial \xi}(-\sin\theta\cos\phi) + \frac{\partial w'}{\partial \tau}(-\sin\phi) + \frac{\partial w'}{\partial \eta}\cos\theta\cos\phi$$

$$= -\frac{\lambda}{\lambda+2\mu}\left(\frac{\partial u'}{\partial \xi}\cos\theta + \frac{\partial u'}{\partial \eta}\sin\theta + \frac{\partial v'}{\partial \xi}(-\sin\theta\sin\phi)\right.$$

$$\left. + \frac{\partial v'}{\partial \tau}\cos\phi + \frac{\partial v'}{\partial \eta}\cos\theta\sin\phi\right). \tag{C-18}$$

Now we apply the above expressions for u', v' and w' that were obtained from the rotation. This leads to

$$\left[\cos\theta\frac{\partial u}{\partial \xi} - \sin\theta\sin\phi\frac{\partial v}{\partial \xi} - \sin\theta\cos\phi\frac{\partial w}{\partial \xi}\right](-\sin\theta\cos\phi)$$

$$+ \left[\cos\theta\frac{\partial u}{\partial \tau} - \sin\theta\sin\phi\frac{\partial v}{\partial \tau} - \sin\theta\cos\phi\frac{\partial w}{\partial \tau}\right](-\sin\phi)$$

$$+ \left[\cos\theta\frac{\partial u}{\partial \eta} - \sin\theta\sin\phi\frac{\partial v}{\partial \eta} - \sin\theta\cos\phi\frac{\partial w}{\partial \eta}\right]\cos\theta\cos\phi$$

$$= \left[-\sin\theta\frac{\partial u}{\partial \xi} - \cos\theta\sin\phi\frac{\partial v}{\partial \xi} - \cos\theta\cos\phi\frac{\partial w}{\partial \xi}\right]\cos\theta$$

$$+ \left[-\sin\theta\frac{\partial u}{\partial \eta} - \cos\theta\sin\phi\frac{\partial v}{\partial \eta} - \cos\theta\cos\phi\frac{\partial w}{\partial \eta}\right]\sin\theta, \tag{C-19}$$

$$\left[\cos\phi\frac{\partial v}{\partial \xi} - \sin\phi\frac{\partial w}{\partial \xi}\right](-\sin\theta\cos\phi)$$

$$+ \left[\cos\phi\frac{\partial v}{\partial \tau} - \sin\phi\frac{\partial w}{\partial \tau}\right](-\sin\phi)$$

$$+ \left[\cos\phi\frac{\partial v}{\partial \eta} - \sin\phi\frac{\partial w}{\partial \eta}\right]\cos\theta\cos\phi$$

$$= \left[-\sin\theta\frac{\partial u}{\partial \xi} - \cos\theta\sin\phi\frac{\partial v}{\partial \xi} - \cos\theta\cos\phi\frac{\partial w}{\partial \xi}\right](-\sin\theta\sin\phi)$$

$$+ \left[-\sin\theta\frac{\partial u}{\partial \tau} - \cos\theta\sin\phi\frac{\partial v}{\partial \tau} - \cos\theta\cos\phi\frac{\partial w}{\partial \tau}\right]\cos\phi$$

$$+ \left[-\sin\theta\frac{\partial u}{\partial \eta} - \cos\theta\sin\phi\frac{\partial v}{\partial \eta} - \cos\theta\cos\phi\frac{\partial w}{\partial \eta}\right]\cos\theta\sin\phi, \tag{C-20}$$

$$\left[\sin\theta\frac{\partial u}{\partial \xi} + \cos\theta\sin\phi\frac{\partial v}{\partial \xi} + \cos\theta\cos\phi\frac{\partial w}{\partial \xi}\right](-\sin\theta\cos\phi)$$

$$+ \left[\sin\theta\frac{\partial u}{\partial \tau} + \cos\theta\sin\phi\frac{\partial v}{\partial \tau} + \cos\theta\cos\phi\frac{\partial w}{\partial \tau}\right](-\sin\phi)$$

$$+ \left[\sin\theta\frac{\partial u}{\partial \eta} + \cos\theta\sin\phi\frac{\partial v}{\partial \eta} + \cos\theta\cos\phi\frac{\partial w}{\partial \eta}\right]\cos\theta\cos\phi$$

$$= -\frac{\lambda}{\lambda+2\mu}\left\{\left[\cos\theta\frac{\partial u}{\partial \xi} - \sin\theta\sin\phi\frac{\partial v}{\partial \xi} - \sin\theta\cos\phi\frac{\partial w}{\partial \xi}\right]\cos\theta\right.$$

22

$$+\left[\cos\theta\frac{\partial u}{\partial\eta} - \sin\theta\sin\phi\frac{\partial v}{\partial\eta} - \sin\theta\cos\phi\frac{\partial w}{\partial\eta}\right]\sin\theta$$

$$+\left[\cos\phi\frac{\partial v}{\partial\xi} - \sin\phi\frac{\partial w}{\partial\xi}\right](-\sin\theta\sin\phi)$$

$$+\left[\cos\phi\frac{\partial v}{\partial\tau} - \sin\phi\frac{\partial w}{\partial\tau}\right]\cos\phi$$

$$+\left[\cos\phi\frac{\partial v}{\partial\eta} - \sin\phi\frac{\partial w}{\partial\eta}\right]\cos\theta\sin\phi\Bigg\}. \tag{C-21}$$

We divide the first of these equations by $\cos^2\theta\cos\phi$, the second by $\cos\theta\cos^2\phi$ and the third by $\cos^2\theta\cos^2\phi$. These divisions assume $\theta\neq\pi/2$ and $\phi\neq\pi/2$. This means that the topography cannot have vertical sections along the planes of rotation, i.e. the topography function must be single–valued. This is a reasonable assumption given that the topography function $z_0(\xi,\tau)$ is assumed to be smooth. After restructuring, the three equations become

$$\left(\frac{\tan^2\theta}{\cos\phi}+1\right)\frac{\partial u}{\partial\eta} = \tan\theta\left(1-\frac{1}{\cos\phi}\right)\frac{\partial u}{\partial\xi} - \left(\tan^2\theta\sin\phi+\tan\phi\right)\frac{\partial v}{\partial\xi}$$

$$-\left(\tan^2\theta\cos\phi+1\right)\frac{\partial w}{\partial\xi} + \frac{\tan\phi}{\cos\theta}\frac{\partial u}{\partial\tau} - \frac{\tan\theta}{\cos\theta}\tan\phi\sin\phi\frac{\partial v}{\partial\tau}$$

$$-\frac{\tan\theta}{\cos\theta}\sin\phi\frac{\partial w}{\partial\tau} + \tan\theta\left(\sin\phi-\tan\phi\right)\frac{\partial v}{\partial\eta} + \tan\theta\left(\cos\phi-1\right)\frac{\partial w}{\partial\eta}, \tag{C-22}$$

$$\left(\cos\theta\tan^2\phi+1\right)\frac{\partial v}{\partial\eta} = \tan\theta\sin\theta\frac{\tan\phi}{\cos\phi}\frac{\partial u}{\partial\xi} + \left(\tan\theta+\sin\theta\tan^2\phi\right)\frac{\partial v}{\partial\xi}$$

$$+\tan\phi\left(\sin\theta-\tan\theta\right)\frac{\partial w}{\partial\xi} - \frac{\tan\theta}{\cos\phi}\frac{\partial u}{\partial\tau} + \tan\phi\left(\frac{1}{\cos\theta}-1\right)\frac{\partial v}{\partial\tau}$$

$$-\left(\frac{\tan^2\phi}{\cos\theta}+1\right)\frac{\partial w}{\partial\tau} - \sin\theta\frac{\tan\phi}{\cos\phi}\frac{\partial u}{\partial\eta} + \tan\phi\left(1-\cos\theta\right)\frac{\partial w}{\partial\eta}, \tag{C-23}$$

$$\left(\frac{\lambda}{\lambda+2\mu}\left[\frac{\tan^2\theta}{\cos\phi}+\frac{\tan^2\phi}{\cos\theta}\right]-1\right)\frac{\partial w}{\partial\eta}$$

$$= \frac{1}{\cos\phi}\left(\frac{\lambda}{\lambda+2\mu}\frac{1}{\cos\phi}-\tan^2\theta\right)\frac{\partial u}{\partial\xi} - \tan\theta\tan\phi\left(\frac{\lambda}{\lambda+2\mu}\left[\frac{1}{\cos\phi}+\frac{1}{\cos\theta}\right]+1\right)\frac{\partial v}{\partial\xi}$$

$$+\tan\theta\left(\frac{\lambda}{\lambda+2\mu}\left[\frac{\tan^2\phi}{\cos\theta}-\frac{1}{\cos\phi}\right]-1\right)\frac{\partial w}{\partial\xi} - \frac{\tan\theta\tan\phi}{\cos\theta\cos\phi}\frac{\partial u}{\partial\tau}$$

$$+\frac{1}{\cos\theta}\left(\frac{\lambda}{\lambda+2\mu}\frac{1}{\cos\theta}-\tan^2\phi\right)\frac{\partial v}{\partial\tau} + \frac{\tan\phi}{\cos\theta}\left(-\frac{\lambda}{\lambda+2\mu}\frac{1}{\cos\theta}-1\right)\frac{\partial w}{\partial\tau}$$

$$+\frac{\tan\theta}{\cos\phi}\left(\frac{\lambda}{\lambda+2\mu}\frac{1}{\cos\phi}+1\right)\frac{\partial u}{\partial\eta} + \tan\phi\left(\frac{\lambda}{\lambda+2\mu}\left[\frac{1}{\cos\theta}-\frac{\tan^2\theta}{\cos\phi}\right]+1\right)\frac{\partial v}{\partial\eta}, \tag{C-24}$$

Using the relations $\tan\theta = \partial z_0(\xi,\tau)/\partial\xi$ and $\tan\phi = \partial z_0(\xi,\tau)/\partial\tau\cos\theta$ together with

the definitions (38)–(44) leads to the closed set of velocity boundary conditions at a free surface topography (35)–(37).

FIGURES

FIG. 1. Rectangular system surface.

FIG. 2. Curved system surface.

FIG. 3. The leftmost section shows the topography in a 100 × 100 km area centered at the NORESS array. The innermost 40 × 40 km was used in the modeling experiment. The dotted lines show the positions of the receivers in the two synthetic profiles and the circle outlines the NORESS array aperture containing sensors in a circular pattern. Labels are in kilometers and elevations are in meters above mean sea level. The black area is Lake Mjøsa (123 m above sea level).

FIG. 4. Snapshots of the vertical component of the particle velocity. The upper snapshots are horizontal sections at the free surface and the lower snapshots are vertical sections along a west-east profile through the center of the model. The time in the lower left corner of each horizontal section is the time from when the plane vertically incident P-wave was reflected from the surface. The straight wavefronts parallel to the model boundaries are artificial reflections from the absorbing boundaries which are seen also in the vertical sections. Note the strong scattering source located at Bronkeberget (2 km N, 10 km E) which is also highly prominent in real record analysis (Bannister et al., 1990).

FIG. 5. Seismograms extracted at the free surface of the model. The left section shows the vertical component of the particle velocity along a 30 km long west-east profile through the center of the model. The right section shows 3-component seismograms from a receiver 3.6 km east of the center.

FIG. 6. Length of topography gradient vector and Frobenius norm of Hessian matrix.
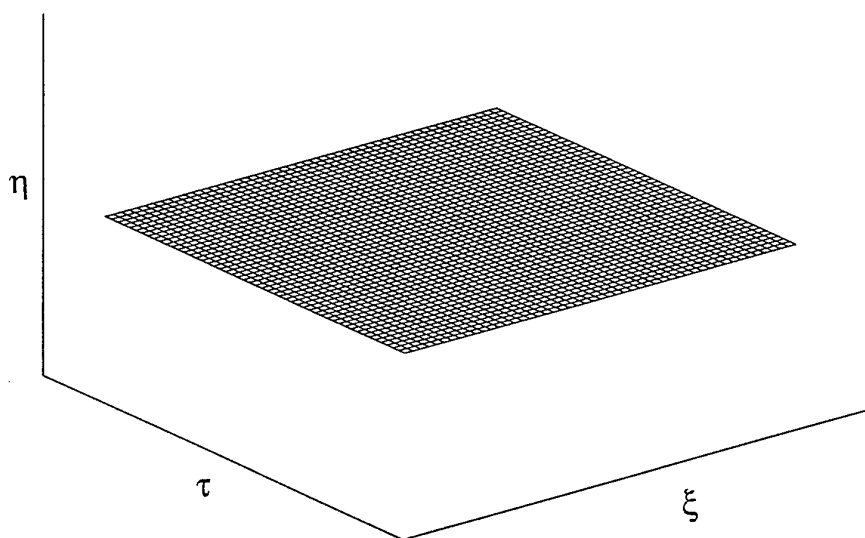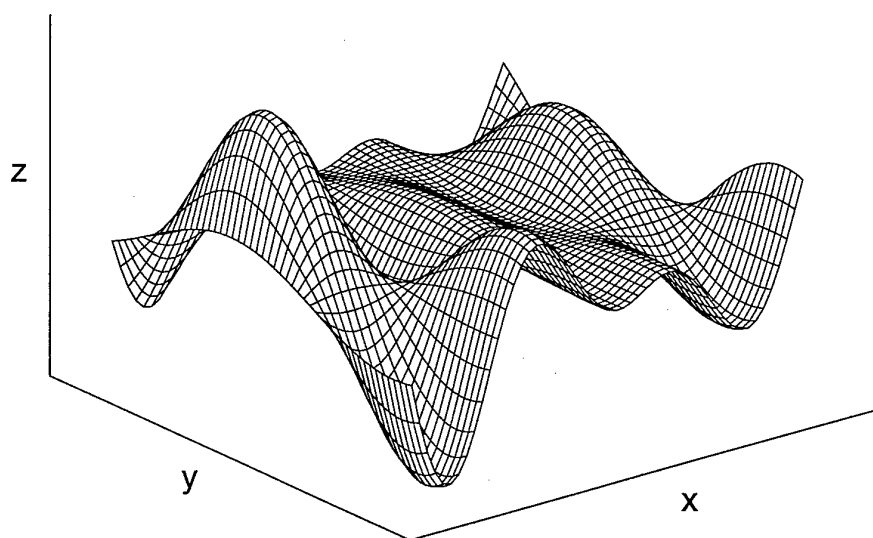
FIG. 1. Rectangular system surface.
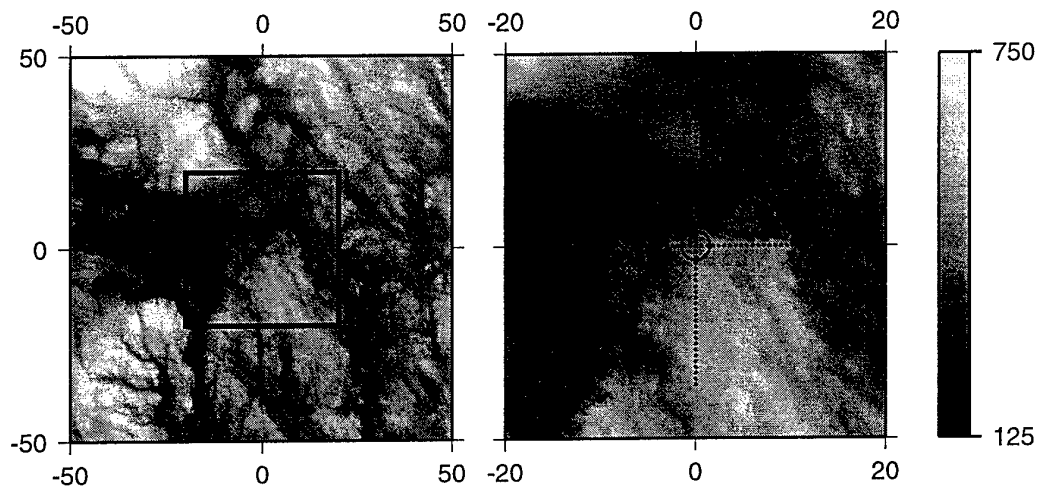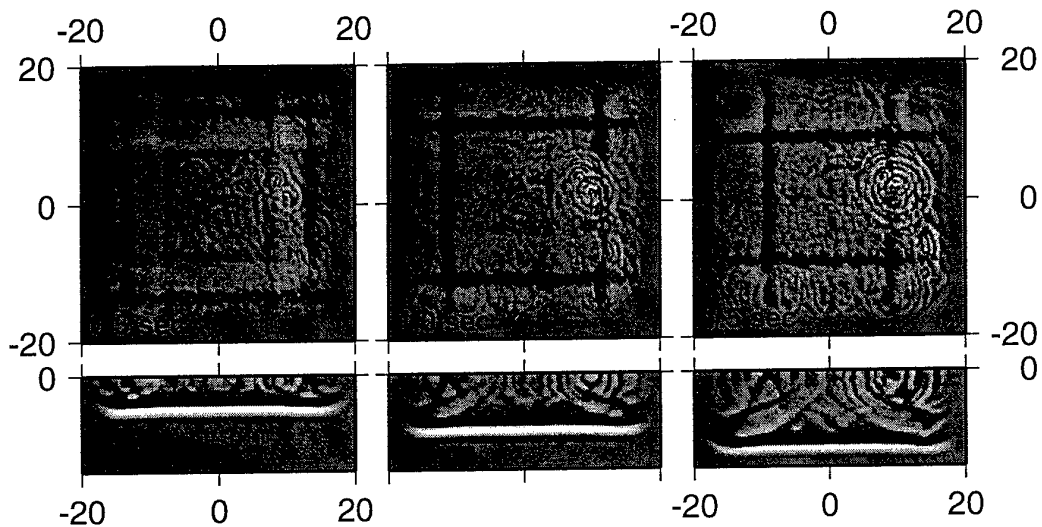
FIG. 2. Curved system surface.

FIG. 3. The leftmost section shows the topography in a 100 × 100 km area centered at the NORESS array. The innermost 40 × 40 km was used in the modeling experiment. The dotted lines show the positions of the receivers in the two synthetic profiles and the circle outlines the NORESS array aperture containing sensors in a circular pattern. Labels are in kilometers and elevations are in meters above mean sea level. The black area is Lake Mjøsa (123 m above sea level).

FIG. 4. Snapshots of the vertical component of the particle velocity. The upper snap-shots are horizontal sections at the free surface and the lower snapshots are vertical sections along a west-east profile through the center of the model. The time in the lower left corner of each horizontal section is the time from when the plane vertically incident P-wave was reflected from the surface. The straight wavefronts parallel to the model boundaries are artificial reflections from the absorbing boundaries which are seen also in the vertical sections. Note the strong scattering source located at Bronkeberget (2 km N, 10 km E) which is also highly prominent in real record analysis (Bannister et al., 1990).
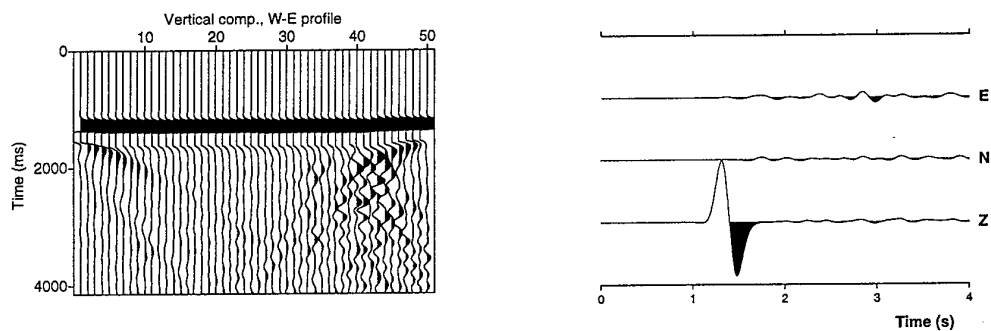
FIG. 5. Seismograms extracted at the free surface of the model. The left section shows the vertical component of the particle velocity along a 30 km long west-east profile through the center of the model. The right section shows 3-component seismograms from a receiver 3.6 km east of the center.
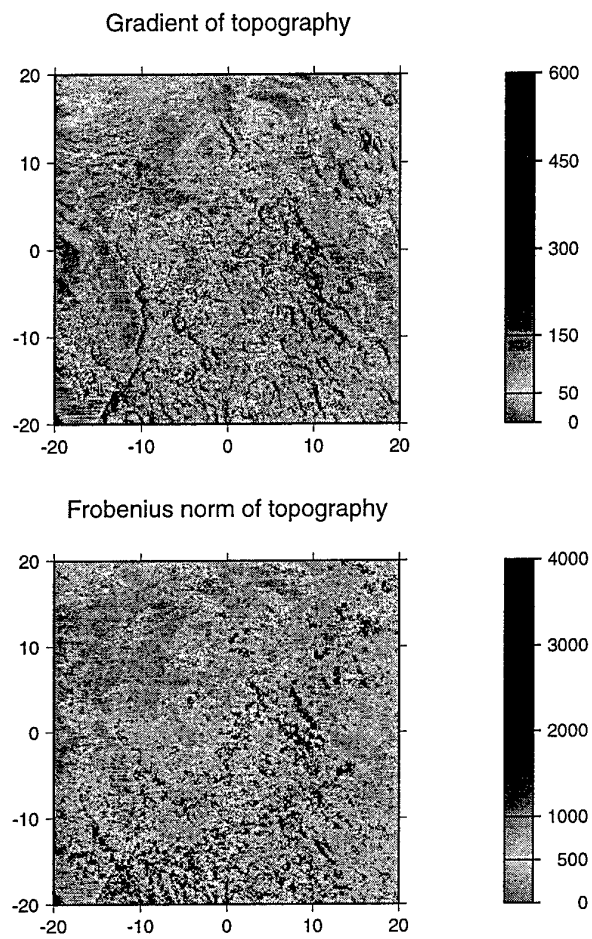
Gradient of topography

Frobenius norm of topography

FIG. 6. Length of topography gradient vector and Frobenius norm of Hessian matrix.

Appendix 7

3–D versus 2–D Finite Difference Seismic Synthetics including Real Surface Topography

Stig Hestholm
Rice Univ., Dept. of Geology and Geophysics, Houston, TX

Bent Ruud, Eystein Husebye
Univ. of Bergen, Dept. of Solid Earth Physics, Bergen, Norway

Short title: 3–D VERSUS 2–D REAL TOPOGRAPHY SYNTHETICS

Abstract. We have pursued and compared two– and three–dimensional (3–D) finite–difference (F–D) modeling of scattering from free surface topography. A velocity–stress formulation of the full elastic wave equations are combined with exact boundary conditions for the surface topography and numerically discretized by an 8th order F–D method on a staggered grid. We have simulated scattering in 2–D and 3–D from teleseismic P–waves using a plane, vertically incident P–wave and real topography from a 60 × 60 km area including the NORESS array in south–eastern Norway. Many field observations that are not easily explained by simpler 2–D cases are shown to better match qualitative effects from 3–D surface topography modeling. These include strong amplifications at hills, complex wave pattern caused by scattering, and directivity of scattered waves. Snapshots and seismograms show clear conversion from P– to Rg– (short period fundamental mode Rayleigh) waves in an area of rough topography in the vicinity of the array site. All results are consistent with numerous observations. By parallellization of the original software, possibilities have been opened for modeling with higher resolution and/or larger areas than before.

1. Introduction

Modeling free surface topography effects is naturally only important for seismic profiling on land, whereas in marine settings it satisfies to specify the medium parameters without including any explicit boundary conditions. The air–solid Earth interface exhibit the strongest possible impedance contrasts. For these reasons alone, modeling topography along such a free surface should be important. Any irregularities along such a surface would have additional consequences for the results, the more so the stronger the gradients and/or irregularities the local topography exhibits [*Hestholm and Ruud,* 1997]. Additionally, uncertain, or even undetermined, parameters are used when performing a seismic simulation, like seismic velocities and the associated densities. Topography data on the other hand, probably has the smallest error margins of any model parameters we use.

It is a goal for a seismic modeling experiment to achieve good match with observations. In this regard the advantage of modeling with surface topography is that implicit effects like scattering and conversion will be accounted for automatically in the wavefield synthetics. For example, plane incoming P– or S–waves cannot convert to Rg–waves when incident on a plane surface of a homogeneous medium. Also, P– to SH–phase conversion depends on surface topography. Amplification and deamplification of propagating waves can be shown to occur at irregularities and in substantial neighborhoods around them [*Sanchez–Sesma and Campillo,* 1991]. Alluvial filled irregular shaped valleys with a plane free surface is also seen to generate strong Love and Rg–waves for some incident waves in 3–D [*Sanchez–Sesma and Luzon,* 1995]. Real data correspondence of simulations has proven to be particularly important in works on earthquake hazard assessment. In urban areas housing are preferably located in hilly, 'socially prestigeous' areas, often with scant attention to possible amplifications from damaging earthquakes. Recently, a study aimed at shedding light on this aspect of hazard analysis has been released [*Pitarka and Irikura,* 1996].

Rg–waves can mask reflections that are the basis of migration. Over the NORESS–array in south–eastern Norway the Rg–waves seem to have amplitudes of about 10 % of those of the first teleseismic P–wave arrivals [*Bannister et al.,* 1990; *Gupta et al.,* 1993; *Hedlin et al.,* 1991]. By quantitatively accounting for topography effects, a dataset better suited for migration can be produced. To illustrate how this might be used in practice, consider a simulation of an earth model with known surface topography. A good correspondence with real data should be obtained to make the initial model viable. Then, using the modeling algorithm to propagate the real data backwards in time by a technique like inverse time migration, good results might be obtained [*Sun and McMechan,* 1992].

With the advent of digital signal recording and deployment of large aperture arrays on preCambrian bedrocks in shield areas with moderate topography, unique opportunities were given for observing wavefield complexities [*Husebye and Ruud,* 1989]. In case of the NORSAR array (aperture ca 100 km), signal amplitudes were found to vary in the extreme by a factor of 10 across the array. In part, this can occur in a systematic manner [*Haddon and Husebye,* 1978]. These observations were modeled in a simplistic way in terms of a deepseated (ca 100 km) structural lense producing focussing and defocussing across the array aperture. Model residues, apparently of shallow origin, were attributed to shallow crust and topography. Another puzzling feature was the strong and persistent coda levels in teleseismic recordings. The question was considered whether the coda waves were primarily due to source side scattering (S to P and Rg to P) or to the receiver side (P to S and P to Rg). This problem was solved by *Bannister et al.* [1990], who identified specific scattering hills in the NORESS siting area where the P to Rg conversions were most effective. In array record studies of local events P to S scattering appears to be most effective both in forward and backwards modes [*Charrette,* 1991; *Hestholm et al.,* 1994; *Dainty,* 1995]. In profiling surveys scattering effects have been recognized and modeled in 2–D in terms of near surface cavities

[*Imhof*, 1996]. Strong Rg-waves have also been observed and attributed to near–surface irregularities with particularly high propagation efficiency in low–velocity weathering layers [*Levander and Hill*, 1985; *Ruud et al.*, 1993].

Not much has been published on the modeling of free surface topography in 2–D, and even less so in 3–D. A work that considers different slope types and combinations of them explicitly in 2–D is that of *Jih et al.* [1988]. A new 2–D approach [*Robertsson*, 1996] incorporates only topography portions parallel to the main axes and classifies every surface point in a way similar to *Jih et al.* [1988]. The scheme can handle both elastic and viscoelastic schemes and implements the field variables at each of 7 categories of surface topography points separately. A 2–D method which employs a complete tensorial formulation of the wave equations for modelling curved interfaces and free surface topography is *Komatitsch et al.* [1996]. This method has the advantage of using the same amount of spatial partial derivative calculations as for a Cartesian approach. This is 12.5 % less in 2–D and 22.2 % less in 3–D than the chain rule approach used in this work. However, it has the distinct disadvantage of 30 % extra memory requirement in 2–D and 60 % extra memory requirement in 3–D than the chain rule approach. In addition, as in the present method, most chain rule approaches use straight vertical grid lines, and therefore the memory difference will be even larger because some partial derivatives of the mapping functions vanish. *Frankel and Leith*'s [1992] 3–D topography modeling algorithm employs an F–D scheme of fourth order accuracy in space and uses a density taper to zero starting at the level of the free surface.

Another method for 3–D surface topography modeling of elastic media is the boundary integral method in the spatial frequency domain [*Bouchon et al.*, 1996]. The medium Green functions have to be calculated for the explicit topography surface as integrals over horizontal wavenumbers. The diffracted wave field is the integral over the surface topography of the Green functions times unknown source density functions. The source density functions are solved for using the conjugate gradient method. Results

are shown for an incoming shear–wave polarized along the minor and major axes of a cosine–formed elliptically shaped hill. They investigate scattering effects of this hill on the wavefield propagating towards an otherwise plane surface in a homogeneous medium. *Sanchez–Sesma and Campillo* [1991] also use a boundary integral method to investigate topography effects. Boundary integral methods, or rather their numerical discretizations, boundary element methods, have not so far been applied to real surface topography modeling. Applications have been restricted to simple geometrical structures. This is probably because the discretization applied to each structure must be given specific thought.

The basis of the present method is the vanishing stress condition for a free surface. As in *Tessmer and Kosloff* [1994] (and earlier in *Tessmer et al.* [1992] in 2–D), a 3–D grid is used which is curved in the vertical direction and adapted to the surface topography, i. e. the top boundary of the grid coincides with the topography. A coordinate transform is used to transfer the elastic, isotropic wave equations from the curved to a rectangular grid in which the numerical computations are done. The velocity boundary conditions for a free surface are implemented into a local, rotated system at each point of the topography. Each of these systems has its vertical coordinate direction coinciding with the normal vector of the surface at the given point. The velocity boundary conditions are subsequently rotated back to the rectangular system. Once the boundary conditions are given in this system, the numerical discretization can be performed. New 3–D boundary conditions for the particle velocities at any arbitrary smooth topography without vertical subsections have thus been derived [*Hestholm and Ruud*, 1997].

In this study, we state the equations of motion and the surface topography boundary conditions for our approach. Next we give a description of the numerical discretization and a stability criterium for the method. Then we present simulated scattering from teleseismic P–waves using a plane vertically incident P–wave and real topography from an area that includes the NORESS array in south-eastern Norway.

2. Elastic Wave Modeling Formulation

The basic equations governing wave propagation in a continuous elastic medium are the momentum conservation and the stress–strain relationship. The velocity–stress formulation [*Achenbach*, 1975; *Virieux*, 1986] can be written in 3–D as in *Hestholm and Ruud* [1997]. We perform a linear transformation from a rectangular (ξ, τ, η)–system (Figure 1) to a curved (x, y, z)–system (Figure 2), where the relationship between the systems is

$$x(\xi, \tau, \eta) = \xi, \tag{1}$$

$$y(\xi, \tau, \eta) = \tau, \tag{2}$$

$$z(\xi, \tau, \eta) = \frac{\eta}{\eta_{max}} z_0(\xi, \tau). \tag{3}$$

The topography function $z_0(\xi, \tau)$ is the local height from the bottom to the surface of the curved (x, y, z)–system, and the rectangular (ξ, τ, η)–system is bounded by $\xi = 0$, $\xi = \xi_{max}$, $\tau = 0$, $\tau = \tau_{max}$, $\eta = 0$ and $\eta = \eta_{max}$. By expanding the velocity–stress formulation of the elastic wave equations by the chain rule [*Hestholm and Ruud*, 1997], we get the equations for the wave propagation in the medium

$$\rho \frac{\partial u}{\partial t} = \frac{\partial \sigma_{xx}}{\partial \xi} + A(\xi, \tau, \eta)\frac{\partial \sigma_{xx}}{\partial \eta} + \frac{\partial \sigma_{xy}}{\partial \tau} + B(\xi, \tau, \eta)\frac{\partial \sigma_{xy}}{\partial \eta} + C(\xi, \tau)\frac{\partial \sigma_{xz}}{\partial \eta} + f_x, \tag{4}$$

$$\rho \frac{\partial v}{\partial t} = \frac{\partial \sigma_{xy}}{\partial \xi} + A(\xi, \tau, \eta)\frac{\partial \sigma_{xy}}{\partial \eta} + \frac{\partial \sigma_{yy}}{\partial \tau} + B(\xi, \tau, \eta)\frac{\partial \sigma_{yy}}{\partial \eta} + C(\xi, \tau)\frac{\partial \sigma_{yz}}{\partial \eta} + f_y, \tag{5}$$

$$\rho \frac{\partial w}{\partial t} = \frac{\partial \sigma_{xz}}{\partial \xi} + A(\xi, \tau, \eta)\frac{\partial \sigma_{xz}}{\partial \eta} + \frac{\partial \sigma_{yz}}{\partial \tau} + B(\xi, \tau, \eta)\frac{\partial \sigma_{yz}}{\partial \eta} + C(\xi, \tau)\frac{\partial \sigma_{zz}}{\partial \eta} + f_z, \tag{6}$$

$$\frac{\partial \sigma_{xx}}{\partial t} = (\lambda + 2\mu)\left(\frac{\partial u}{\partial \xi} + A(\xi, \tau, \eta)\frac{\partial u}{\partial \eta}\right) + \lambda\left(\frac{\partial v}{\partial \tau} + B(\xi, \tau, \eta)\frac{\partial v}{\partial \eta} + C(\xi, \tau)\frac{\partial w}{\partial \eta}\right), \tag{7}$$

$$\frac{\partial \sigma_{yy}}{\partial t} = \lambda\left(\frac{\partial u}{\partial \xi} + A(\xi, \tau, \eta)\frac{\partial u}{\partial \eta} + C(\xi, \tau)\frac{\partial w}{\partial \eta}\right) + (\lambda + 2\mu)\left(\frac{\partial v}{\partial \tau} + B(\xi, \tau, \eta)\frac{\partial v}{\partial \eta}\right), \tag{8}$$

$$\frac{\partial \sigma_{zz}}{\partial t} = \lambda\left(\frac{\partial u}{\partial \xi} + A(\xi, \tau, \eta)\frac{\partial u}{\partial \eta} + \frac{\partial v}{\partial \tau} + B(\xi, \tau, \eta)\frac{\partial v}{\partial \eta}\right) + (\lambda + 2\mu)C(\xi, \tau)\frac{\partial w}{\partial \eta}, \tag{9}$$

$$\frac{\partial \sigma_{xy}}{\partial t} = \mu\left(\frac{\partial v}{\partial \xi} + A(\xi, \tau, \eta)\frac{\partial v}{\partial \eta} + \frac{\partial u}{\partial \tau} + B(\xi, \tau, \eta)\frac{\partial u}{\partial \eta}\right), \tag{10}$$

$$\frac{\partial \sigma_{xz}}{\partial t} = \mu \left(\frac{\partial w}{\partial \xi} + A(\xi, \tau, \eta) \frac{\partial w}{\partial \eta} + C(\xi, \tau) \frac{\partial u}{\partial \eta} \right), \tag{11}$$

$$\frac{\partial \sigma_{yz}}{\partial t} = \mu \left(\frac{\partial w}{\partial \tau} + B(\xi, \tau, \eta) \frac{\partial w}{\partial \eta} + C(\xi, \tau) \frac{\partial v}{\partial \eta} \right), \tag{12}$$

where $A(\xi, \tau, \eta)$, $B(\xi, \tau, \eta)$ and $C(\xi, \tau)$ are functions of the topography function $z_0(\xi, \tau)$, its spatial derivatives and the rectangular grid coordinates,

$$A(\xi, \tau, \eta) = \frac{\partial \eta}{\partial x} = -\frac{\eta}{z_0(\xi, \tau)} \frac{\partial z_0(\xi, \tau)}{\partial \xi}, \tag{13}$$

$$B(\xi, \tau, \eta) = \frac{\partial \eta}{\partial y} = -\frac{\eta}{z_0(\xi, \tau)} \frac{\partial z_0(\xi, \tau)}{\partial \tau}, \tag{14}$$

$$C(\xi, \tau) = \frac{\partial \eta}{\partial z} = \frac{\eta_{max}}{z_0(\xi, \tau)}. \tag{15}$$

The topography function $z_0(\xi, \tau)$ is the local height from the bottom to the surface of the curved (x, y, z)–system, of which the surface is shown in Figure 2. ρ is the density and λ and μ are Lamé's parameters. f_x, f_y and f_z are the components of the body forces, and u, v and w are the particle velocity components. σ_{xx}, σ_{yy}, σ_{zz}, σ_{xy}, σ_{xz} and σ_{yz} are the stress components. Equations (4)–(12) are the momentum conservation equations and Hooke's law for the curved system, now given in the rectangular (ξ, τ, η)–system.

The 3–D particle velocity boundary conditions for a free surface topography given in the computational (ξ, τ, η)–system [*Hestholm and Ruud, 1997*] can be given by

$$\left(\frac{d^2}{q} + 1 \right) \frac{\partial u}{\partial \eta} = d \left(1 - \frac{1}{q} \right) \frac{\partial u}{\partial \xi} - \left(d^2 r + p \right) \frac{\partial v}{\partial \xi} - \left(d^2 q + 1 \right) \frac{\partial w}{\partial \xi} + \frac{p}{e} \frac{\partial u}{\partial \tau}$$

$$- \frac{dpr}{e} \frac{\partial v}{\partial \tau} - \frac{dr}{e} \frac{\partial w}{\partial \tau} + d \left(r - p \right) \frac{\partial v}{\partial \eta} + d \left(q - 1 \right) \frac{\partial w}{\partial \eta}, \tag{16}$$

$$\left(ep^2 + 1 \right) \frac{\partial v}{\partial \eta} = \frac{dfp}{q} \frac{\partial u}{\partial \xi} + \left(d + fp^2 \right) \frac{\partial v}{\partial \xi} + p \left(f - d \right) \frac{\partial w}{\partial \xi} - \frac{d}{q} \frac{\partial u}{\partial \tau}$$

$$+ p \left(\frac{1}{e} - 1 \right) \frac{\partial v}{\partial \tau} - \left(\frac{p^2}{e} + 1 \right) \frac{\partial w}{\partial \tau} - \frac{fp}{q} \frac{\partial u}{\partial \eta}$$

$$+ p \left(1 - e \right) \frac{\partial w}{\partial \eta}, \tag{17}$$

$$\left(\zeta \left[\frac{d^2}{q} + \frac{p^2}{e} \right] - 1 \right) \frac{\partial w}{\partial \eta} = \frac{1}{q} \left(\frac{\zeta}{q} - d^2 \right) \frac{\partial u}{\partial \xi} - dp \left(\zeta \left[\frac{1}{q} + \frac{1}{e} \right] + 1 \right) \frac{\partial v}{\partial \xi}$$

$$+ d \left(\zeta \left[\frac{p^2}{e} - \frac{1}{q} \right] - 1 \right) \frac{\partial w}{\partial \xi} - \frac{dp}{eq} \frac{\partial u}{\partial \tau} + \frac{1}{e} \left(\frac{\zeta}{e} - p^2 \right) \frac{\partial v}{\partial \tau}$$

$$- \frac{p}{e} \left(\frac{\zeta}{e} + 1 \right) \frac{\partial w}{\partial \tau} + \frac{d}{q} \left(\frac{\zeta}{q} + 1 \right) \frac{\partial u}{\partial \eta}$$

$$+ p \left(\zeta \left[\frac{1}{e} - \frac{d^2}{q} \right] + 1 \right) \frac{\partial v}{\partial \eta}, \tag{18}$$

with

$$\zeta = \frac{\lambda}{\lambda + 2\mu} \tag{19}$$

and

$$d = \frac{\partial z_0(\xi, \tau)}{\partial \xi}, \tag{20}$$

$$e = \cos\left[\arctan\left(d\right)\right], \tag{21}$$

$$f = \sin\left[\arctan\left(d\right)\right], \tag{22}$$

$$p = \frac{\partial z_0(\xi, \tau)}{\partial \tau} e, \tag{23}$$

$$q = \cos\left[\arctan\left(p\right)\right], \tag{24}$$

$$r = \sin\left[\arctan\left(p\right)\right]. \tag{25}$$

3. Numerical Discretization

The same spatial and time discretization methods as in the 2–D case are used [*Hestholm and Ruud*, 1994; *Kindelan et al.*, 1990; *Sguazzero et al.*, 1989]. The schemes employ a staggered discretization stencil of the velocity–stress formulation of the elastodynamic wave equations [*Levander*, 1988] based on *Virieux* [1986]. Only the particle velocities need to be defined at the surface topography. In order to get explicit expressions for the particle velocities and stresses at each time step, we stagger the vertical velocity component w half a grid length downwards and the horizontal velocity components u and v half a grid length positively along the ξ– and τ–directions respectively. Stresses are implemented at the grid nodes or at the middle of the 'plaquettes' (the 2–D case is shown in Figure 3). The 3–D boundary conditions

(16)–(18) are discretized by 2nd order, staggered F–D operators [*Fornberg, 1988*], from which the particle velocity surface values are solved for from the vertical partial derivative expressions. In this procedure, the horizontal partial derivatives are calculated one grid length or one and a half grid length below the free surface and considered known (Figure 3). Moving from the free surface into the medium, the central, staggered F–D method's order is gradually increased with depth, via 4th and 6th up to 8th order, which is the order used inside the domain. The 8th order method is dispersion–bounded and cost–optimized [*Kindelan et al., 1990*]. Along the artificial grid boundaries exponential damping is used [*Cerjan et al., 1985*]. In a layer of 25 points along each grid boundary, the stresses and velocities are multiplied by exponentially decreasing terms towards the boundary.

Generally, a stability criterion has to be satisfied in the numerical implementation when combining the medium equations (4)–(12) with the boundary conditions (16)–(18). It turns out that $min\{(z_0(\xi, \tau)\} \approx 3\eta_{max}$ is sufficient for stability in most cases [*Hestholm and Ruud, 1997*]. In such cases, the vertical grid distance (distance between grid points) should be a third of the horizontal grid distances in the (ξ, τ, η)–grid in order to maintain the same sampling rate in all directions of the physical (x, y, z)–grid.

4. Numerical Simulations using Real Topography

For F–D modeling experiments we have used digital elevation data for an area of 60×60 km containing the NORESS array in south–eastern Norway (Figure 4). This hilly area was chosen because of easy access to detailed topography data. Additionally, significant P to Rg scattering from specific hills is well documented from NORESS record analysis [*Bannister et al., 1990*]. The code has been parallellized using MPI (Message Passing Interface). In this way we are able to run 3–D models with about 10^8 gridpoints on the most recent Cray Origin 2000 parallel machine. In the following examples, we display 2–D and 3–D simulations with 0.2 km grid–sampling for a $60 \times$

60 km topography area displayed in Figure 4. The most prominent topography present in the dataset is the steep Skreikampen hill immediately west of the southern part of lake Mjøsa (the long south–north oriented dark pattern in the south–west area in Figure 4). In all the examples shown the incoming wave is a vertically incident plane P–wave simulating a teleseismic short period P–phase. The center frequency of the Ricker wavelet is 5 Hz, the P–wave velocity of the homogeneous medium is 6.0 km/s, the S–wave velocity is 3.46 km/s and the density is 2.0 kg/m^3. In this section we show simulations for gradually more complex situations, with a 3–D elastic simulation using the parallel code as the final result. The outline of displaying results for the same area with gradually added complexities will illustrate the need to include these complexities in both academic applications and exploration.

4.1. Topography Surface versus Plane Surface

Figure 5 shows shapshots for a 2–D simulation of an incident plane wave reflecting from a plane, free surface on top of a homogeneous medium of 28.8 km depth. Distances are in kilometers, so the area covers a 60 km long horizontal subsection. The left frames show the horizontal (u) (top) and vertical (w) (bottom) particle velocity component 0.12 seconds after the start of the simulation and 0.04 seconds after the reflection from the free surface of the center part of the plane wave. There is 1 second between each of the next snapshot frames. The snapshots show a clean reflection from the plane surface and artificial reflections from the top corners. All snapshots displayed in this section are scaled with respect to a maximum value determined for each simulation. This means that amplitudes can be compared directly within the same figure.

The snapshots in Figure 6 show the exact same times, model depth and source location/type as in Figure 5, but here the actual NORESS topography is added (the 60 km long west–east profile of Figure 4). The medium is still homogeneous, so the scattering is caused only by the topography. The strongest scattered waves are seen

to radiate out from the surface at two points about 25 km and 45 km from the left edge, coinciding with areas of steep topography (see Figure 4). The steep hill directly west of lake Mjøsa along the profile seems to be at the edge of the present model and not contributing much to the scattering because of the absorbing boundary conditions acting there. The scattered waves are best seen on the u particle velocity component because this component is not affected by the strong vertically oriented wavefront. Rg–waves is the dominating feature at the surface, but converted and reflected P– and S–waves are also present in the snapshots. The field propagating away from the areas of prominent topography has a relatively coherent appearance.

Figure 7 shows the three following snapshot times for the simulation in Figure 5 (plane surface). Except for the reflected surface wave seen on the w–component snapshots, only artificial reflections emanate from the top corners and sides. Figure 8 shows the same snapshots with the topography added, i.e. the simulation of Figure 6 for the next three times. The artificial reflections propagate further into the medium, and the scattered waves from the areas of prominent topography are seen to traverse downwards. This is most clearly seen on the u–component. The scattered wavefield continues to show a coherent appearance, and no wavefronts are seen after the first two clear ones propagating out slightly to the left of the middle of the model.

4.2. 3–D versus 2–D

For the 3–D simulation we use the 60 × 60 km NORESS topography area (Figure 4, left) for a homogeneous 28.8 km deep model. Exactly the same source position and type are used as in the 2–D case, i.e. the same plane, vertically incident Gaussian.

4.2.1. Snapshots. The snapshots shown in Figure 9 are taken for the same particle velocity components (u and w) and at exactly the same locations as the topography data for the 2–D case, i.e. an xz–plane midway along the y–direction of the 60 × 60 km area. The snapshots of the w–component from the 3–D run seems

13

to differ slightly from the 2–D case by the stronger white band in the center of the wavefront. This must be because of an amplitude difference from geometrical spreading due to both the numerical discretization and actual physical geometrical spreading. Even if analytical geometrical spreading of a plane wave is impossible, it is important to remember that after reflection from the surface topography, the wavefront is no longer plane. As seen from Figure 9 the scattered surface waves appear to radiate out from secondary point sources which coincide with areas of high topographic gradients (Figure 4). Energy spreads out into the extra horizontal direction, therefore the amplitudes of the u–component, in particular, will be weaker than in 2–D. This is not apparent from the figures, since in order to visualize the scattering features, each figure is scaled according to a maximum value for that simulation. To the contrary of 2–D simulations, in 3–D the strongest amplitudes at a certain time may be from out–of–plane scattering, which will be delayed due to its longer travel path and complicate the wave pattern.

Another pronounced feature visible in the 3–D simulation is the disruption of the scattered wavefield. It appears to contain much stronger variations in its wavelengths, i.e. the spatial spectrum seems to contain more peaks than in the 2–D simulations. The total scattered wavefield has a much more complex appearance in 3–D than in 2–D. This can be seen on the wavefield pattern for both particle velocity components. 2–D simulations are expected to exhibit a greater degree of localization of the scattered wavefield than 3–D simulations [*Imhof*, 1996]. In view of the apparent energy partitioning into frequency peaks in 3–D, this is seen to hold if physical dispersion were included (as it would be for viscoelastic wave modeling).

The increased complexity of the 3–D scattered wavefield pattern is even more apparent in the next three snapshots of the u and w–components shown in Figure 10, where the scattered wavefield has propagated into most of the model. The corresponding 2–D snapshots (Figure 8) appear quite coherent beside the 3–D ones. Still, the clear

wavefronts of the 2–D scattered field can be recognized in 3–D, but they are here more complex and interspersed by new wavefronts due to out–of–plane scattering. This phenomenon is also the reason for slightly broader wavefronts of the u–component and the much more complex general appearance of the 3–D scattered wavefield compared to the 2–D one.

We finally show snapshots for the remaining dimensions from the 3–D simulation. Figures 11 and 12 display snapshots of the w particle velocity component for the times shown in the previous figures. The upper series in both figures show snapshots along the surface topography for the complete 60 × 60 km area, while the lower series is taken along the complete 60 × 28.8 km yz–plane at the midpoint along the x–direction.

The extra information drawn from the display of the scattered wavefield along the surface topography justifies 3–D simulations opposed to 2–D simulations. In particular, when investigating surface topography effects, the out–of–plane information is invaluable. The positions and shapes of the scattered waves can easily be traced with time in the snapshots. The strongest scattered waves can be seen to emanate from locations of strong topographic gradients. The strongest effect is seen to be caused by the steep area directly west of the Southern part of lake Mjøsa (near the lower left area of the horizontal snapshots). This area causes a prominent Rg–wavefront that can be traced on all the snapshots. It propagates slowly towards the middle part of the topography area, where it can be seen clearly on the last snapshot. Results are consistent with the ones found by *Pitarka and Irikura* [1996] and *Bouchon et al.* [1996], that elevated areas and high gradients amplify wave amplitudes and cause scattering away from these areas. The results in Figures 11 and 12 are also consistent with 3–D effects found from field experiments and from simulations [*Bouchon et al.*, 1996], i.e. the directivity of the wavefield. The most prominent topography causes Rg–waves propagating away from it, and these waves have stronger amplitudes in certain directions. The particularly clear wavefront propagating towards the center of

the area can be observed in all horizontal snapshots.

The absorbing boundary condition used in all the simulations is the exponential damping method according to *Cerjan et al.* [1985]. Extensive tests have been done [*Simone and Hestholm,* 1997] to verify that this method is among the best available. Nevertheless, a plane incident wave shows the method from its most unfavorable side, so that soon after the initiation, reflections will occur and propagate into the domain from all grid edges. This is clearly seen from Figures 11 and 12. The reflections appear as straight lines of much lower frequencies than the scattered wavefield. They might therefore be filtered out from the results by a filtering technique, but one cannot be sure of not eliminating some of the physically significant wave portions at the same time.

The 2–D simulations in this section took about 5 minutes on an IBM RISC 6000 model 590 workstation. The 3–D run took 2 days and nights (when others were also using the machine) on an Intel Paragon machine using 48 processors. This is a much slower machine than the 590 workstation, but it was not possible to access enough memory on the workstation for this 3–D simulation. However, on a new Cray Origin 2000 parallel machine using a sequential version of the program on one processor and the memory of 8 processors, the time for this 3–D simulation was reduced to 4 hours when others were also using the machine. The total memory requirements of the 2–D simulation was 2.3 MB, while the size of the 3–D simulation (including all overlap domains between processors) was 763 MB.

4.2.2. Seismograms. This section will compare seismograms for corresponding 2–D and 3–D simulations. 3–D seismograms are taken from the same 3–D simulation that was used for the snapshots. Synthetics are shown along the profile shown as the dashed lines in the left part of Figure 4. The first recordings are taken along the west–east profile at 40 km from the south grid boundary with stations starting at 25,6 km and ending at 55 km from the west grid boundary. The second record set is along the south–north profile at 40 km from the west grid boundary with the stations distributed

from 25,6 km to 55 km from the south grid boundary. There are 50 stations in each profile and the spacing between them is 600 m. In order to compare with 2–D runs, we performed 2–D simulations using exactly the same topography data and receiver locations as along the profiles for the 3–D simulation. This means that each 2–D profile consisted of 50 stations distributed from 25.6 km to 55 km from the lower grid edge with an inter–spacing of 600 m.

Figure 13 compares seismograms for the vertical particle velocity component in 2–D (left part) and 3–D (right part). The receiver profile is the west–east oriented one shown in the left part of Figure 4. The slightly slower 3–D arrival times are due to the fact that 4 extra grid points along all edges of the computational domain are included in the model compared to the 2–D case. Inside the 3–D domain these 4 points are the overlapping layers between processors for the parallel code, but along the computational domain edges they are included in the physical model. The strong arrivals striking the rightmost receivers and spreading into the model from the right in both seismograms are the artificial reflections from the east grid boundary. The other strong arrival at all receivers after 5 seconds in the right seismogram of Figure 13 is the artificial reflections from the north grid boundary. The left seismogram clearly shows coherent wavetrains emanating from the areas of prominent topography. These waves can be identified as S– and Rg–waves from their velocities. Going to the 3–D case on the right part of Figure 13, the picture becomes much more complicated. Still the prominent topographic relief from the 2–D case can be identified as causing the largest amount of scattering, but the arrivals are more incoherent and less localized than in 2–D. The relative amplitudes of the scattered phases are greatly enhanced compared to the 2–D case. As for the snapshots, the 3–D simulation causes the wave pattern to be more irregular, which is attributed to out–of–plane topographic scattering. This is also the reason for the extra scattered arrivals in 3–D. The overall weaker amplitudes of the 3–D simulation (corresponding seismograms are scaled up by 3.5) we attribute to geometrical

spreading, which will affect all phases generated near the surface after the plane wave has been reflected. In addition, geometrical spreading will occur due to the numerical definition of the plane wave at discrete grid points. This effect will therefore weaken all 3–D arrivals compared to 2–D ones. It is also possible that more destructive interference will occur in 3–D than in 2–D because of the extra dimension of discrete point sources interacting.

In Figure 14 we show seismograms from 2–D (left part) and 3–D (right part) simulations for the same receivers as in Figure 13, but here the first horizontal particle velocity component (the one directed west–east) is displayed. The artificial boundary reflections affecting this component, i.e. the ones from the east grid boundary, are seen clearly as both P– and S–wavetrains, and after 4 seconds the artificial P–reflections from the west boundary can also be seen coming in from the left. The areas of prominent topography are seen to give rise to the strongest amplitude amplifications of scattered waves from the incident plane wave in both the 2–D and 3–D cases. Still, the appearance of the latter is different and more complicated. Additionally, extra scattered arrivals can be identified in 3–D. They are caused by out–of–plane topography. Horizontal and vertical particle velocity components have the same scaling, and so from comparing the two components in each dimension we can confirm that the scattered surface amplitudes have the same order of magnitude for all components.

In Figure 15 seismograms for a 2–D simulation (left) and the 3–D simulation (right) are displayed for the 50 south–north oriented receivers shown in the left part of Figure 4. The 60 km long 2–D profile with irregular topography is taken along this receiver line and covers the complete yz–plane of the 3–D model. The vertical particle velocity component is displayed in Figure 15, and 3–D results are again scaled by a constant for comparison with the 2–D results. Artificial grid reflections as seen from the east boundary for the west–east profile propagate from the north boundary, and the large arrival in 3–D after 5 seconds is an artificial reflection from the east grid

boundary. In 2–D one can see that the areas of most topographic variations cause quite coherent amplitude amplifications. In 3–D the corresponding arrivals get masked from scattering from out–of–plane topography, although some of the 2–D topographic scattering pattern can be recognized on the 3–D seismogram. The 3–D topography is seen to cause scattering of much stronger relative amplitude compared to that caused by the 2–D topography.

Figure 16 shows seismograms for the same 2–D (left) and 3–D (right) simulations and for the same receivers as displayed in Figure 15, but here the south–north oriented particle velocity component is displayed. The P– and S–reflections from the north and south grid boundaries can be identified, as well as strong scattering from the areas of prominent topography. Again the 3–D case leads to a much more irregular wave pattern and extra scattered waves compared to the 2–D case, although not to the same extent as for the vertical particle velocity component.

5. Discussion

We have given details on our 3–D F–D scheme for computing synthetic seismograms based on the elastodynamic wave equations and produced results pertaining to the topography of the NORESS array siting area. The choice of area was motivated by easy access to topography data plus many array results exhibiting amplitude variations [*Haddon and Husebye,* 1978] and scattering phenomena [*Bannister et al.,* 1990; *Hedlin et al.,* 1994]. In our synthetic experiments we focussed on two topics; (i) to demonstrate the necessity of 3–D modelling for complex topographic features and (ii) scattering features tied to prominent hills. We used both snapshots of 2–D displays and profile seismograms to illustrate the results obtained in the experiments. Firstly, the 2–D synthetics are very much simpler than the corresponding 3–D ones due to out–of–plane contributions. This is expected and easily confirmed by f–k or semblance analysis of array recordings. A few examples are given by *Hestholm et al.* [1994]. Here loss of

directionality in the Lg–coda waves is demonstrated, i.e. both forward and backward scattered wavelets arrive from any direction. Additionally, coda coherency is low or hardly significant, at levels of 0.2–0.4 units [*Dainty,* 1995]. This is in contrast to the 2–D synthetics snapshots shown in the left parts of Figures 13–16 or from the semblance plots in *Hestholm et al.* [1994]. Also, from Figures 13–16 we see that 3–D coda waves are characterized by larger amplitudes than what is the case for 2–D records – naturally due to out–of–plane contributions. This reflects a problem in 2–D synthetics, namely that excessive and partly unrealistic velocity perturbations (exceeding 5 %) must be introduced to match RMS coda levels in observational records [*Hestholm et al.,* 1994; *Dainty,* 1995].

As observed by *Bannister et al.* [1990], some hills in the NORESS area literally radiate Rg–waves at regular intervals for incoming teleseismic waves of long durations. In this regard array recordings are just point observations while the synthetics in Figures 6–12 reveal nearly symmetric Rg–radiation from some secondary sources. However, with passing time the interference of phases from a multiplicity of secondary sources becomes complex (Figure 11), so propagation directionality from a secondary source to a receiver will generally weaken. An observational counterpart to this result is that Rg–waves rarely propagate further than 60 km in hilly areas typical of the NORESS and GERESS (Bavaria, Germany) arrays while across the plains of northern Fennoscandia Rg–waves from explosions occasionally propagate out to 600 km.

We have quoted observations pertaining to strong wavefield amplification on top of hills in areas of rough topography. As expected, the synthetics presented here only produce moderate amplitude variations along the profiles in Figures 13–16 – less than a factor of 2. The reason is that in order to obtain stronger amplitude variations, a large slice of the wavefront has to be focussed (compressed) into a small area. This is simply not feasible with our homogeneous crustal model. The observations in *Haddon and Husebye* [1978] reflect wavefront 'bending' taking place more than 100 km away from the

20

free surface sensors. This makes sense with moderate lithospheric velocity perturbations on the order of 3–5 %. Undoubtedly, some strong, localized wavefield amplifications have taken place in cities destroyed by earthquakes in view of their damage patterns.

6. Conclusions

It is demonstrated that 3–D F–D synthetic wavefield analysis including topography provides improved insight and a better understanding of surface scattering phenomena. Snapshots and seismograms display clear conversion to Rg–waves in areas of rough topography. Additionally, 3–D as opposed to 2–D modeling is shown to give significantly different results. The added effects from the extra complexities can contribute to explanations for deviations between numerical simulations performed on 2–D structures and 3–D scattering observed in the field. These discrepancies are connected to incoherent and unlocalized scattering, excessive amplitude amplifications and directionality dependencies. The last point can be observed in NORESS and GERESS recordings. At some sensors the Rg–phase is prominent while hardly visible at nearby sensors less than a kilometer away. Many of such wavefield phenomena are out of range for 2–D F–D synthetics. The major conclusion from the present study is that there is no substitute to 3–D synthetic wavefield modeling for obtaining an adequate comprehension of seismic wave propagation in the heterogeneous subsurface.

References

Achenbach, J. D., *Wave propagation in elastic solids,* North–Holland Publishing Co., The Netherlands, 1975.

Bannister, S. C., E. S. Husebye, and B. O. Ruud, Teleseismic P–coda analyzed by three-component and array techniques – deterministic location of topographic P–to–Rg scattering near the NORESS array, *Bull. Seismol. Soc. Am., 80,* 1969-1986, 1990.

Bouchon, M., C. A. Schultz, and M. N. Toksöz, Effect of three–dimensional topography on seismic motion, *J. Geophys. Res., 101,* 5835-5846, 1996.

Cerjan, C., D. Kosloff, R. Kosloff, and M. Reshef, Short note on a nonreflecting boundary condition for discrete acoustic–wave and elastic–wave equations, *Geophysics, 50,* 705-708, 1985.

Charrette, E. E. III, Elastic wave scattering in laterally inhomogeneous media, Ph.D. thesis, Massachusetts Institute of Technology, 1991.

Dainty, A. M., The influence of seismic scattering on monitoring, in *Monitoring a Comprehensive Test Ban Treaty,* edited by E. S. Husebye and A. M. Dainty, pp. 663-688, Kluwer Academic Publishers, Dordrecht, The Netherlands, 1995.

Fornberg, B., Generation of finite difference formulas on arbitrary spaced grids, *Mathematics of Computation, 51,* 699-706, 1988.

Frankel, A., and W. Leith, Evaluation of topographic effects on P and S–waves of explosions at the Northern Novaya Zemlya Test Site using 3–D numerical simulations, *Geophys. Res. Lett., 19,* 1887-1890, 1992.

Gupta, I. N., C. S. Lynnes, and R. A. Wagner, An array study of the effects of known local scatterers on regional phases, *Bull. Seismol. Soc. Am., 83,* 53-63, 1993.

Haddon, R. A. W., and E. S. Husebye, Joint interpretation of P–wave travel time and amplitude anomalies in terms of lithospheric heterogeneities, *Geophys. J. R. Astron. Soc., 55,* 19-44, 1978.

Hedlin, M. A., J. B. Minster, and J. A. Orcutt, Beam-stack imaging using a small aperture array, *Geophys. Res. Lett., 18,* 1771-1774, 1991.

Hedlin, M. A., J. B. Minster, and J. A. Orcutt, Resolution of prominent crustal scatterers near the NORESS small-aperture array, *Geoph. J. Int. 119,* 101-115, 1994.

Hestholm, S. O., and B. O. Ruud, 2D finite difference elastic wave modeling including surface topography, *Geoph. Prosp. 42,* 371-390, 1994.

Hestholm, S. O., and B. O. Ruud, 3–D finite difference elastic wave modeling including surface topography, *Geophysics 62,* in press, 1997.

Hestholm, S. O., E. S. Husebye, and B. O. Ruud, Seismic wave propagation in complex crust–upper mantle media using 2–D finite–difference synthetics, *Geoph. J. Int. 118,* 643-670, 1994.

Husebye, E. S., and B. O. Ruud, Array seismology – past, present and future developments, in *Observatory Seismology,* edited by J. J. Litehiser, pp. 123-153, Berkeley Univ. Press, Berkeley, CA, 1989.

Imhof, M. G., Scattering of elastic waves using non–orthogonal expansions, Ph.D. thesis, Massachusetts Institute of Technology, 1996.

Jih, R. S., K. L. McLaughlin, and Z. A. Der, Free–boundary conditions of arbitrary topography in a two–dimensional explicit finite difference scheme, *Geophysics 53,* 1045-1055, 1988.

Kindelan, M., A. Kamel, and P. Sguazzero, On the construction and efficiency of staggered numerical differentiators for the wave equation, *Geophysics 55,* 107-110, 1990.

Komatitsch, D., F. Coutel, and P. Mora, Tensorial formulation of the wave equation for modelling curved interfaces, *Geoph. J. Int. 127,* 156-168, 1996.

Levander, A. R., Fourth–order finite–difference P–SV seismograms, *Geophysics 53,* 1425-1436, 1988.

Levander, A. R., and N. R. Hill, P–SV resonances in irregular low–velocity surface layers, *Bull. Seismol. Soc. Am., 75,* 847-864, 1985.

Pitarka, A., and K. Irikura, Modeling 3D surface topography by finite–difference method: Kobe–JMA station site, Japan, case study, *Geophys. Res. Lett., 23,* 2729-2732, 1996.

Robertsson, J. O. A., A numerical free–surface condition for elastic/viscoelastic finite–difference modeling in the presence of topography, *Geophysics 61,* 1921-1934, 1996.

Ruud, B. O., E. S. Husebye, and S. O. Hestholm, Rg observations from four continents: inverse– and forward–modelling experiments, *Geoph. J. Int. 114,* 465-472, 1993.

Sanchez–Sesma, F. J., and M. Campillo, Diffraction of P, SV, and Rayleigh waves by topographic features: A boundary integral formulation, *Bull. Seismol. Soc. Am., 81,* 2234-2253, 1991.

Sanchez–Sesma, F. J., and F. Luzon, Seismic response of three–dimensional alluvial valleys for incident P, S, and Rayleigh waves, *Bull. Seismol. Soc. Am., 85,* 269-284, 1995.

Sguazzero, P., M. Kindelan, and A. Kamel, Dispersion–bounded numerical integration of the elastodynamic equations, *Proc. ICOSAHOM Conference, Como, Italy, June, 89, North Holland Publishing Company, The Netherlands,* 165-172, 1989.

Simone, A., and S. Hestholm, Instabilities in applying absorbing boundary conditions to high order seismic modeling algorithms, *Geophysics 62,* in press, 1997.

Sun, R., and G. A. McMechan, 2–D full–wavefield inversion for wide–aperture, elastic, seismic data, *Geoph. J. Int. 111,* 1-10, 1992.

Tessmer, E., and D. Kosloff, 3–D elastic modeling with surface topography by a Chebychev spectral method, *Geophysics 59,* 464-473, 1994.

Tessmer, E., D. Kosloff, and A. Behle, Elastic wave propagation simulation in the presence of surface topography, *Geoph. J. Int. 108,* 621-632, 1992.

Virieux, J., P-SV wave propagation in heterogeneous media: velocity–stress finite–difference method, *Geophysics 51,* 889-901, 1986.

S. Hestholm, Rice Univ., Dept. of Geology and Geophysics, 6100 Main, Houston, TX 77005–1892. B. Ruud and E. Husebye, Univ. of Bergen, Dept. of Solid Earth Physics,

Allégt. 41, N–5008 Bergen, Norway (e-mail: stig@rice.edu; BentOle.Ruud@ifjf.uib.no; Eystein.Husebye@ifjf.uib.no)
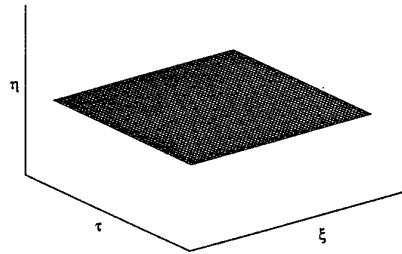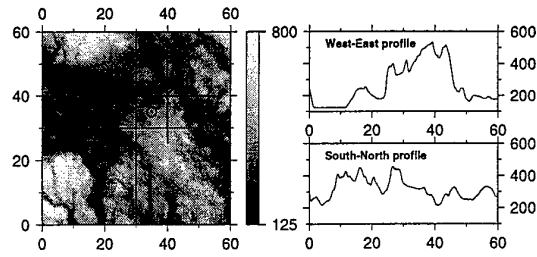
Figure 1. Rectangular system surface.
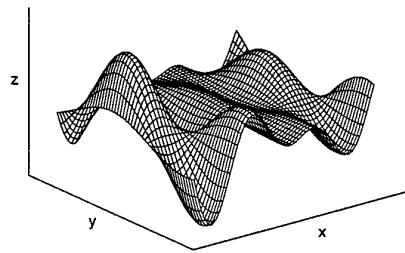
Figure 2. Curved system surface.

Figure 3. Computational staggered grid, (ξ, η)–plane.

Figure 4. *Left:* Map shows the topography of the 60 × 60 km area used in the 3–D simulation. The dashed lines show the positions of the receivers in two profiles and the circle outlines the NORESS array. Labels are in kilometers and elevations are in meters above mean sea level. The black area to the south–west is Lake Mjøsa (123 m above sea level). *Right:* Topography profiles along the two lines each of 60 km length shown on the map. They are midway along the y–direction and x–direction and cover respectively the complete x– and y–dimension of the area. Horizontal axes are in kilometers and vertical axes are in meters above mean sea level.
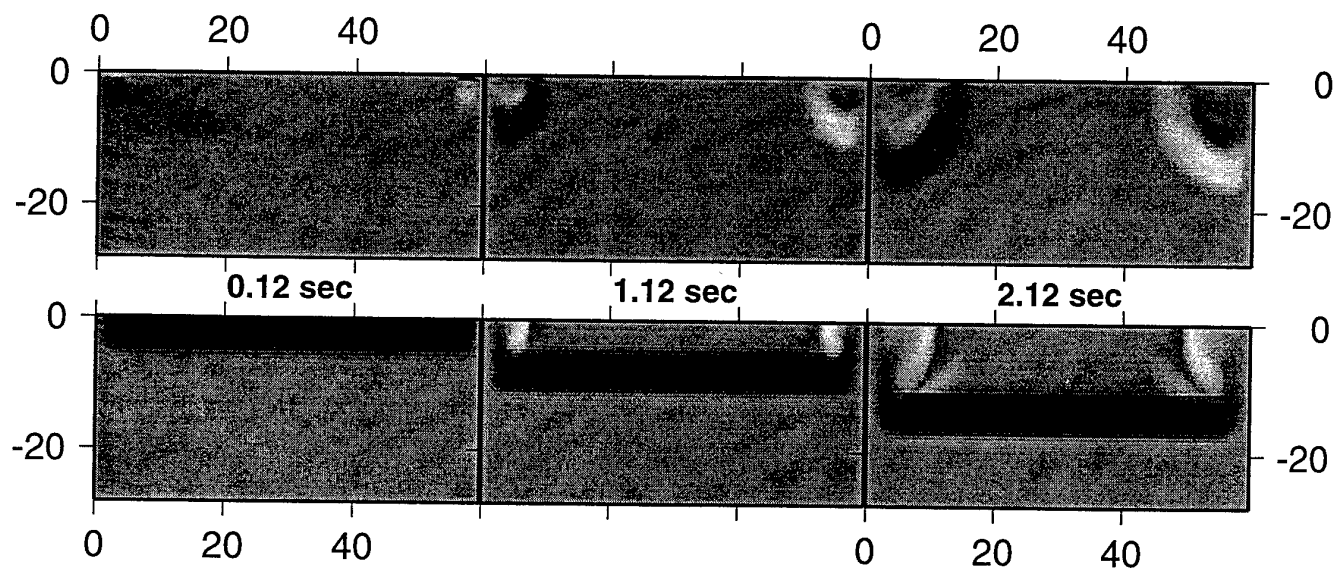
Figure 5. Snapshots of 2–D simulation of a plane, vertically incident P–wave reflecting from a plane, free surface. The first snapshot shows the wavefield 0.04 seconds after its reflection from the surface, and the time lap between each of the next snapshots is 1 second. Distances are in kilometers, and the upper and lower series display the horizontal and vertical particle velocity components respectively.
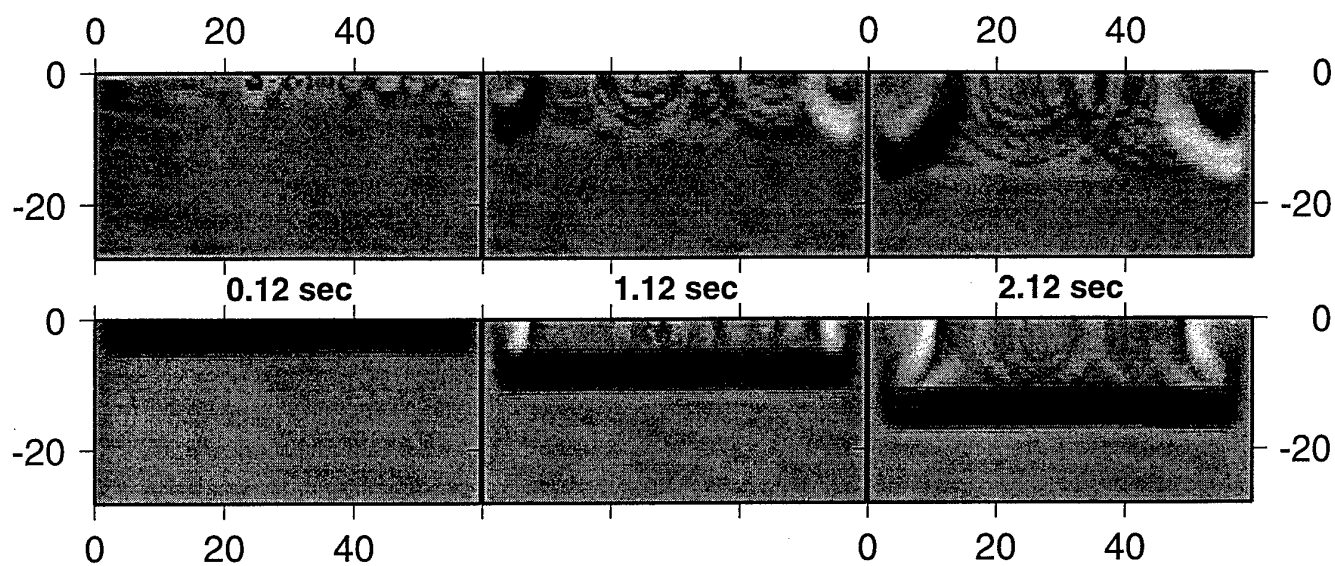
Figure 6. Same as Figure 5, but for an irregular free surface boundary condition. The topography is that of the west–east profile of Figure 4.
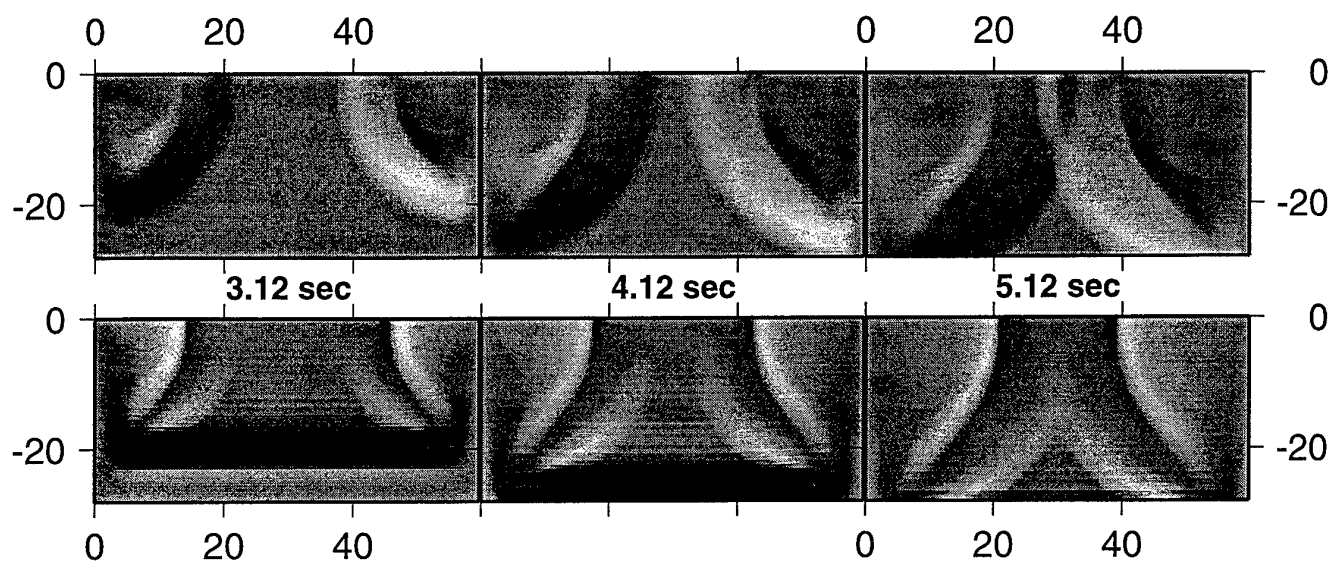
Figure 7. Same as Figure 5 for the next three snapshots.
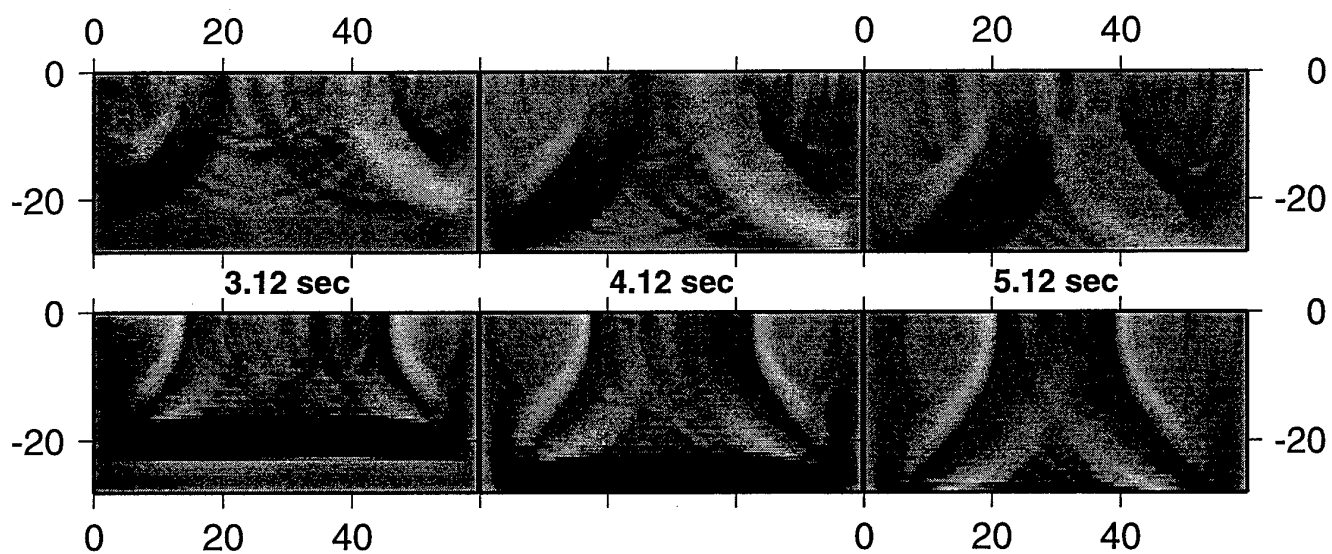
Figure 8. Same as Figure 6 for the next three snapshots.
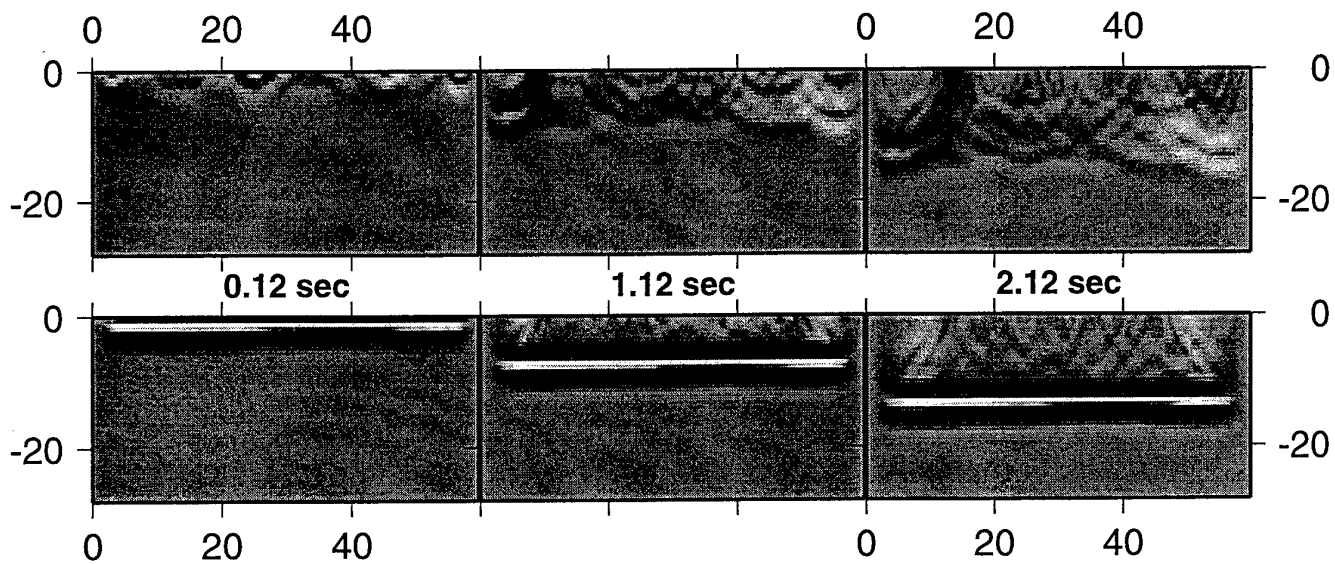
Figure 9. Snapshots of 3–D simulation of a plane, vertically incident Ricker wavelet reflecting from an irregular free surface. The first snapshot shows the wavefield 0.04 seconds after its reflection from the surface, and the time lap between each of the next snapshots is 1 second. Distances are in kilometers, and the upper and lower series display a horizontal (u) and vertical particle velocity component respectively. Snapshots are shown at the midpoint of the direction of the second horizontal dimension and correspond exactly to the snapshot locations of Figure 6 for the 2–D case.
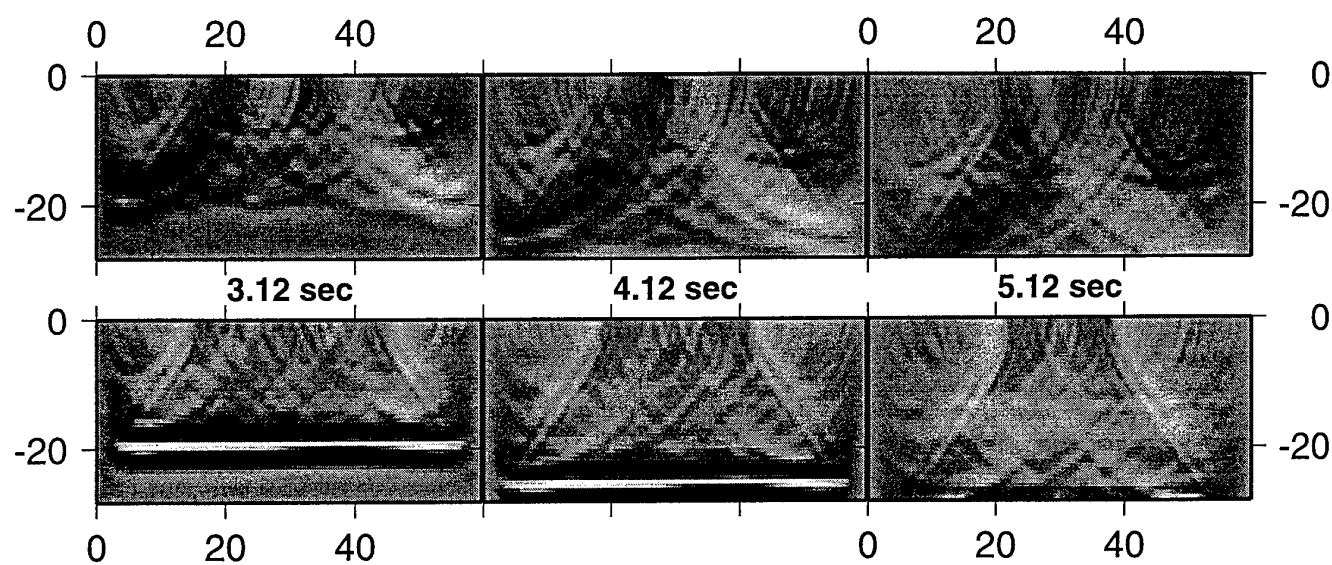
Figure 10. Same as Figure 9 for the next three snapshots.
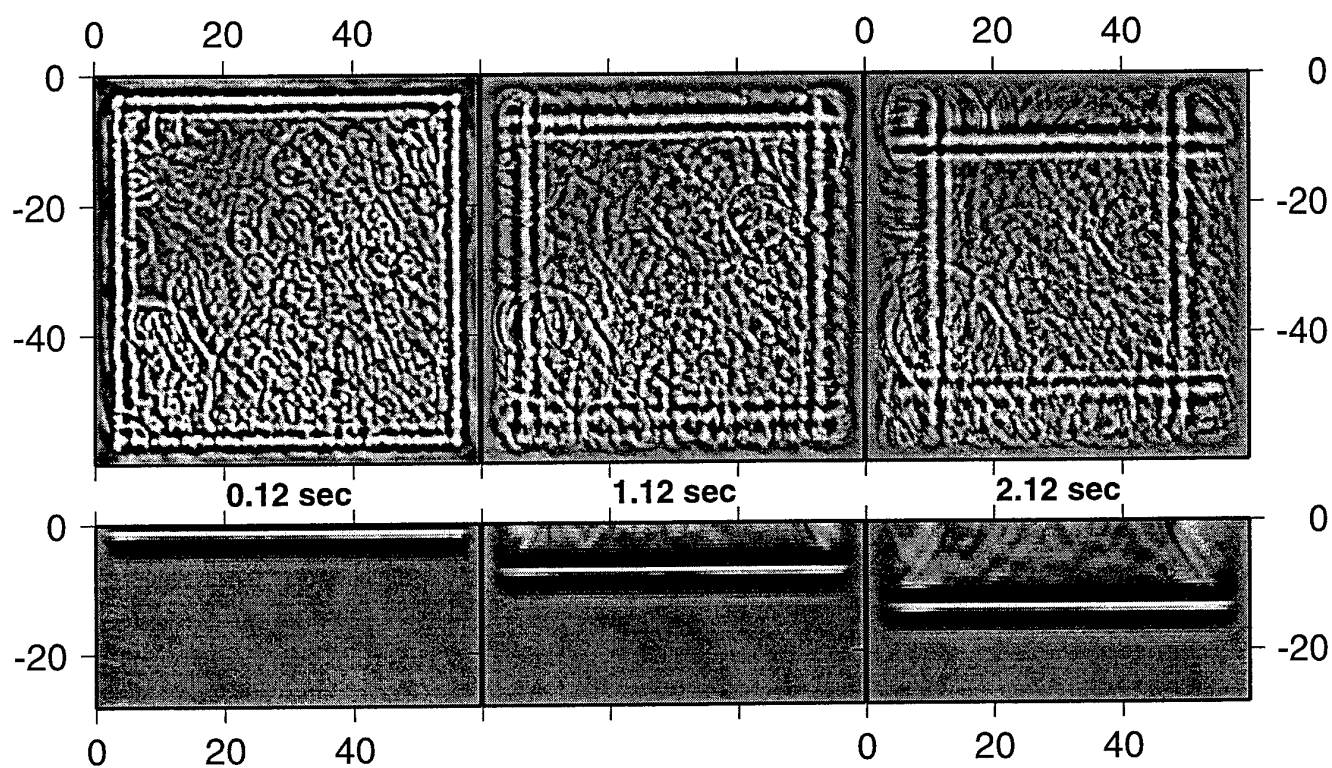
Figure 11. The simulation displayed in Figure 9 for the same times, but here snapshots are shown at the surface topography and along the plane of the midpoint of the first horizontal direction (along the yz-plane). Both series display the vertical particle velocity component (w).
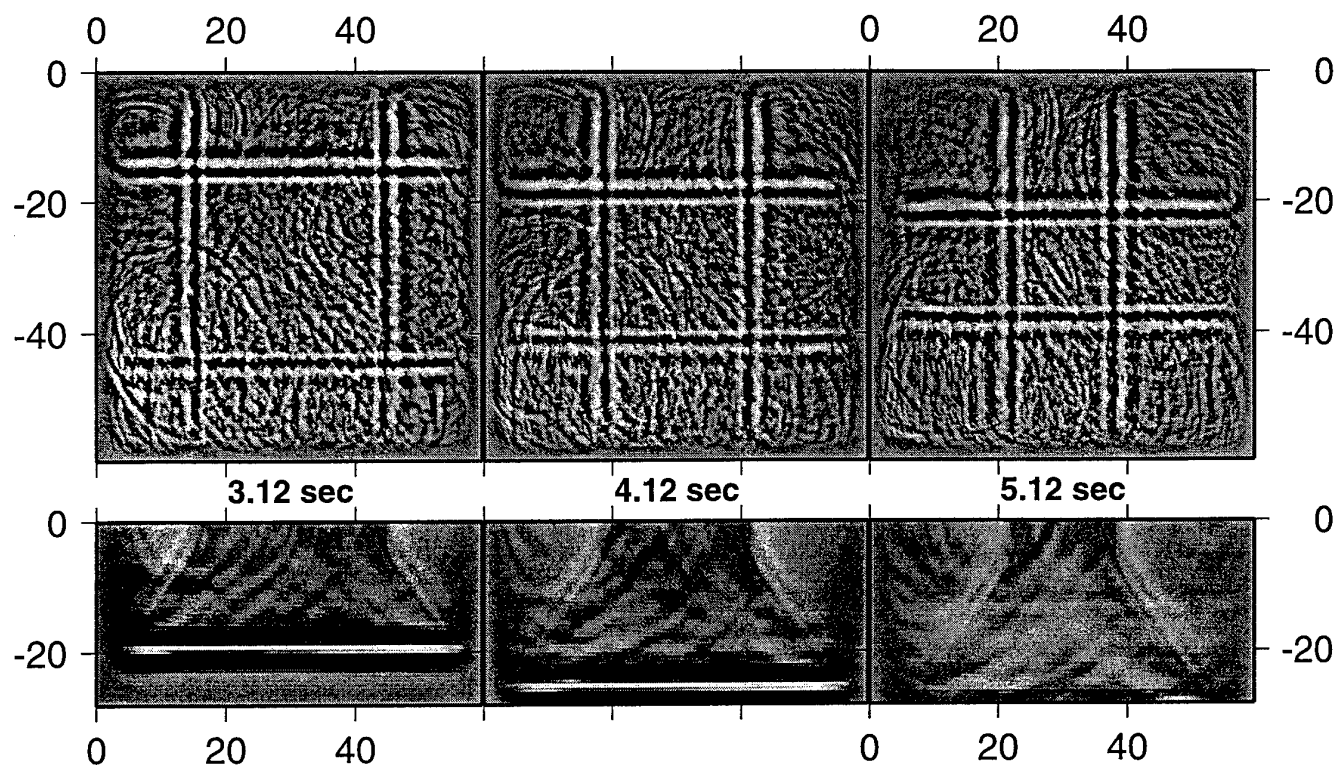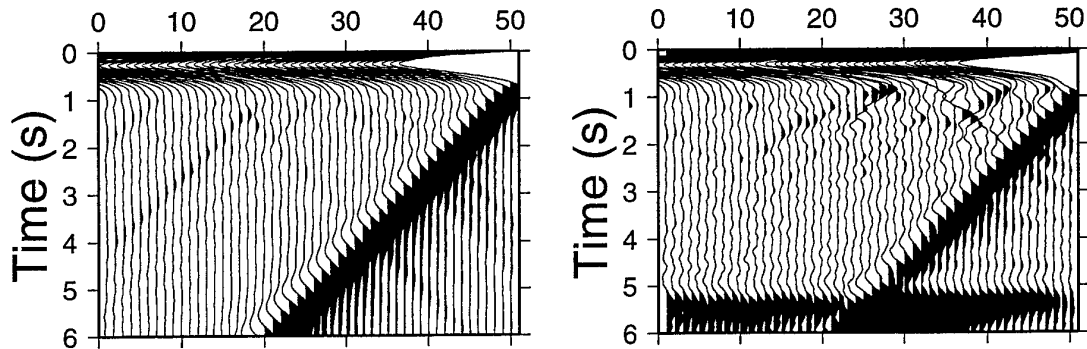
Figure 12. Same as Figure 11 for the next three snapshots.

Figure 13. *Left:* Seismogram from 2–D simulation of a 60 km long topography data profile taken along the west–east oriented receiver line from the left part of Figure 4. The profile is 28.8 km deep and extends from 25.6 km west of the leftmost receiver to 5 km east of the rightmost receiver. The profile contains the displayed line of 50 west–east oriented receivers inter–spaced by 600 m. The vertical particle velocity component is displayed. *Right:* Seismogram from the 3–D simulation of the 60 × 60 × 28.8 km model displayed in the snapshots. The 50 receivers are located along the west–east oriented receiver line displayed on the left part of Figure 4 and inter–spaced by 600 m. Because of geometrical spreading, the amplitudes are multiplied by 3.5 to make the main arrivals the same order of magnitude as those for the 2–D case on the left. The vertical particle velocity component is displayed.
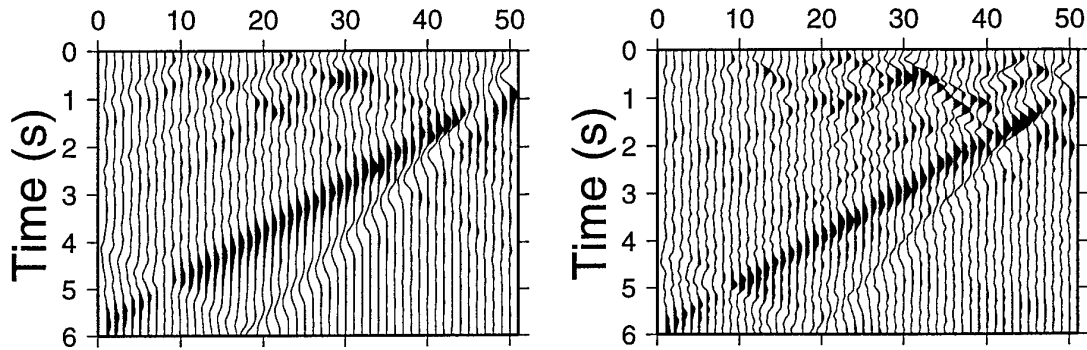
Figure 14. Seismograms from the same 50 receivers and the same 2-D (left) and 3-D (right) simulations as shown in Figure 13, but here analogous horizontal particle velocity components (the west–east oriented ones) are displayed.
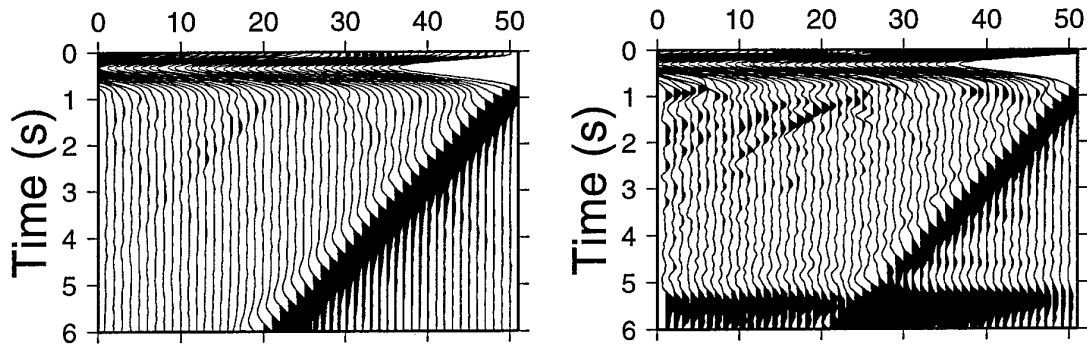

Figure 15. *Left:* Seismogram from 2-D simulation of a 60 km long topography data profile taken along the south–north oriented receiver line from the left part of Figure 4. The profile is 28.8 km deep and extends from 25.6 km south of the receiver furthest to the south to 5 km north of the receiver furthest to the north. The profile contains the displayed line of 50 south–north oriented receivers inter-spaced by 600 m. The vertical particle velocity component is displayed. *Right:* Seismogram from the 3-D simulation of the 60 × 60 × 28.8 km model displayed in the snapshots. The 50 receivers are located along the south–north oriented receiver line displayed on the left part of Figure 4 and inter-spaced by 600 m. Because of geometrical spreading, the amplitudes are multiplied by 3.5 to make the main arrivals the same order of magnitude as those for the 2–D case on the left. The vertical particle velocity component is displayed.
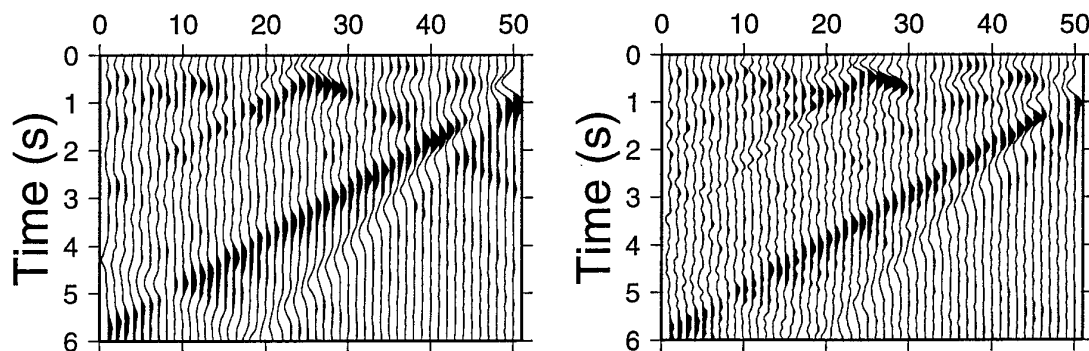
Figure 16. Seismograms from the same 50 receivers and the same 2–D (left) and 3–D (right) simulations as shown in Figure 15, but here analogous horizontal particle velocity components (the south–north oriented ones) are displayed.

Appendix 8

Geophys. J. Int.

RECOGNIZING EXPLOSION SITES WITHOUT SEISMOGRAM READINGS:

NEURAL NETWORK ANALYSIS OF ENVELOPE TRANSFORMED

MULTISTATION SP RECORDINGS 3 - 6 HZ.

Yu. V. Fedorenko[1,2], E. S. Husebye[1], B. Heincke[1,3] and B. O. Ruud[1]

1) Institute Solid Earth Physics, University of Bergen, Norway
2) Institute of North Ecology Problem, Fersman street 14, Apatity, Russia
3) Institute of Geophysics, Albrecht University, Kiel, Germany

SUMMARY

Seismic waveform similarities for closely spaced earthquakes and explosions in particular are well established observationally. In many industrialized countries of low seismicity more than 90 % of seismic event recordings stem from chemical explosions and thus contribute significantly to the daily analyst workload. In this study we explore the possibility of using envelope waveforms from a priori known explosion sites (learning) for recognizing subsequent explosions from the same site excluding any analyst interference. To ensure high signal correlation while retaining good SNRs we used envelope transformed waveforms including both the P and Lg arrivals. To ensure good spatial resolution we used multistation (network) recordings. The interpolation and approximation neural network (IANN) of Winston (1993) was used for learning the computer to recognize new explosion recordings from a specific site using detector output event files of waveforms only. The IANN output is a single number between 0 - 1 and on this scale an acceptance threshold of 0.4 proved appropriate. We obtained 100 % correct decisions between two sets of 'site explosions' and hundreds of 'non-site' explosions/earthquakes using data files from the Norwegian Seismograph Network.

KEY WORDS: neural network, site rcognition, explosion, envelopes, automatic analysis

INTRODUCTION

An experienced analyst is often capable to locate an earthquake simply by a brief visual inspection of a single station recording (Vesanen, 1944). With easy access to digital recording the ability to recognize specific explosion sites at least in a semi-automatic manner has been explored by several investigators like Israelsson (1990), Harris (1991), Riviere-Barbier and Grant (1993) and Jost, Schweitzer and Harjes (1996) among others. The basic idea is that many explosions are confined to a few sites which should be recognizable through correlation and cluster analysis of waveform records. Research focus has been mainly on separating closely spaced explosions, although accurate "ground truth" information is often lacking. Since the source correlation distance may exceed a few wavelengths of the dominant P-signal period it is not easy to resolve closely spaced explosion sites. To improve resolution, 'covariance records' in combination with clustering analysis and a manual touch was used by Israelsson (1990) and Riviere-Barbier and Grant (1993), while Harris (1991) expressed site resolution in a probabilistic manner in terms of bandwidth and time duration. Joswig (1990) on the other hand used sonograms for seismic signal detection based on a priori known signal patterns. However, the above schemes do not appear convenient for semi-automatic seismogram analysis of array and network recordings -- not easy to use nor robust enough. Nevertheless, the logic of using seismic waveforms of various kinds for identifying local explosion sites is attractive since it would ensure to pinpoint locations with a minimum of analyst effort. Such a scheme would be of particular interest in low-seismicity countries where up to 95 % of local event recordings are explosions. In this short note we describe a neural network scheme for recognizing specific explosion sites using envelope transformed (short period vertical component) network recordings of local events.

DATA ANALYSIS SCHEME

The problem considered here is a variant of classical seismic source discrimination --

earthquake or explosion (Husebye and Dainty, 1996). However, it is simpler, as we aim to

recognize explosion sites using multistation envelope waveform patterns tied to the basic

assumption that these are site specific. These waveforms are envelope transforms of bandpass

filtered (3 - 6 Hz) recordings, formed by first computing signal power in 2 sec long moving

timewindow (STA window) at 0.5 sec intervals. These STA time series are futher smoothed by

convolution with 3 'boxcar' functions of length 6, 8 and 10 sec. Finally, the square root of

each sample in the new time series are computed so the envelopes effectively consist of

smoothed RMS amplitudes.

Various kinds of neural network schemes have proved to be efficient tools in

discrimination analysis (Dowla, 1996). For the site recognition problem the so-called

interpolation and approximation neural nets (IANN; Winston, 1993) or radial basis function

networks (Dowla, 1996) appear to be ideally suited for our purpose. It has the virtue that

training (or learning) can be tied to solving a set of linear equations hence in this case it is not

necessary to involve any optimization method in order to obtain the weights. Below we

outline the construction of this particular variant of neural nets following the approach of

Winston.

The starting point is several inputs $\mathbf{x} = (x_1,\ x_2, ..., x_N)^{\mathrm{T}}$ and one output Y as

illustrated in Fig. 1. The input vector $\mathbf{x}$ consists of K sub-vectors, $\mathbf{x} = (\mathbf{x}_1,\ \mathbf{x}_2, ..., \mathbf{x}_K)^{\mathrm{T}}$

where K is the total number of stations used in analysis. Each sub-vector $\mathbf{x}_m$, $m = 1, 2, ..., K$

is the envelop record for station m. The number of samples in each sub-vector is different

because it is determined using the distance from each station to the site when calculating time

windows. Lg dominates our waveforms, thus the different station traces are weighted accordingly. Station weighting, whether tied to body or surface waves geometrical spreading was not critical for the final results. The output Y may be a single number (the score) and preferably $Y \in [0,1]$ for facilitating performance comparisons. The aim is to predict future Y-values for new (and unknown epicenters) given a proper data set (or learning set) of input-output combinations.

Let the output function $Y(\mathbf{x})$ have the following properties; (*i*) the value of Y is exactly equal to 1 whenever the input event coincides to the one of the events in the learning set. (*ii*) The value of Y should be close to 1 for all other events stemming from the site subject to recognition analysis and close to 0 for the remaining events. The output Y is denoted the 'interpolation' function by Winston (1993) and may be expanded into a weighted sum of other functions $f_i(\mathbf{x})$, $Y(\mathbf{x}) = \sum_{i=1}^{S} W_i f_i(\mathbf{x})$, where S is the number of events in learning set. It consists of multistation records from the specific site we want to recognize.

Using vector notation this might also be written as

$$Y(\mathbf{x}) = \mathbf{W}^T \mathbf{f} \qquad\qquad (1)$$

where $\mathbf{W} = \left(W_1, W_2, .., W_S \right)^{\mathrm{T}}$ is a vector of weights.

According to Winston, a convenient choice for $f_i(\mathbf{x})$ is a Gaussian function that may be written in the form $f_i(\mathbf{x}) = \exp\left(-\frac{1}{2\sigma^2} \|\mathbf{x} - \mathbf{c}_i\|^2 \right)$, where the norm $\|\mathbf{x} - \mathbf{c}_i\|^2 = \sum_{j=1}^{N} \left(x_j - c_{ij} \right)^2$ and N is the number of observation points (total number of samples) in input. The shape of $f_i(\mathbf{x}) = f_i\left(\|\mathbf{x} - \mathbf{c}_i\|^2, \sigma \right)$ is controlled by given values of σ and $\mathbf{c}_i$. The latter is a reference vector obtained from the i-th event of the learning set. Because each $f_i(\mathbf{x})$-value depends on only one $\mathbf{c}_i$-value the $f_i(\mathbf{x})$-function together with the weight W_i are tailoring the influence of

the i-th learning sample on future predictions of Y. To summarize, the function Y is computed by a 2-layer net by which the single node in the second layer (see Fig. 1) computes a weighted sum of the outputs of the first layer nodes. In turn, each of the first layer nodes "computes" a Gaussian function centered on the "sample" input.

For a given σ - value of f_i a set of linear equations can be written for calculating the vector $\mathbf{W}$ in eq. (1). In our IANN approach the output Y is 1 for samples drawn from the learning set, so, substituting the input $\mathbf{x}$ by the $\mathbf{c}_i$ we rewrite equation (1)

$$\sum_{i=1}^{S} f\left(\left\|\mathbf{c}_i - \mathbf{c}_{ij}\right\|^2, \sigma\right) W_i = 1, \text{ for } j = 1, .., S \qquad (2)$$

or, in matrix notation $\mathbf{AW} = \mathbf{1}$ where $\mathbf{1} = \left(1, 1, ..., 1\right)^{\mathrm{T}}$, $A_{ij} = f\left(\left\|\mathbf{c}_i - \mathbf{c}_j\right\|^2, \sigma\right)$ and $\mathbf{W} = \left(W_1, W_2, ..., W_S\right)^{\mathrm{T}}$. The linear system of eq. in (2) comprises S unknowns but also S-equations. The $\mathbf{A}$-matrix is positive definite and symmetric. However it may be ill posed due to the arbitrary choice of events for the learning set (some very small eigenvalues may appear if chosen envelops are quite similar) so the SVD approach (singular value decomposition) was preferred for solving eq. (2). The record lengths vary between individual stations. Preferably both the P and Lg envelopes should be included for all stations in a learning set, which in turn should comprise the largest number of network recording stations available because this "master" learning set then can easily be adjusted to any sub configuration of the network. This property is important since quite often data from one or more stations in a network are missing and corresponding new weights are fast to compute from eq (2). Using network envelopes has three advantages, (i) high signal similarity, so few events are needed in learning set; (ii) robustness, since envelope records are used; and (iii) quite good spatial resolution; since we use recordings including both P- and S (Lg)-waves from widely spaced network stations. Note, using high-frequency (8 - 16 Hz) explosion records from a single array, Israelsson (1990) and

Harris (1990) obtained 2 - 4 km spatial resolution while ours is around 6-8 km (Fig. 5). However, as demonstrated below, envelope processing is far more robust and hence convenient for automated record analysis.

DATA ANALYSIS AND RESULTS

The data used are local event recordings from the Norwegian Seismograph Network (NSN) (Fig. 2) for the period September 1992 to May 1997. The network is operated in a trigger mode implying that original waveforms from individual detecting stations are merged into easily accessible event files. An essential element in our site recognition analysis is to establish the reliable learning set. In this regard, only 2 explosion sites proved convenient, namely the open pit mine Titania (TITA) and an underwater harbor construction site in Geiranger Fjord (GEIR). For both of these sites written notifications of each shot were received. The other events subjected to analysis were different for TITA and GEIR reflecting varying station detectabilities for these 2 sites (Fig. 2). Since P- and S-group velocities are quite different the envelope shapes change rapidly with epicenter distance thus ensuring adequate spatial resolution. Origin time is not a problem since for the a priori known sites we can accurately calculate/predict the relative move-out times between the station used. Alternatively, one may use one event in the learning set to set the time windows manually for each station without any knowledge of the velocity model or station distance. Through 'sliding window operation' the IANN recognition scheme amounts to a two-pronged test; (i) that signal record move-out times correspond to the specific sites and (ii) their envelope waveform shapes conform to those of the learning set (Fig. 3).

The envelope event files were screened for appropriate candidates conditioned on; (*i*) relatively large number of recording stations (3-7) and (*ii*) a minimum of 3 stations in common with the learning set. On average, the Titania and Geiranger explosions are recorded at 3 - 6

stations only so there is an obvious need to adjust the learning set to the specific event recordings at hand as discussed above. Even in the extreme case of only 2 recording stations, site recognition was sometimes feasible. In Fig. 3 the Titania and Geiranger learning set envelopes are shown. The site recognition performance depends on the variance (σ-parameter) in the presumed Gaussian distribution (1, 2). Testing gave that the best population separation was obtained for a σ value at 0.04 which was used in subsequent analysis.

The outcome of the site recognition analysis are displayed in Fig. 4 for Geiranger and for both sites in Fig. 5. The performance for Geiranger was better than that for Titania which partly is attributed to a better network configuration (Fig. 2). Occasionally, "true" Titania events had scores below the threshold of 0.4. To our surprise this was due to small errors of a few seconds in the station timing system (ODD1, ASK, EGD). The site recognition scheme also has good spatial resolution. As apparent from (Fig. 5), any event more than 6-8 km away from 'true' site location would be rejected. If closer and with similar envelope shape, it could possibly be accepted as a 'site explosion'. Best results were obtained for Geiranger where with one exception all scores for confirmed explosions exceeded 0.7 units. The non-Geiranger event scores were mostly zero and never exceeded 0.2 units. For Titania the results are similar but somewhat lower in absolute terms, i.e., score between 0.4 and 0.7 are relativly frequent. These lower scores are in part attributed to the aforementioned timing errors. However, some non-Titania events in the range 100 - 150 km from Titania have scores between 0.2 - 0.4 and the corresponding epicenter locations are in some cases close to the stations KMY or BLS (Fig. 2a). The explanation here is as follows: only 3 stations are used namely ASK, EGD and KMY or BLS with an appearant lined-up versus the Titania site. In two cases, low site recognition scores were due to interference from other events causing Lg envelope shape modifications.

DISCUSSION.

Our novel approach to explosion site recognition has, unsurprisingly, performed well on this dataset. The discrimination power of our IANN approach is surprising; rather small timing errors either stemming from clock defects or other epicenters a few kilometers away from site suffice for rejecting the event in question. This also implies that our approach as presently formulated hardly would be applicable for earthquake record analysis because of less spatial clustering of foci even in cases of swarm activities.

In areas like Fennoscandia and large parts of Europe, site recognition scheme has the potential of significantly reducing tedious analyst effort in bulletin preparations since 90 - 95 % of all local events stem from mining and construction explosion activities. The former seismic source type is most convenient to handle since operational span often amounts to many years while construction works finish in months or at most a few years. The latter can also be handled effectively by our selection approach since the learning set can be established with 5 - 10 events. However, a potential drawback is that analyst is often unaware of temporary explosion sites, leading to ground truth problems in event selection for learning sets. Also bulletin epicenter solutions are quite error prone (Fig. 2a and 2b) so this parameter is not helpful in this regard (Husebye, Ruud and Dainty, 1998).

Our site recognition scheme does not incorporate specific earthquake/explosion source type criteria but essentially discriminates on spatial locations for presumed identical envelope recordings. However, for this type of problems we may for envelope generation use several bandpass filters reflecting those Pn and Lg signal frequencies for which the best earthquake/explosion source separation has been obtained (Dowla, 1996). In special cases, we may consider non-envelope transformed record analysis like those of Israelsson, (1990), Joswig (1990) and Harris, (1990). Regrettably, to obtain an adequate data base for recognizing

source type appears to be problematic. The main potential of our flexible explosion site recognition approach is to reduce significantly the analyst work in many industrial countries.

ACKNOWLEDGEMENT

REFERENCES.

F. U. Dowla (1996). Neural networks in seismic discrimination. In E. S. Husebye and A. M. Dainty (eds), Monitoring a Comprehensive Test Ban Treaty, NATO ASI Series, Kluwer Academic Publ., Dordrecht, The Netherland, 777 - 789.

A. Frankel (1982). Precursors to a magnitude 4.8 earthquake in the Virgin Islands, spatial clustering of small earthquakes, anomalous focal mechanisms, and earthquake doublets, Bull. Seism. Soc. Am., 72, 1277 - 1294.

D.B. Harris (1991). A waveform correlation method for identifying quarry explosions, Bull. Seism. Soc. Am., 81, 2395 - 2418.

E.S. Husebye and A.M. Dainty (eds., 1996). Monitoring a Comprehensive Test Ban Treaty, NATO ASI Series, Kluwer Academic Publ., Dordrecht, The Netherlands, pp. 836.

E.S. Husebye, B.O. Ruud and A.M. Dainty (1998). Fast, robust and reliable epicenter determinations: Envelope processing of local network data, Bull. Seism. Soc. Am., Feb. 1998.

H. Israelsson (1990). Correlation of waveforms from closely spaced regional events, Bull. Seism. Soc. Am., 80, 2177 - 2193.

M.L. Jost, J. Schweitzer and H.-P. Harjes (1996). Monitoring nuclear test sites with GERESS, Bull. Seism. Soc. Am., 86, 172 - 190.

M. Joswig (1990). Pattern recognition for earthquake detection, Bull. Seism. Soc. Am., 80, 170 - 186.

J. Pechman and H. Kanamori (1982). Waveforms and spectra of preshocks and aftershocks of the 1979 Imperial Valley, California earthquake: evidence for fault heterogeneity ?, J. Geophys. Res., 87, 10579 - 10597.

F. Riviere-Barbier and L. T. Grant (1993). Identification and location of closely spaced mining events, Bull. Seism. Soc. Am., 83, 1527 - 1546.

P.M. Shearer (1997). Improving local earthquake locations using the L1 norm and waveform cross correlation: Application to the Whittier Narrows, California, aftershock sequence, J. Geophys. Res., 102, 8269 - 8284.

P.H. Winston (1993). Artificial Intelligence, 3rd ed. Addison-Wesley Publ. Co., 491 - 504.

E. Vesanen (1944). Uber die Typenanalytische Ausvertung der Seismogramme, Ph.D. thesis, Ann. Acad. Sci. Fennicae, Helsinki, Finland, pp 244.

FIGURE CAPTIONS

Figure 1. The Interpolation and Approximation Neural Net (IANN, Winston, 1993).

Figure 2a. The stations of the Norwegian Seismograph Network (NSN) used in our site recognition analysis for the open pit mine explosions at Titania (TITA). Rings are event epicenter locations taken from the NSN-bulletins while ring shading indicates recognition score: white = 0.0-0.1; gray = 0.11 - 0.39 and black > 0.40. The dispersion of high score events around the Titania mining site simply reflects errors in the local bulletin for these explosions. Such errors are significantly smaller for the Geiranger explosions. Score results also presented in Figs. 4 and 5.

Figure 2b. The stations of the Norwegian Seismograph Network (NSN) used in our site recognition analysis for the underwater construction explosions in Geiranger. In comparison to Titania (2a) bulletin location errors are small. Figure caption otherwise as for Fig. 2a.

Figure 3a. Stippled envelope traces for individual station recordings for known (confirmed) Titania explosions which were used as learning set in the site recognition analysis. These recordings, typically comprising 3 - 10 events, are flexible in the sense that number of stations used can be reduced to 3 or even 2 if some of the station recordings are lacking or defect. Notice the consistent dominance of Lg-phase and the often weak, first arriving, Pg-phase. The latter is occasionally lost in the ambient noise. For convenience, traces are time shifted relative to expected P-onset time computed from epicenter distances. The traces marked by a solid line are a 'new' event subject to IANN recognition test. The score is given on the top of the figure together with the σ-value of 0.04 and Origin Time (year, day, hr, min, sec).
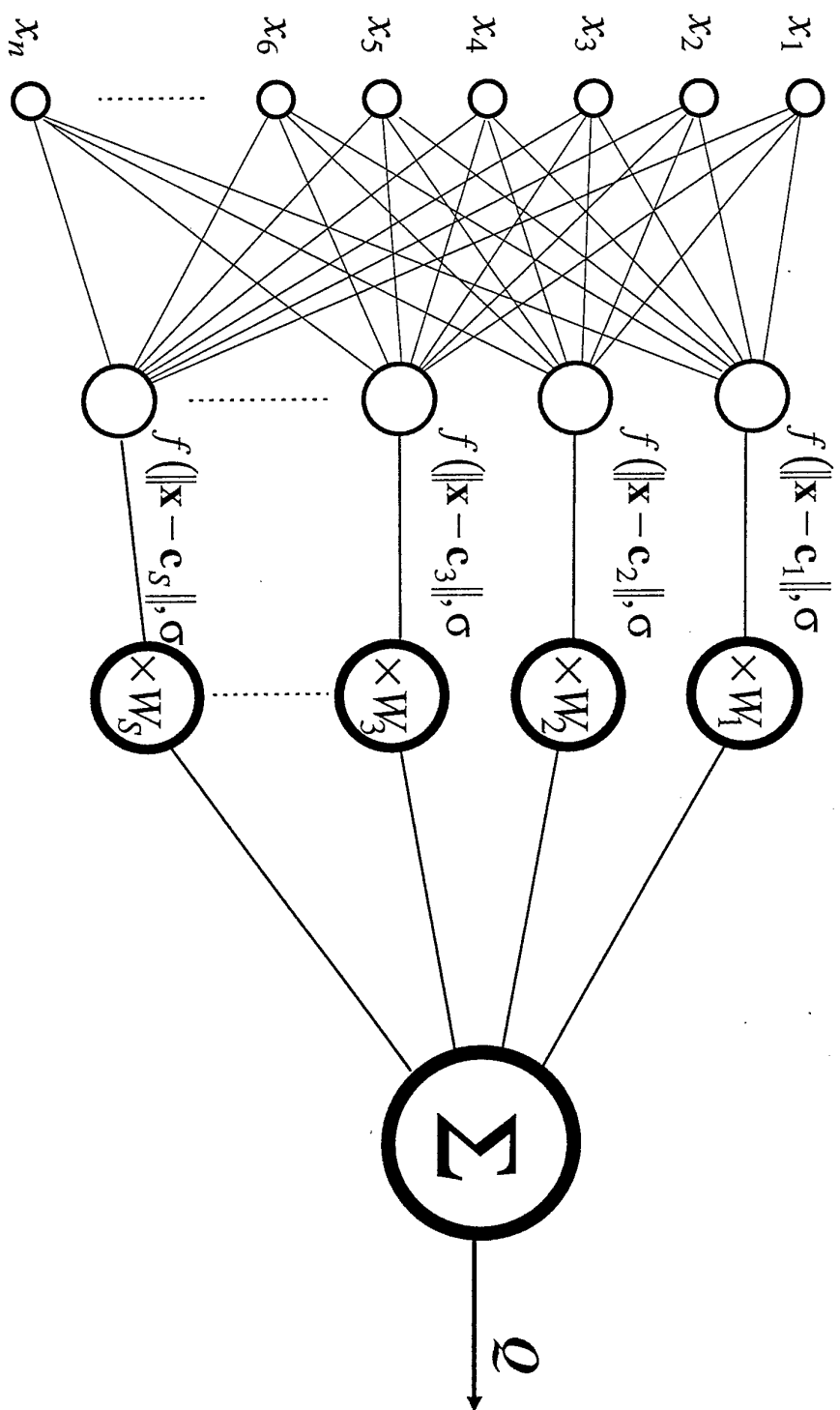
Figure 3b. Stippled envelope traces for individual station recordings for known (confirmed) Geiranger explosions which were used as learning sets in the site recognition analysis. Caption otherwise as for Fig. 3a.
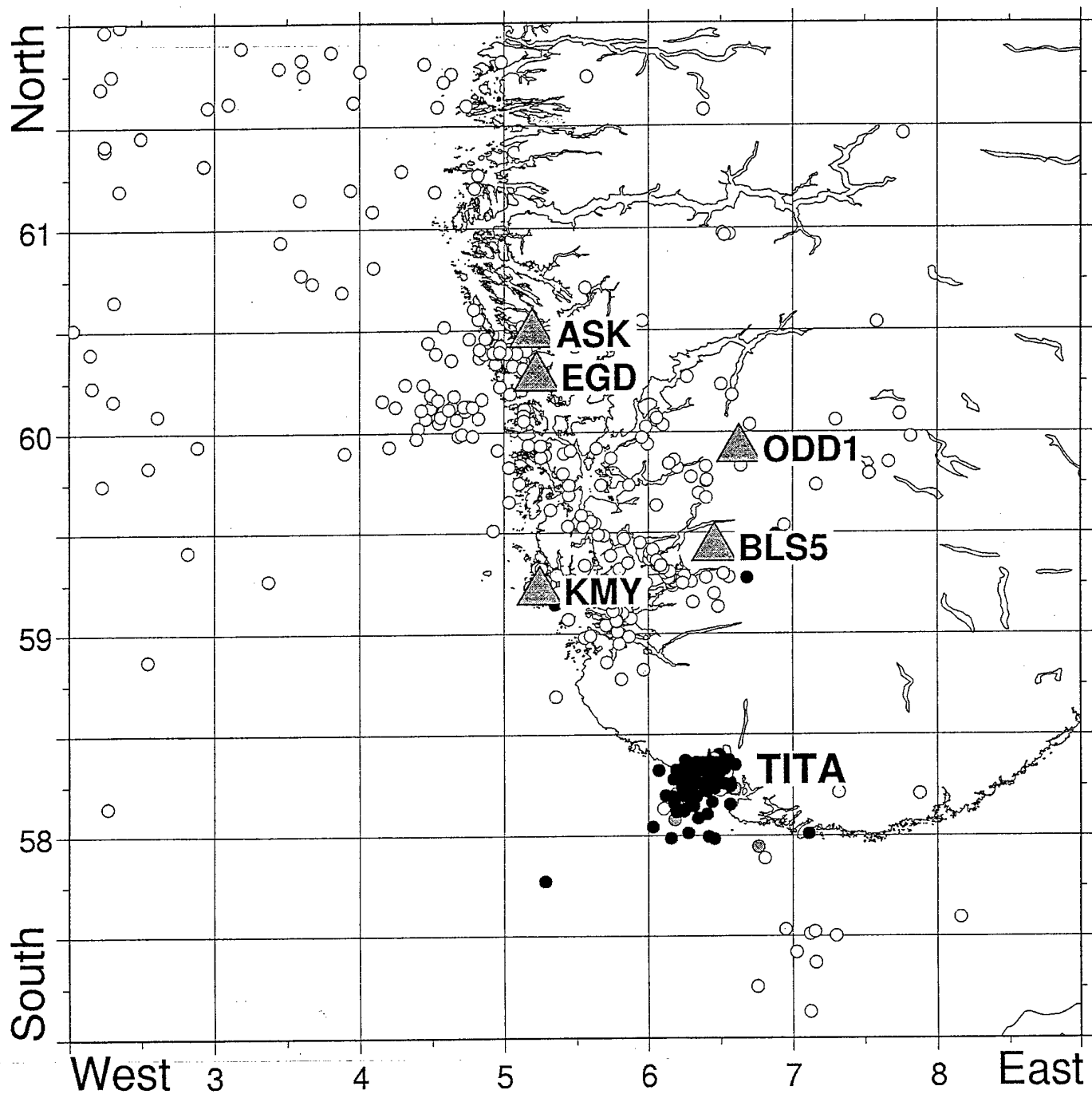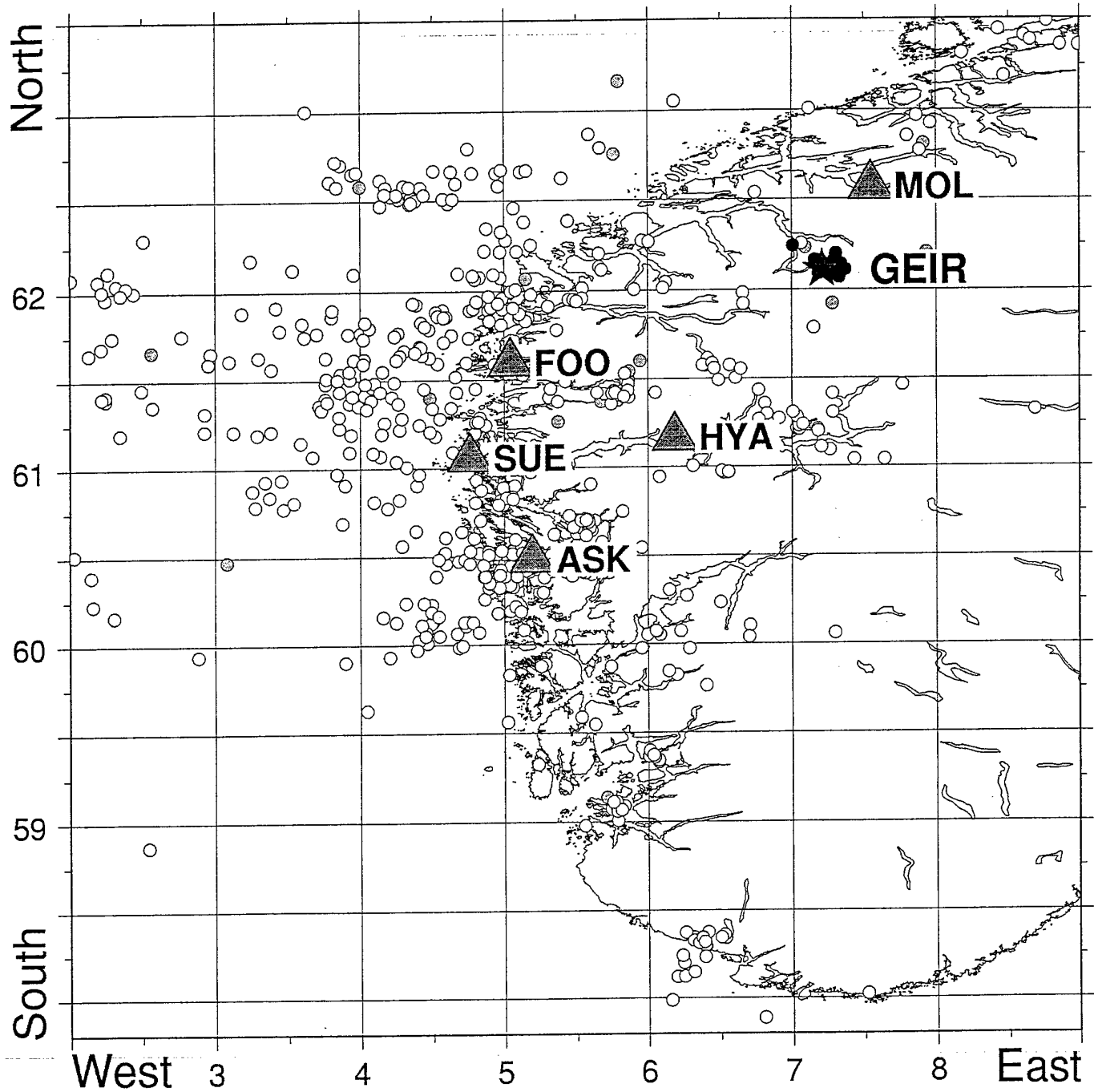
Figure 4. Geiranger site recognition scores (vertical axis) as a function of distance between the site and the epicenters depicted in Fig. 2b. Regrettably, we lack information about which events are explosions and which are earthquakes. Notice that the scores, with one exception, are uniformly high, i.e., larger than 0.7 units. The non-site (more than 600) events have uniform low scores below 0.2 units so the discrimination between site and non-site events is excellent.

Figure 5a. Simulated Titania score performances as a function of fictitious epicenter position relative to the 'true' site location. The recognition score acceptance of 0.4 units is equivalent to an area of radius 8 km.
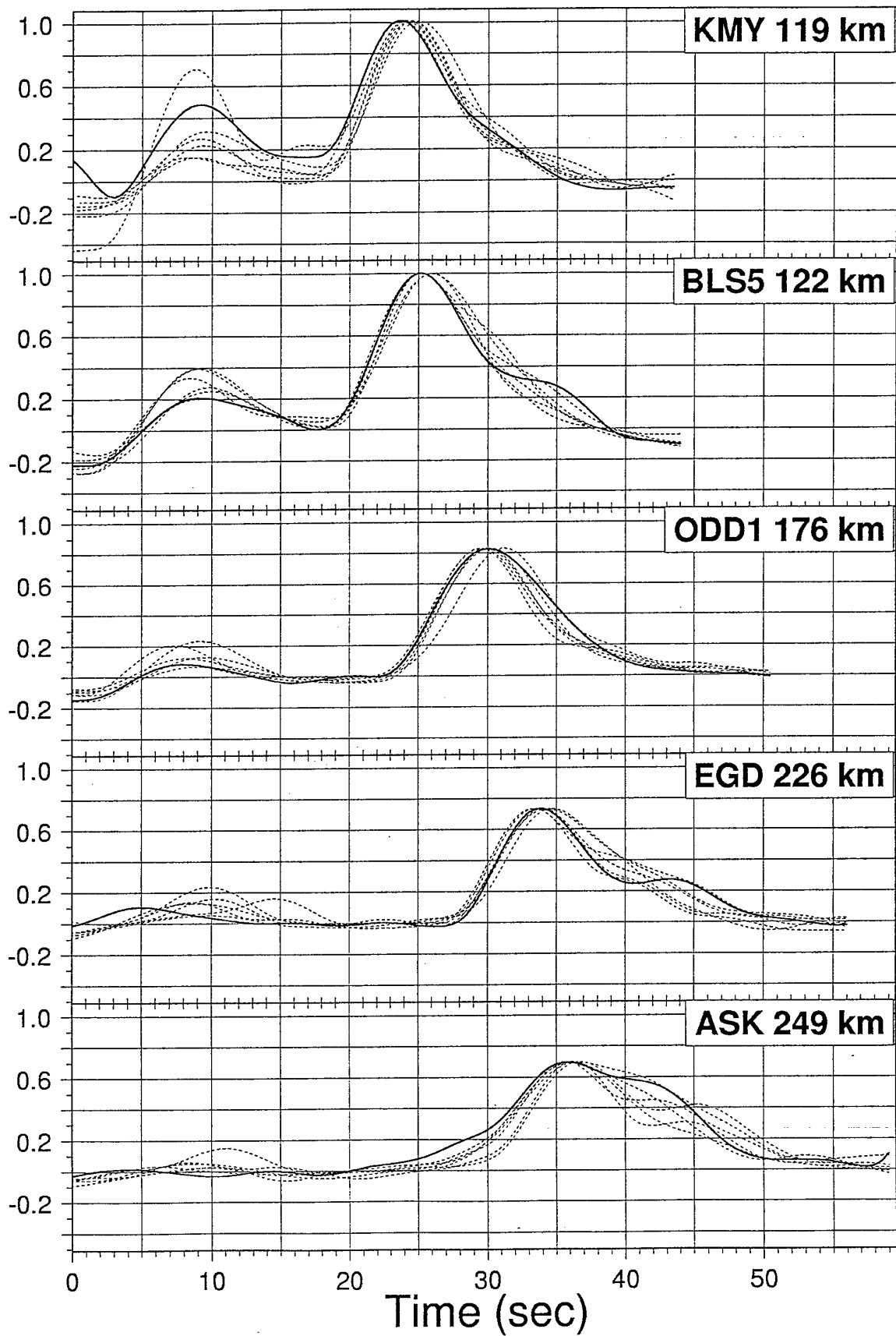
Figure 5b. Simulated Geiranger score performances as a function of fictitious epicenter position relative to the 'true' site location. Due to a non-uniform network configuration the recognition score acceptance area is elliptic with the largest half-axis of 10 km.
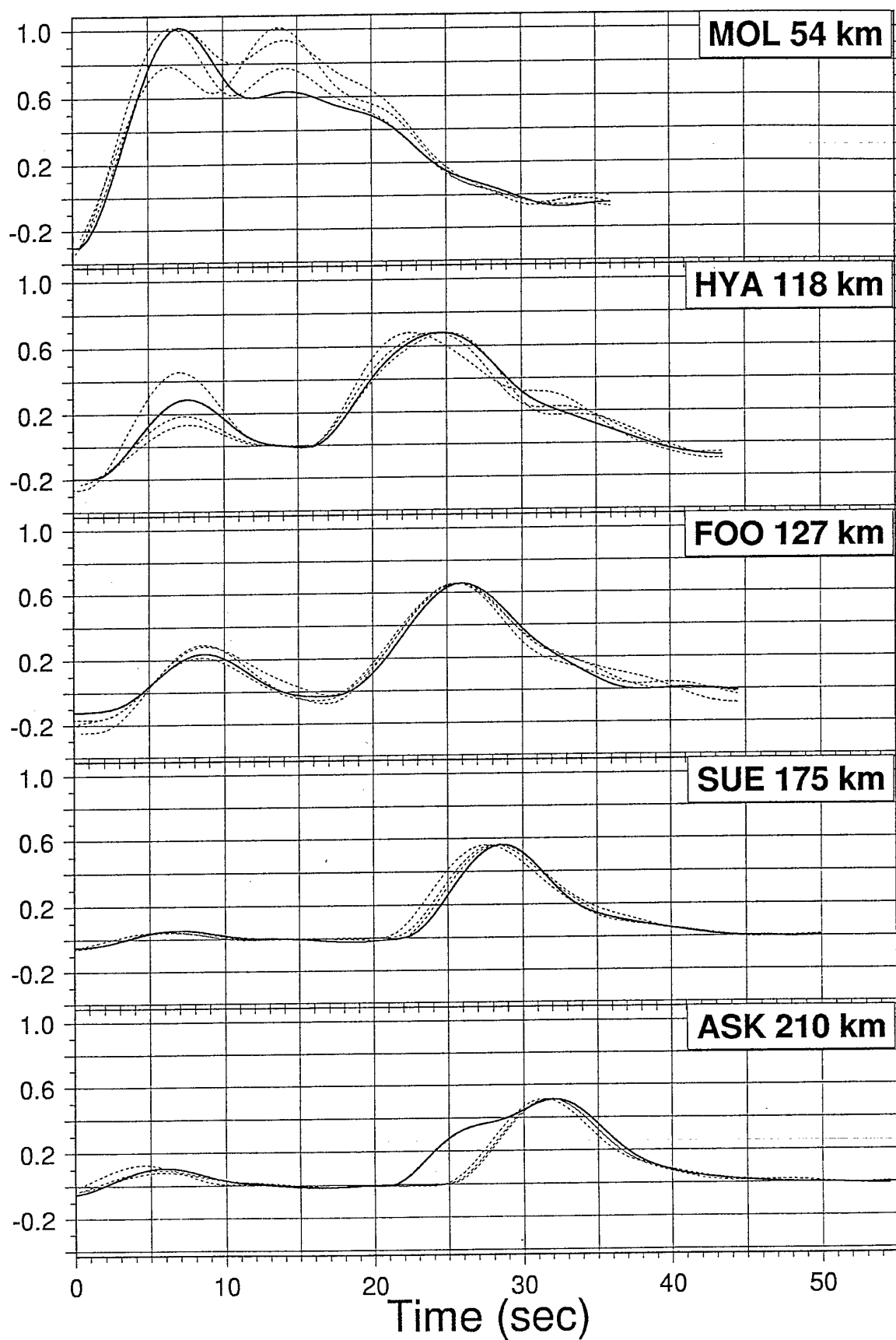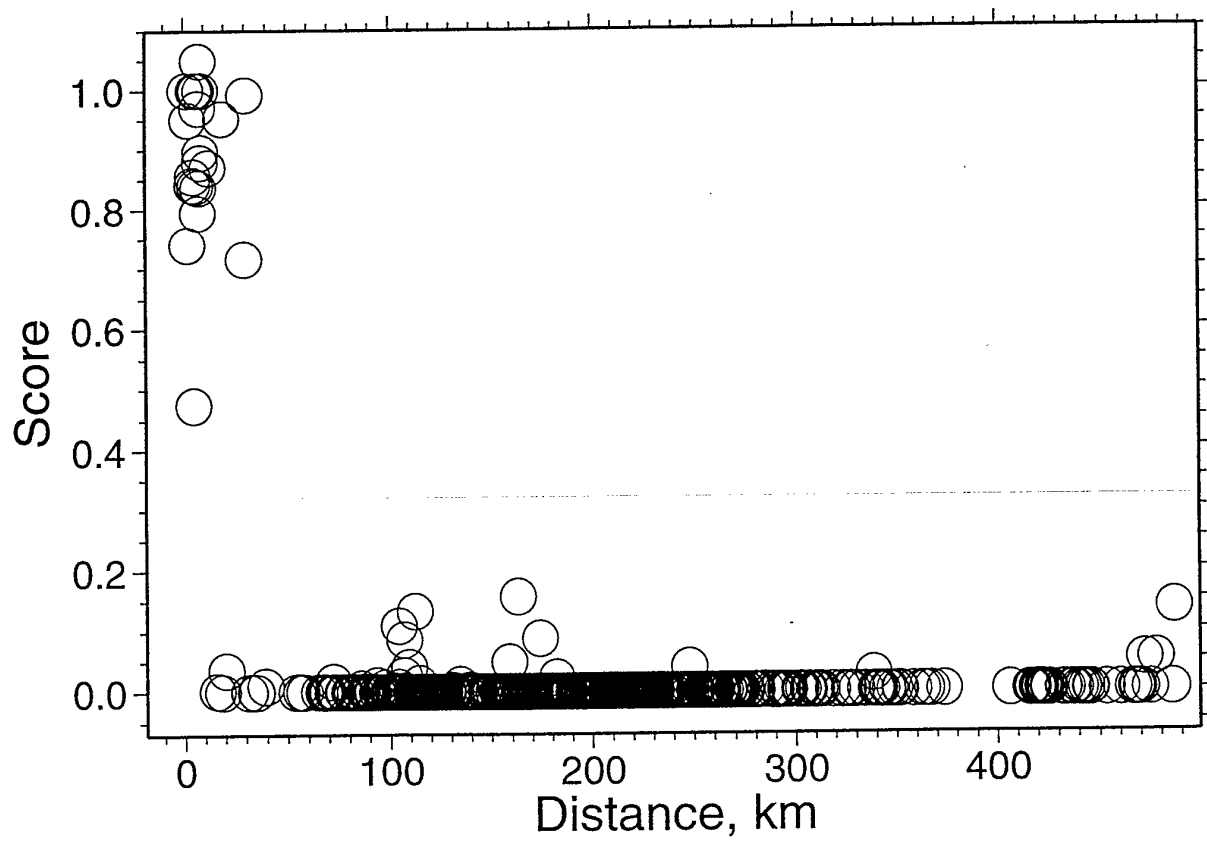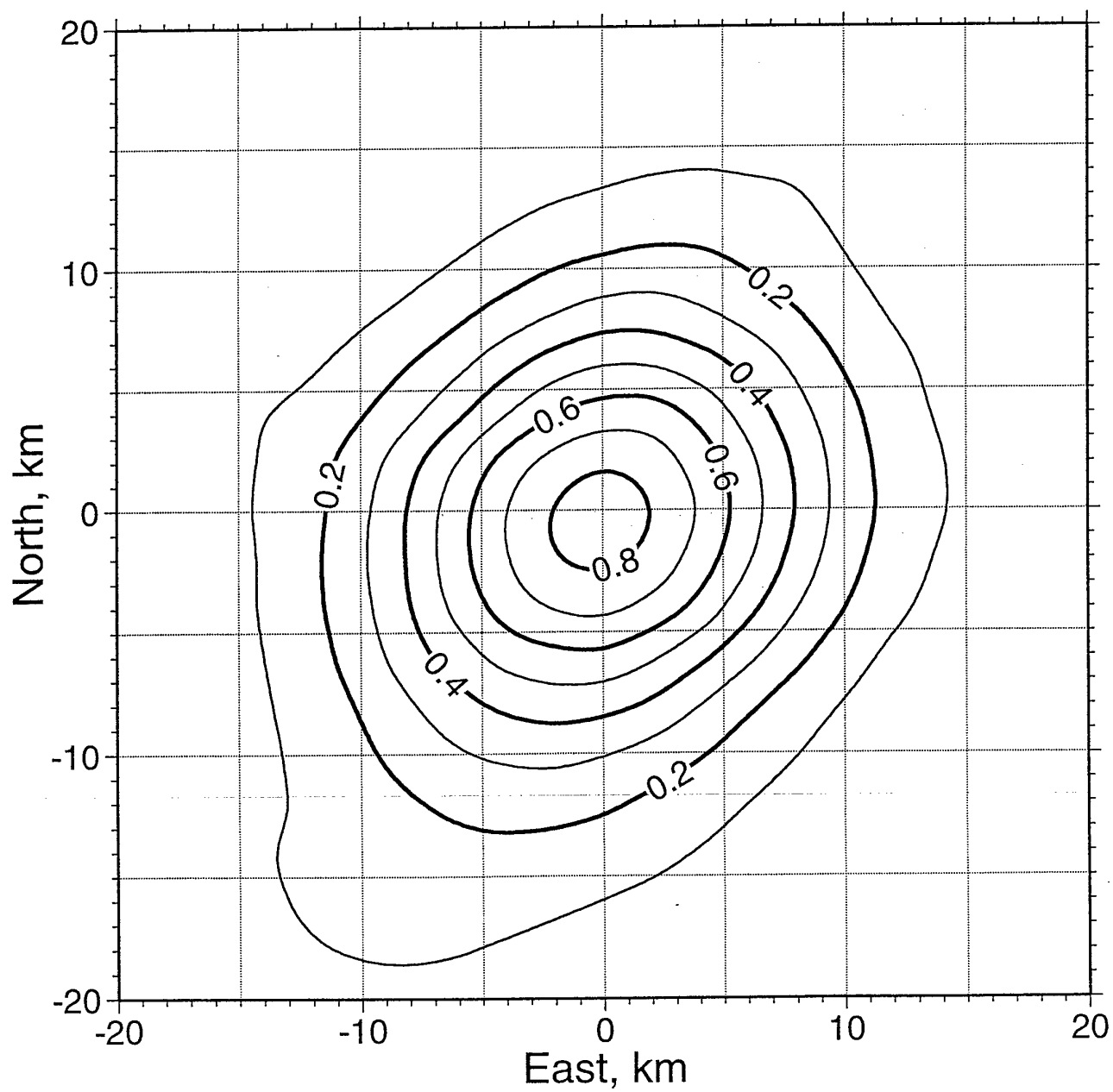
x_1

x_2

x_3

x_4

x_5

x_6

x_n

$f(\|\mathbf{x} - \mathbf{c}_1\|, \sigma)$

$f(\|\mathbf{x} - \mathbf{c}_2\|, \sigma)$

$f(\|\mathbf{x} - \mathbf{c}_3\|, \sigma)$

$f(\|\mathbf{x} - \mathbf{c}_s\|, \sigma)$

$\times W_1$

$\times W_2$

$\times W_3$

$\times W_s$

Σ
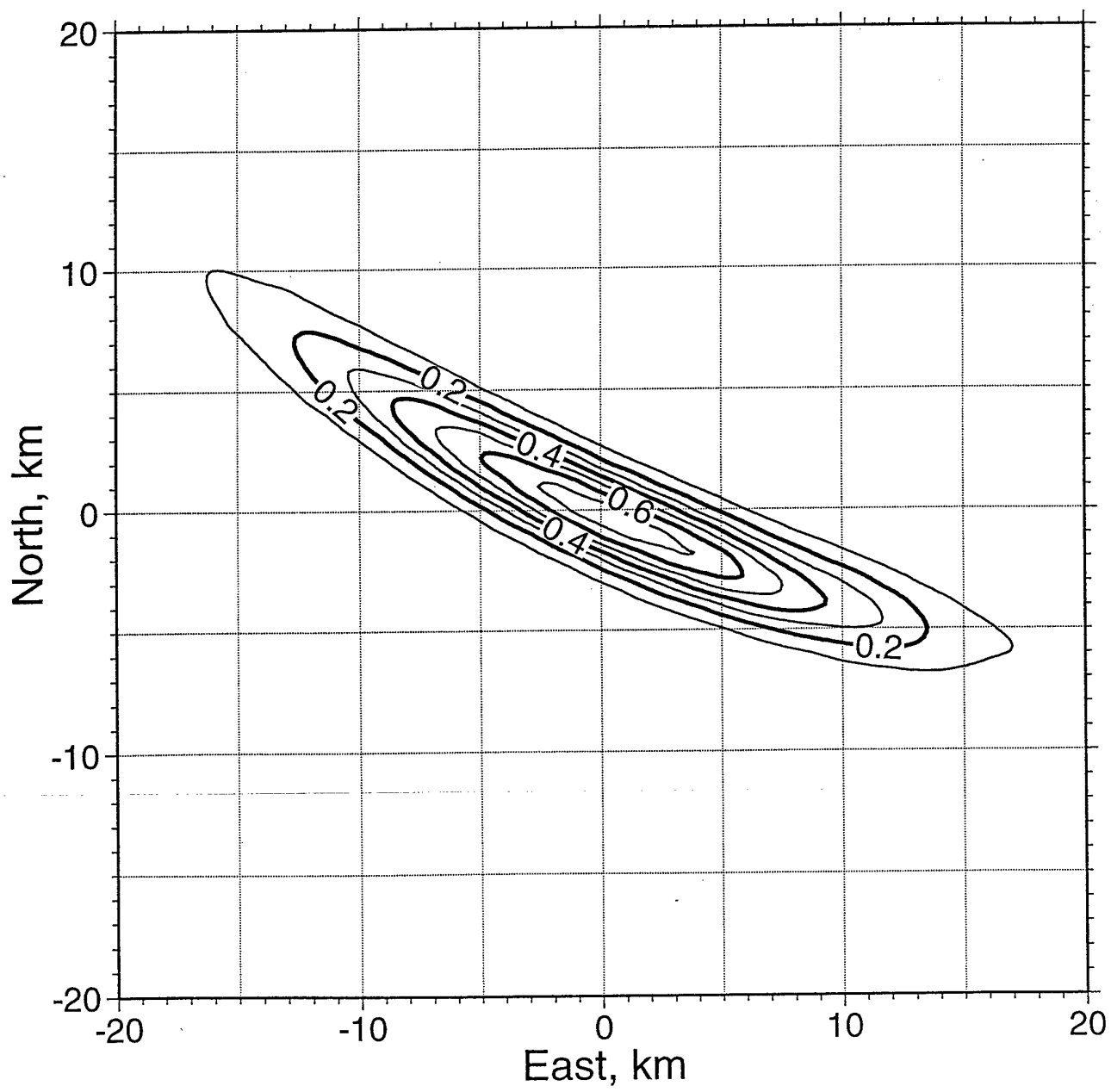
ϱ

TITA   Score = 0.84   1993-351:14:17:19.3

GEIR   Score = 1.0   1996-299:10:55:08.3

Appendix 9

4.9 Signal site recognition using single station 3-component records

As mentioned, seismic waveform similarities for closely spaced explosions are well established observationally. Also, encouraged by our previous site recognition results we considered additional flexibility in our approach to this problem essentially how to incorporate additional seismic record information in the neural network analysis. Another motivation here was to safeguard against technical defects like timing errors which otherwise would ruin multistation analysis. The alternative strategy choosen for extracting relative comprehensive signal attributes was that of using single station 3-component (3C) records. By introducing complex demodulated record operations (including both the P- and S-wave arrivals and part of the coda) the 3C covariance matrix would contain 3x3 elements of different time information. From other source classification studies we know that both explosion and earthquake spesific information are contained in several frequency bands so we formed covariance matrixes for a suit of 12 different frequency bands. In other words, a single 3C station event record produced 9x12 = 108 pieces of time information. Having access to 'ground truth' information from 2 underwater construction sites (Mongstad and Geiranger) we had 4 - 6 events (enough) for site recognition learning sets. Obtained results were excellent; all events from the construction sites (not in learning sets) were classified as such while all other events (more than 200) were classified as non-site events whether source was an explosion or an earthquake. Presuming log-normal distribution of the neural network output score factor we estimated that the probabilities of false alarm or missed 'detection' were less than 1:1,000,000. Also, spatial resolution was good (less than 10 km) even perpendicularly to the station-site azimuth direction. During this 3C site recognition exercise we found in the epicenter map used, 2 cluster of events with which origin times were mainly between 10. - 14. hours that is prime working hours. Selecting events directly from bulletin for learning sets but without ground truth information at hand did produce results somewhat less convincing in comparision to those obtained for Mongstad and Geiranger. This kind of problems, lack of ground truth information for appearant event clusters, would in future be addressed through an initial multivariate analysis scheme in order to sort out 'most similar' event recordings and hence the likely event candidates for learning sets.

This is just Abstract; first DRAFT not in

a state to be included in Final Rep.

just now - would send soon!

Egrli J. Husebye?